CHAPTER 8

Structural Studies of Polymer Systems Using Small-Angle Neutron Scattering

Kell Mortensen*

Condensed Matter Physics and Chemistry Department, Risφ National Laboratory, DK-4000 Roskilde, Denmark

Contents

* Tel.: +45 4677 4710, Fax: +45 4677 4790, e-mail: kell.mortensen@risoe.dk

Advanced Functional Molecules and Polymers, edited by H.S. Nalwa
Volume 2, Processing and Spectroscopy

ISBN 90-5699-309-7

1 Introduction

Multi-component macromolecular and colloidal systems attract lots of applied as well as basic interests. Industrial applications tend to use still more complex polymeric systems, where specific structural properties are aimed, and where miscibility parameters play essential role. There are therefore broad interests on the exploration of basic thermodynamic equilibrium properties as well as gain of better understanding on the non-equilibrium behavior. Generally, the thermodynamic properties of polymer systems are described within the Flory-Huggins model, which is based on the assumption of negligible small thermal composition fluctuations as in the mean field approach. Scattering experiments have proven to be one of the major techniques used to provide details on the phase behavior and related thermodynamics. In particular neutron scattering has provided important information giving detailed structural insight using the possibility for labeling and contrast variation through exchange of specific hydrogen's with the deuterium isotopes.

Some textbook have been published in recent years with the aim to give the theoretical as well as the practical basis for the application of scattering techniques in polymer physics. A most important contribution in this context were made by Higgins and Benoit who in great detail present the basis for the use of neutron scattering for polymer studies [1]. Other textbook on neutron and x-ray scattering relevant for colloidal and polymer research include books of Strobl [2], Kotlarchyk and Chen [3], Lindner and Temb [4], Brown and Mortensen [5], and the classical books of Guinier and Fournet [6], and Glatter and Kratky [7].

In the following, the basic experimental procedure for studies of structural properties of polymers and polymeric colloids will be described. The text will be supported by representative examples of the various topics discussed. The examples are to a large extent from own studies, but will hopefully be representative for the more general cases.

The presentation will mainly concern neutron scattering, but several of the more general parts are applicable for x-ray scattering as well. We will first very briefly describe the sources needed for neutron scattering,

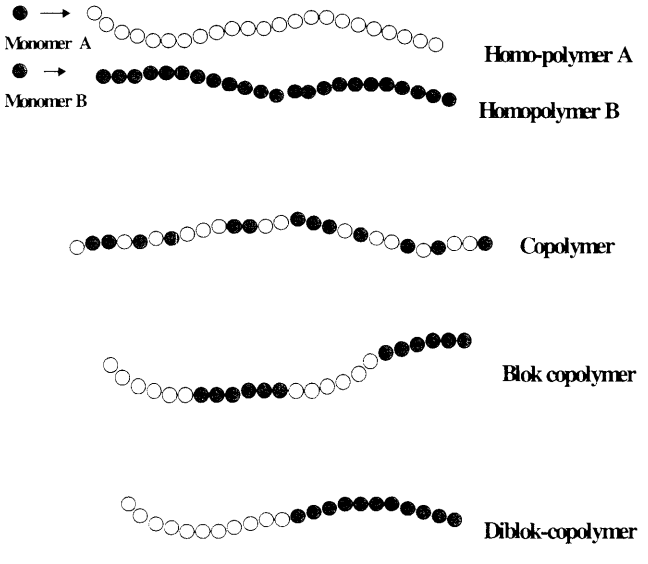

Figure 1 Illustration of various polymer types discussed in the text. Homopolymers, copolymer, random block copolymer and diblock copolymer.

and give some details on the experimental procedure. Successively, we will describe various topics in polymer physics using scattering technique, and give details on the analysis of the scattering function relevant for the various examples. We will start with polymer chain conformation and polymer gels, including some generalized comments on fractal structures.

Next, we will discuss in some detail the information that scattering experiments can provide on phase behavior of polymer blends, and discuss the composition fluctuations in terms of critical phenomena. In direct context to the mixtures of homopolymers, we will present how block copolymer phase behavior can be studied, and investigations of the variety of mesoscopically ordered crystal structures than many such systems evolve into. In the last parts we will describe the scattering function of more complex polymer systems, like blends of block copolymers and homopolymers or block copolymers and liquids. This latter part includes structural studies of micellar aggregates.

2 Basic Scattering Theory

Small angle scattering by x-rays and neutrons are to a large extent complementary techniques that are widely used to study structural properties of polymer and colloidal systems.

X-ray scattering have in general an instrumental resolution that is far beyond the possibility using neutrons. In ordered systems, x-ray scattering shows in addition often Bragg reflections to higher order than those observed in neutron scattering. The resolve of many Bragg reflections is in many cases necessary to discriminate between possibly ordered structures like those of block copolymer mesophases. Neutron scattering have, on the other hand, the advance relative to x-rays that polymer systems composed of even very similar molecular species, like for example different polyolefins, can be investigated by deuterium labeling specific sites. Labeling for the neutron experiment requires some times synthesis of deuterium monomers all from the beginning, but in other cases the labeling can be provided by exposing the sample to a deuterium-gas during a hydrogenation process of precursor polymers. Neutron scattering has another advance relative to x-ray that it in general is relative easy to obtain reliable scattering functions in absolute values, thereby providing detailed information on thermodynamics and on the interaction parameter.

2.1 Interaction Between Matter and x-Ray/Neutron Radiation

The interaction between matter and radiation is for x-ray scattering dominated by the response of the electrons, which is accelerated in the electric field of the beam. To a good approximation each electron scatters the beam as a dipole proportional to the term $b_e = e^2/m_e c^2$, where e is the electronic charge, m_e is the electron mass and c is the velocity of light. b_e, which has the dimension of length, $b_e = 0.282 \cdot 10^{-4}$ Å, is termed the *'scattering length'*. In the interaction with an atom, one must integrate over all electrons, (see e.g., reference [6]).

$$b_z = \int b_e \rho(\bar{r}) d^3 r \tag{1}$$

where $\rho(\bar{r})$ is the charge distribution in the atom. The integral, which depends on the scattering angle θ, defines the *atomic form factor*. For small-angle scattering ($\theta \approx 0$), the $\int \rho(\bar{r}) d^3 r$-term approaches the number of electrons, i.e., the atomic number Z, thereby giving the atomic scattering length $b_z = b_e Z$.

The interaction between neutrons and (non-magnetic) matter is dominated by the interaction with the nuclei. The scattering from different isotopes of the same atom may therefore be quite different. This is in particular the case for the two hydrogen isotopes, ^{1}H (abbreviated H) and ^{2}H (abbreviated D for deuterium), which provides the basis for labeling polymers. Since the neutron is a spin-1/2 particle, there are two different couplings between the neutrons in the beam and an ensemble of similar nuclei, unless the nucleus spin approaches zero (as in for example ^{16}O and ^{12}C). The average of these two interactions gives coherent scattering, whereas the deviation from average is incoherent and gives uniform background. Only the coherent scattering term gives information on the static structure. Hydrogen has a very high incoherent scattering power, and gives therefore relative high background. In the design of a sample for neutron scattering experiments, one should therefore aim to have the hydrogen's of the major polymer component exchanged with deuterium, rather than vice versa.

Table 1 Scattering length and incoherent scattering cross section of elements relevant for polymers.

Nuclei	*Coherent scattering length* b_i	*Incoherent cross section* δ_{ic}
H	-0.3739×10^{-12} cm	80.26×10^{-24} cm^2
^{1}H	-0.3741×10^{-12} cm	80.27×10^{-24} cm^2
^{2}H = D	0.6671×10^{-12} cm	2.05×10^{-24} cm^2
C	0.6646×10^{-12} cm	0.001×10^{-24} cm^2
^{12}C	0.6651×10^{-12} cm	0×10^{-24} cm^2
N	0.936×10^{-12} cm	0.50×10^{-24} cm^2
^{14}N	0.937×10^{-12} cm	0.50×10^{-24} cm^2
O	0.5803×10^{-12} cm	0.0×10^{-24} cm^2
^{16}O	0.5803×10^{-12} cm	0.0×10^{-24} cm^2
Si	0.4149×10^{-12} cm	0.004×10^{-24} cm^2
^{28}Si	0.4107×10^{-12} cm	0×10^{-24} cm^2
Cl	0.958×10^{-12} cm	5.3×10^{-24} cm^2
^{35}Cl	1.165×10^{-12} cm	4.7×10^{-24} cm^2
Ca	0.479×10^{-12} cm	0.05×10^{-24} cm^2
^{40}Ca	0.480×10^{-12} cm	0×10^{-24} cm^2

2.2 Scattering Amplitude and Intensity

The amplitude of x-ray or neutron radiation scattered into an angle 2θ from a collection of objects, located by vectors $\bar{r}_i$ and characterized by the scattering length b_i is obtained as the sum of all scattering sites of the sample, taken the phases into account:

$$f(q) = \sum b_i \cdot \exp\left[i(\bar{q} \cdot \bar{r}_i)\right] \tag{2}$$

where $b_i = b(\bar{r}_i)$ and $\bar{q}$ is the momentum transfer with length

$$|\bar{q}| = q = 4\pi/\lambda \cdot \sin\theta, \tag{3}$$

λ being the radiation wavelength and 2θ the scattering angle. The intensity $I(q)$ is proportional to the square of the scattering amplitude

$$I(q) = K \cdot |f(q)|^2 \tag{4}$$

where K is given by the geometrical configuration, the intensity of the incident flux and the sample transmission. Normalization with respect to these parameters gives the differential cross section $d\sigma/d\Omega$:

$$\frac{d\sigma(\bar{q})}{d\Omega} = \sum\sum b(\bar{r}_i)b(\bar{r}_j) \cdot \exp\left[i(\bar{q} \cdot \bar{r}_{ij})\right] \tag{5}$$

where $\bar{r}_{ij} = (\bar{r}_i - \bar{r}_j)$. It is useful to replace the scattering length $b(\bar{r}_i)$ with the parameter $\eta(\bar{r}_i)$ describing the fluctuations from average: $\eta(\bar{r}_i) = b(\bar{r}_i) - <b>$, and defining the correlation function $\gamma_{ij} = \eta(\bar{r}_i)\eta(\bar{r}_j)/<\eta^2>$. Insert of this into equation (5) gives

$$\frac{d\sigma(\bar{q})}{d\Omega} = <\eta^2> \sum \gamma_{ij} \cdot \exp\left[i(\bar{q} \cdot r_{ij})\right] \tag{6}$$

In small-angle scattering experiments the resolution is not on atomic distances ($\sim$ Å-scale). The discrete scattering lengths can therefore effectively be replaced by a continuous function, the scattering length density $\rho(\bar{r})$, defined as the averaged value

$$\rho = \sum b_i/V \tag{7}$$

summed over an appropriate volume V, e.g., the volume of a monomer unit. Equivalently, one can define a continuous fluctuation parameter η as the deviation from average: $\eta(\bar{r}) = \rho(\bar{r}) - <\rho>$. The pre-factor $<\eta^2>$ in equation (6) is for a two phase system with scattering length ρ_A and ρ_B easily shown to be equal $(\rho_A - \rho_B)^2 = (\Delta\rho)^2$. With the summation in equation (6) replaced by an integration, we then have:

$$\frac{d\sigma(q)}{d\Omega} = (\Delta\rho)^2 \int_{\text{sample}} \gamma(\bar{r}) \cdot \exp[i(\bar{q} \cdot \bar{r})]d\bar{r} \tag{8}$$

with the integration made over the whole sample volume.

Table 2 Bulk mass densities and neutron scattering length densities for selected polymers in the amorphous state.

Polymer	*Chemical formula*	*Density* δ(g/cm^3)	*Total scattering length* $\sum b_i$(cm)	*Scattering length density* ρ(cm^{-12})
PB-1.4	$(C_4H_6)_n$	0.83	0.415×10^{-12}	0.384×10^{10}
PBd-1.4	$(C_4D_6)_n$	0.894	6.66×10^{-12}	5.98×10^{10}
PC	$(C_{10}H_{15}O_3)_n$	1.14	2.77×10^{-12}	1.04×10^{10}
PDMS	$(C_3H_6SiO)_n$	0.97	0.075×10^{-12}	0.05×10^{10}
PEO	$(C_2H_4O)_n$	1.064	0.414×10^{-12}	0.60×10^{10}
PPO	$(C_3H_6O)_n$	1.0	0.331×10^{-12}	0.343×10^{10}
PI(*cis*)	$(C_5H_8)_n$	0.913	0.332×10^{-12}	0.268×10^{10}
PMMA	$(C_4H_8O_2)_n$	1.13	0.828×10^{-12}	0.64×10^{10}
PMMA-d	$(C_4D_8O_2)_n$	1.0	9.16×10^{-12}	0.574×10^{10}
PE	$(C_4H_8)_n$	0.784	-0.333×10^{-12}	-0.28×10^{10}
PE-d	$(C_4D_8)_n$	1.06	2.0×10^{-12}	8.0×10^{10}
PP	$(C_3H_6)_n$	0.791	-0.252×10^{-12}	-0.28×10^{10}
PEP	$(C_5H_{10})_n$	0.856	-0.416×10^{-12}	-0.31×10^{10}
PEP-d5	$(C_5H_5D_5)_n$	0.92	4.79×10^{-12}	3.55×10^{10}
PEE	$(C_4H_8)_n$	0.866	-0.332×10^{-12}	-0.31×10^{10}
PEE-d2	$(C_4H_6D_2)_n$	0.90	1.75×10^{-12}	1.63×10^{10}
PS	$(C_8H_8)_n$	0.969	2.33×10^{-12}	1.31×10^{10}
PS-d	$(C_8D_8)_n$	1.04	10.65×10^{-12}	5.96×10^{10}
PVME	$(C_3H_6O)_n$	1.023	0.307×10^{-12}	0.354×10^{10}

Table 2 gives scattering length densities for various commonly studied polymers. It should be noted that the values depend on specific density and will therefore depend on temperature. The ρ-values of polymers in solution will generally also deviate from those given in Table 2. since the specific volume depends critically on solvent properties.

2.3 Contrast Variation

Small-angle neutron scattering experiments are particularly useful for studies of the detailed structures of colloidal and polymeric systems. This is done by systematic studies of systems in which the contrast is varied by exchanging hydrogen's with deuterium in specific places. In a solution study, this is most easily done by changing the composition of the solvent in terms of normal and deuterated material. While the effect of changing the contrast of an essential two-phase systems is only to change the prefactor in front of the scattering function equation (8) more complex structures with varying scattering length density will give rise to significant different form of the scattering function. Figure 2 shows schematically, how the coil conformation can be visualized by, so to say, coloring some of the polymer chains, by exchange of hydrogen's with deuterium isotopes. Figure 3 shows schematically the possible use of contrast variation to enhance different structural properties of complex particle, which could be a star-like polymer, or a micellar aggregate. Figure 4 illustrate the possibility different contrasts in a three component microemulsions, giving respectively the so-called bulk contrast and the interface contrast.

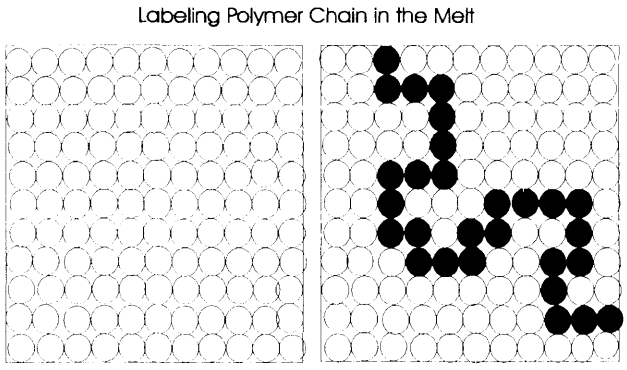

Figure 2 Schematic illustration on the deuterium labelling of polymer coils in the melt.

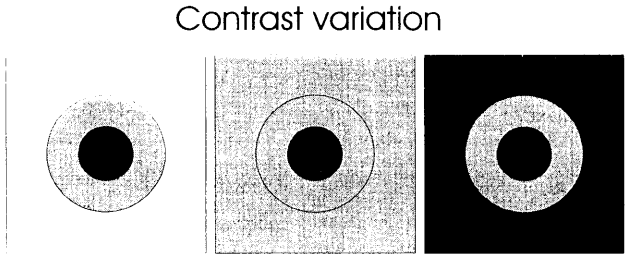

Figure 3 Schematic illustration of the use of varying the solvent contrast to visualize different segments in a complex structure, as for example a micelle.

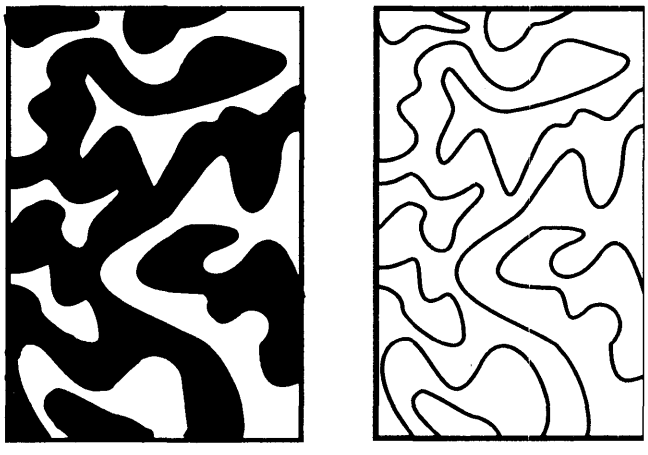

Figure 4 Schematic illustration of the use of varying the solvent contrast to highlight different properties of three-component microemulsions: bulk contrast and interface contrast.

3 Instrumentation

3.1 Neutron Sources

Neutrons are elementary particles that constitute half of the nucleus mass, or more. Each neutron has a mass of $m_n = 1.675 \times 10^{-14}$ g. In fission of specific nuclei neutrons might escape, and can be utilized for material research. The application of neutron scattering technique is based on the wave-character of such neutrons, as determined through the de Broglie relation

$$\lambda = h/m_n v_n \tag{9}$$

where h is Planck's constant and v_n the neutron velocity.

Two types of applied neutron sources exist: The reactor and the spallation type. Both types produce, at best, a beam of about 10^7 neutrons/sec/cm^2. As a consequence of the special needs and expenses involved in operation and building neutron sources, sources for neutron scattering are usually *mega science* projects that relies on international user-groups. This is also the case for national sources. Basically all major European neutron sources are in this context parts of joint European user programs.

In the reactor core fast neutrons, i.e., neutron with energy E_n of the order of 1–2 MeV, are produced in a fission chain reaction. Usually enriched uranium ^{235}U is used for fuel. Almost all reactor facilities acts as *continuous source*, providing a constant neutron flux. Examples of major reactor facilities are ILL in France, NIST in USA and JAERI in Japan. Most national neutron sources, as for example the DR3 research reactor at Risφ National Laboratory, are of the reactor type. In the reactor the core is surrounded by a moderator, that usually are made of either D_2O, H_2O or graphite. In the interaction with the moderator material, the neutrons are thermalized to the energy given by the temperature of the moderator, e.g. 50 °C. The resulting Maxwell Boltzmann distributed *thermal neutron flux* has a maximum for neutron energies $E_n = k_B T = 30$ eV, corresponding to a neutron velocity of

$$v_n = \sqrt{2k_B T/m_n} \tag{10}$$

of the order of 3000 m/s, and the neutron wavelength of the order of $\lambda = 1.4$ Å, according to the de Broglie relation equation (9).

In small angle scattering facilities, which are designed for structural studies on the mesoscopic length scale of 10–1000 Å, it is desirable to use the low energy neutrons with wavelength typically in the range 3–20 Å. In the attempt to move the peak-flux to the energy corresponding to this wavelength, *cold sources* are inserted next to the reactor core in the neutron-beam hole. The cold source is typically working with deuterium below the supercritical point, e.g., at 28 K and 15 bar. Further advances for cold beam small-angle scattering facilities are gained if the instrument is moved away from the reactor source using neutron guides. This results in highly reduction of stray neutrons, high-energy neutrons and gamma-radiation, thus resulting in a significant improved signal to background ration in the detector.

In spallation sources, the neutron beam is obtained from splintering heavy nuclei by high-energy particles such as 800 MeV protons. The protons are produced from linear accelerators, proton synchrotrons or combination of these. As in reactor sources, the produced

neutrons have high energy, which have to be reduced in a suitable moderator. The method of accelerating protons is often optimized to bursts of high-energy protons, and hence pulsed neutron beam. This is for example the case for the ISIS neutron scattering facility in UK, but continuous, or quasi-continuous, spallation sources exist as well, as for example the facility in Switzerland. The pulsed instruments provide in general a very large q-space, q being the momentum transfer equation (3), $q = 4\pi/\lambda \sin(\theta)$, through the combined determination of angle and energy. The energy is determined by time of flight.

The advantage and disadvantage of the various types of sources depends on the type of problem to be studied by neutron scattering. Small angle scattering is generally best performed at reactor sources. This is mainly a consequence of difficulty in the determination of background in the form of incoherent scattering from the sample itself. The pulsed sources have, on the other hand, possibilities for better high-resolution data. The probably best instrument would be to use a pulsed spallation source, where the beam is monochromatized. Such instruments have been proposed for the European ESS project.

3.2 Small-Angle Neutron Scattering Instrument

The small-angle neutron scattering instrument is in essence rather simple, consisting of the four units: monochromator, collimator, sample environment, and flight tank for the scattered beam with a neutron detector. In addition to these units, the instrument includes electronics for data acquisition and software for data treatment.

3.2.1 Monochromator

Neutrons with a particular wavelength can be extracted from the 'white' beam of the neutron source by monochromators. In pulsed facilities, the obvious way is to use time of flight, even though additional monochromatization may be useful as discussed above. For continuous sources, the monochromatisation is essential. Two basic different techniques are used, given by the two dual properties of the neutron, respective wave and particle properties. Using the wave nature of the neutrons, a particular wavelength can be selected *via* Bragg scattering from a crystal with suitable crystal lattice spacing, d. Moreover, a high reflectivity is needed, and to match the general resolution of the instrument, a relative high mosaic spread is favored, i.e., a crystal with some spread in the crystal orientation, thus fulfilling the Bragg condition for neutron wavelength within some limited band. Typically, pyrolitic graphite is used as crystal monochromators, giving wavelength spread up to about 6% centered around the nominal value.

Alternatively, one can use the particle nature of the neutrons to choose the appropriate neutron velocity, and thereby given wavelength. The velocity of neutrons of 6 Å, as an example, is 600 ms^{-1}. This relative low speed allows the use of mechanical selectors made up of rotating plates of neutron absorbing materials. Those neutrons with too low speed will be absorbed from the selector from the back, while those with too high speed will hid the selector plate in front. Mechanical selectors are usually made as slightly screwed turbine like devices. The screw angle and the distance between the plates define the wavelength spread, while these parameters and the speed of revolution give the nominal wavelength. By changing the axis of rotation relative to the beam direction, additional possibility for variation of wavelength spread is possibly. At the SANS instrument at Risφ National Laboratory, such possibility gives the freedom of wavelength spread from 9% and up. When structures with relative sharp features are measured, as for example an ensemble of monodisperse particles or ordered structures, 9% wavelength resolution should be

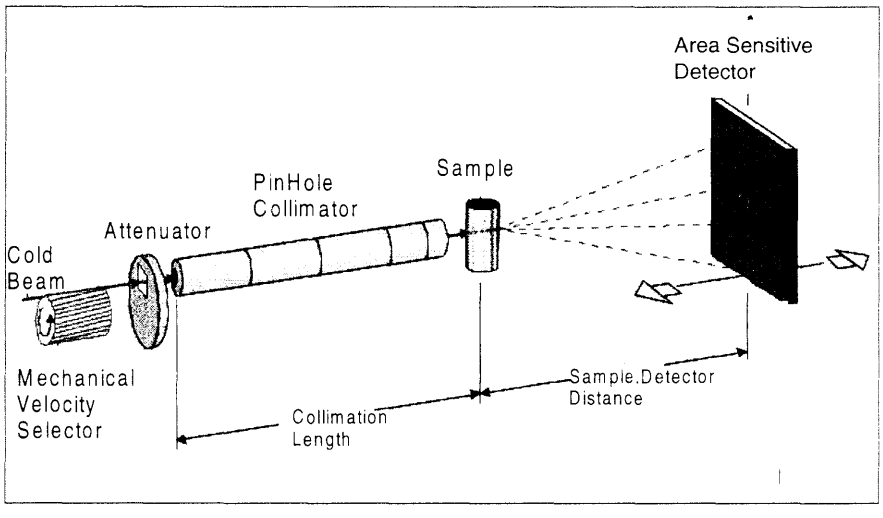

Figure 5 Schematic drawing of small-angle neutron scattering instrument.

used, whereas 18% resolution typically is used for more feature less structures like Gaussian chains. Wavelength spread of 36% has been used in very special cases where the experiment was limited by extremely low scattering contrast.

3.2.2 Collimation

The neutron beam direction is defined by the collimator, which in principle can be given by just two pinholes, one near the source point, and one near the sample. In practice the SANS facility is often equipped with a variable length of the collimator as well as variable pinhole sizes. The effective length is varied by inserting sections of neutron guides between the source (or the monochromator) and the sample. Such neutron guides are glass channels coated with Ni or super-mirrors reflecting neutrons with wavelength above a certain critical value (typically more than 3 Å, depending on the Ni-isotope that is used, or the design of the super-mirror). As an example, a 10 meter collimator with 2 cm diameter pin-hole at the entrance, and 1 cm diameter pinhole near the sample corresponds to a beam divergence of 0.1°.

3.2.3 Neutron Detector

Most SANS facilities today are equipped with area-sensitive neutron detector that is positioned in a large flight path tank.

The detector is usually of the multiwire type, with ^{3}He as the active gas for neutron detection. ^{3}He capture neutrons through the nuclear process

$$n + {}^3\mathrm{He} \rightarrow {}^3\mathrm{H} + {}^1\mathrm{H} + 0.76\,\mathrm{MeV}$$

producing tritium ^{3}H and protons ^{1}H. Alternative gasses or materials based on either ^{10}B of ^{6}Li can be used as neutron detection system. In the gas detector there is in addition an ionisable gas of for example mixed argon and methane. A plane of wires mounted in the center of the detector, the anode plane, is based at a high tension (3–5 kV). The positive protons and trition nuclei produce a trace of ionized Ar-gas that is accelerated toward this anode plane, thereby producing an amplified charge signal. The charges are absorbed in the anode and distributed toward an electronic system, which determines the one coordinate of the position of the incoming neutron. An additional plane, the cathode plane next to the anode, gets by inductive coupling an electronic pulse of opposite sign, which with appropriate design of the planes can be used to determine the second coordinate.

The gas detector has a limited capability in terms of neutron flux and spatial sensitivity. For SANS detectors with diameter of the order of 50–100 cm, the typical spatial resolutions are within the 0.5 to 1 cm range. Deadtime problems starts to become significant for count rates of the order of 10^4–10^5 counts/sec when distributed over the whole detector, whereas count rates within a few pixels normally should be limited to a few thousands.

The signal from the neutron detector is analyzed electronically, and saved in an histogram memory for further data treatment.

3.3 Small-Angle X-Ray Scattering

The present chapter is focused on the use of neutron radiation for the small angle scattering. Since much of the presentations will be appropriate for x-ray scattering as well, however, will we include a very brief introduction to the types of instruments that is used for small angle x-ray scattering, SAXS.

In instruments using conventional x-ray tubes as the source, the Kratky type of SAXS instrument is the most frequently used [7]. This type of instrument has optimized the flux and resolution using slit geometry for collimation and simple filter for monochromatization. The detector is a point detector or a linear sensitive detector. The Kratky-apparatus is often sufficient for solution studies where the scattering objects are not too anisotropic in shape. The Kratky instrument has also successfully been used in studies of polymers and colloids with liquid crystalline order, but due to the extreme anisotropic resolution function it may cause significant problems in such samples. Texture can give rise to misleading values of scattering vector q.

In x-ray sources of high power rotating anodes and synchrotron facilities, pin-hole configuration is usually used in the SAXS instrument. In these systems the collimation consists of two pinholes to define the beam, one near the source, and a second relative near the sample. A third pinhole is usually needed between the defining pinhole and the sample to reduce parasitic scattering and Fraunhofer diffraction from the slits. The monochromatization is obtained using Bragg-scattering from single crystals, and an area sensitive detector detects the scattered photons. There exist a variety of area-sensitive x-ray detectors. The type which is most commonly used in SAXS-instruments is a gas detector which function very similar to the neutron detector described above, but where the ionizing gas interact directly with the x-ray photons. There are different possibilities of gasses, including argon and xenon. Another detector type, which in recent years has been extensively used, is the image plate detector. This detector function in principle as photographic film, but the pattern is read out electronically, and the detector is re-useable. The image plate detector has a spatial resolution and dynamic range that is significant better than the gas detector, but the need for real-time display makes anyway the wire detector more appropriate in most cases. Some instruments use CCD devices for x-ray detection. These are still rather rare, but will most probably be of importance in the future.

3.3.1 Sample Environment

Typical scattering experiments on polymer melts and solutions concern investigation of structure and structural changes versus temperature, pressure, shear or other external fields. The investigation can involve detailed examination of an ordered mesophase with the aim to determine the crystal structure, or to give details on the phase behavior near a critical point.

In general a high quality temperature control is needed to be adapted to the scattering facility. Typical temperature ranges are within the range –20 to 300 °C, but depending on the polymer, of cause. Typical limitations coming from the polymer systems concern at the low temperature limit the glass transition temperature, and at high temperatures the polymer stability against degradation, stability against cross-linking, and possibility of solvent evaporation.

Another thermodynamic parameter, which in recent years has proven important for the understanding of polymer phase behavior, is a pressure device possibly combined with temperature regulation. Pressure devices, which are presently available, are typically limited to approximately 2000 bar, but pressures beyond this limit would certainly be interesting for future studies.

Shear devices have proven to be extremely important for block copolymer studies, that during processing can show dramatic change in phase behavior, texture etc. This is for example the situation in extruders used in polymer industry. In the scattering experiment, shear can be used both to study hydrodynamic changes of polymer coil conformation related to shear and stress, and possibly changes in miscibility parameters and thereby phase transition temperatures. Shear have in addition proven extremely useful for making monodomain ordered structures suitable for crystallographic studies, for example after mounted on a goniometer.

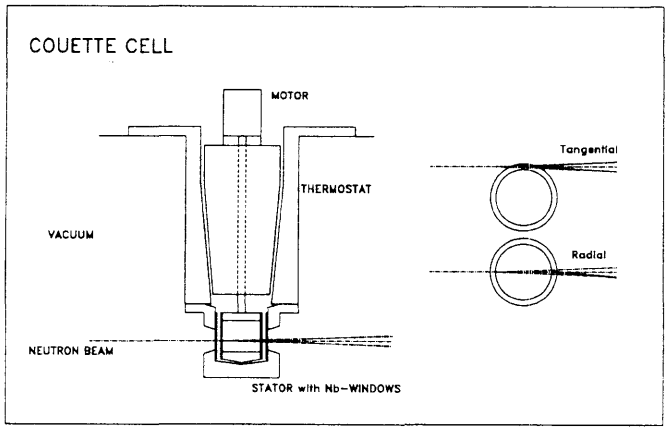

Figure 6 Schematic drawing of a Couette-shear device for *in situ* small-angle neutron scattering. The two configurations shown are typically applied: radial through the cell and tangential through the cell.

Figure 6 shows schematically a shear devices of the Couette type, used for SANS experiments. The two commonly used configurations are included: the beam going radially through the cups giving the (e, v)-scattering plane, and the beam tangentially to the shearing cups:, giving the (e, ∇)-scattering plane, where v is parallel to flow velocity, ∇ is parallel to shear gradient and e is the neutral vorticity axis.

Figure 7 shows a commercial parallel plate shear instrument (RSA2 from Rheometrics) modified for *in situ* SANS experiments.

In addition to shear, stretching devices can be useful both in the attempt to mimic problems in practical applications, and to obtain additional microscopic understanding.

4 Data Reduction

4.1 Basic Background Treatment and Normalization

The measured scattering intensity $I_m(q)$ is related to the differential scattering cross section per unit sample volume, $\partial\sigma/\partial\Omega$,

$$I_m(\bar{q}) = I_o \Omega_o \epsilon A d_s t_s (\partial\sigma/\partial\Omega) \tag{11}$$

where I_o is the neutron flux, Ω_o is the solid angle of acceptance of the detector, ϵ is the detector efficiency, A is the area of the beam, d_s is the sample thickness ($A \cdot d_s$ is sample volume), and t_s is the neutron transmission through the sample. The differential cross section $\partial\sigma/\partial\Omega$ is often also termed the scattering function, and has the unit of cm^{-1}.

The terms I_o, Ω_o, ϵ, and A is often kept constant for a given series of measurements. It is assumed that the transmission is the same for all scattered neutrons, which is effectively fulfilled for plate-like shape of homogeneous samples, since the flight path through the sample is basically the same for scattering into small angles.

The contribution from background (e.g., from container) and electronic noise must be subtracted to get the scattering form the 'sample' itself.

It is not always trivial how to obtain a relevant background measurements. In the case of relative low concentration of particles dispersed in a liquid, the background spectrum I_b is a measure of the container with pure solvent.

An additional background term I_e may arise from electronic noise in the detection system, and from stray neutrons from other sources than that of the sample scattering. This term is measured with the beam blocked at the sample position, typically using boron-containing plastics.

Taking the transmission factors into account, the scattering intensity from the sample is then given as

$$\tilde{I}_s = I_m - \frac{t_s}{t_b} I_b - (1 - \frac{t_s}{t_b}) I_e \tag{12}$$

where t_s, t_b are the transmission factors of respectively sample including possibly container and solvents, and

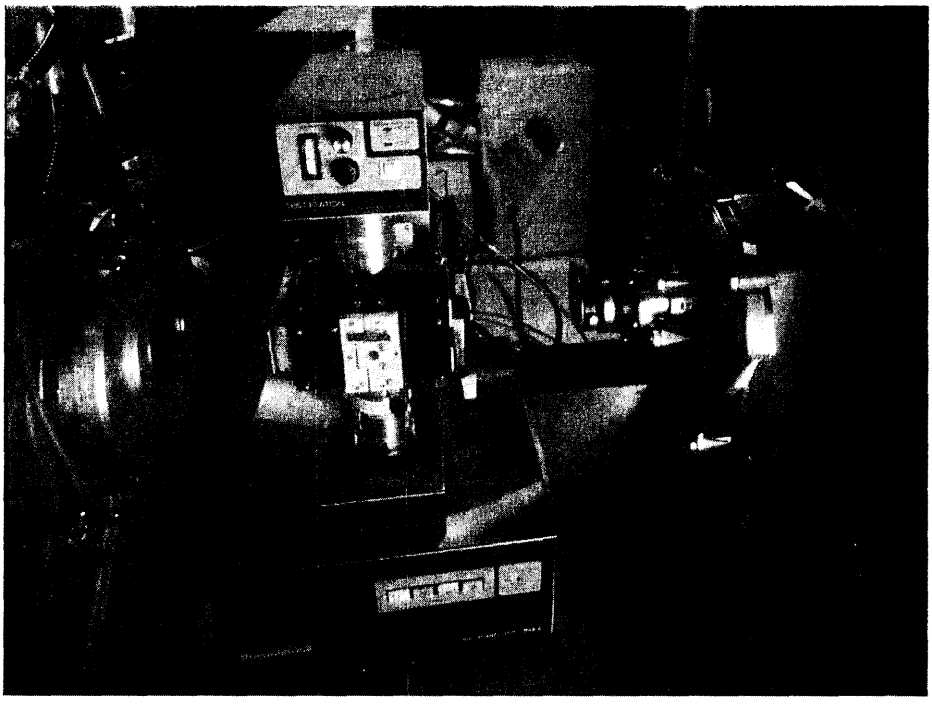

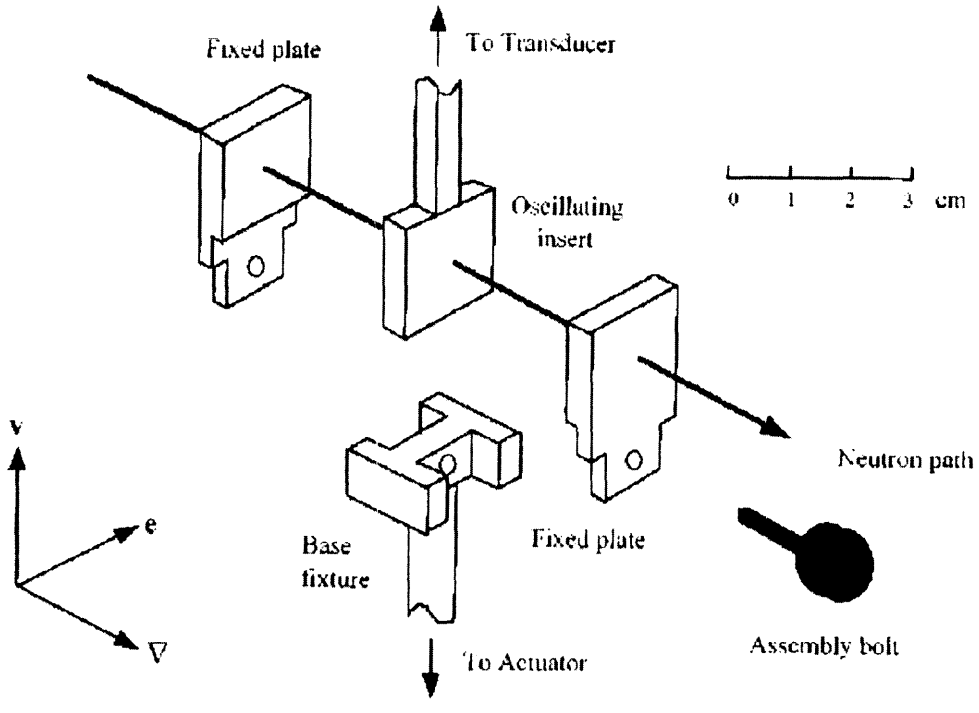

Figure 7 Commercial rheological instrument modified for *in situ* mechanical and scattering studies. The figure shows the RSA2 (Rheometrics) which is a parallel plate device (Photo B. Koch).

pure background conditions. The pre-factor $(1 - t_s/t_b)$ in front of the last term I_e is needed since part of the 'electronic noise' already is included in the second measured term I_b.

The calibration into absolute units are most easily done using a secondary standard [8, 9]. Often one uses a standard where the scattering is totally dominated by the incoherent term, giving a well defined flat spectrum. Such materials can, for example, be plain water or lupolen (a special polyethylene) where the scattering at low angles is dominated by the incoherent cross-section of hydrogen. Using water, as a relevant example, one

Table 3 Correction parameter g relative to isotropic scattering from water.

λ	2 Å	3 Å	4 Å	5 Å	6 Å	7 Å	8 Å	9 Å	10 Å
g	1.84	1.63	1.48	1.33	1.24	1.15	1.11	1.05	1.00

may assume that all neutrons that interact with the hydrogens, i.e., the fraction $t_c(1 - t_w)$ is scattered into the space angle 4π, t_c and t_w being the transmission through the water container and the water, respectively. The isotropic scattering into 4π is not totally correct. The recoil of atomic nuclei in collisions with neutrons causes the incoherent scattering to be strongest in the forward direction, and falls off with angle. Also the sample geometry favors in general forward scattering, if multiple scattering takes place. These contributions, so so-called g-values, can be measured. They will be slightly dependent on instrumental specifications. Table 3 gives the g-values as measured by Jacrot and Zaccai for D11 at ILL [9]. Using water for normalization, the scattering function is then given in absolute units as:

$$\frac{\partial\sigma}{\partial\Omega} = \frac{\tilde{I}_s}{\tilde{I}_w} \cdot \frac{1}{t_s}\frac{1}{d_s}\frac{t_c(1-t_w)}{4\pi} \cdot g \tag{13}$$

where the water-normalization spectrum, $\tilde{I}_w$, in analogy with equation (12) is calculated based on measured spectra according to

$$\tilde{I}_w = I_w - \frac{t_w}{t_c} I_c - (1 - \frac{t_w}{t_c}) I_e. \tag{14}$$

I_c being the scattering intensity of the empty container (quartz cuvette).

4.2 Data Interpretation

In the expression for the scattering function $d\sigma/d\Omega$ in equation (8), the integration is over the whole sample volume. In some cases it is possibly, and advantageous, to split the interpretation of the scattering function into a part with the origin in intra-particle correlations, and a part describing inter-particle correlations. For a monodisperse ensemble of scattering objects, particles, the integration of the correlation function, equation (8), can be simple split into such an intra-particle self-correlation term and an inter-particle correlation, as

$$\frac{d\sigma(\bar{q})}{d\Omega} = n_v \cdot V^2(\Delta\rho)^2 \cdot \int_{\text{intra}} \gamma(\bar{r}) \exp\left[i(\bar{q}\cdot\bar{r})\right] d\bar{r} \cdot \int_{\text{inter}} (\gamma(\bar{r}) - 1) \exp\left[i(\bar{q}\cdot\bar{r})\right] d\bar{r} \tag{15}$$

where n_v is the number density of particles, and spherical symmetry is assumed. The first integral in equation (15) determines the normalized particle form factor, $P(q)$, and the last integration term gives the inter-particle structure factor, $S(q)$. The scattering function can thus be written

$$\frac{d\sigma(\bar{q})}{d\Omega} = n\Delta\rho^2 V^2 P(\bar{q}) S(\bar{q}) \tag{16}$$

In very dilute systems the inter-particle correlation's vanishes ($S(\bar{q}) \simeq 1$) and the particle form factor is accordingly determined directly from the scattering function.

For an ensemble of objects with some size distribution, different approaches have been proposed to obtain the average particle size and size-distribution from the experimental scattering function. Kotlarchyk and Chen [10] proposed the 'decoupling approximation' in which it is assumed that the position of the particles is independent of their sizes, and that the interference effects can be described by an effective structure factor calculated for the average size of the particles. The scattering function has then exactly the same form equation (16) as given above for monodisperse systems, but the form factor, $P(\bar{q})$, is replaced by the weighted mean average, $\tilde{P}(\bar{q})$:

$$\tilde{P}(\bar{q}) = < V^2 P(\bar{q}) > / V^2, \tag{17}$$

and the structure factor is modified by a term, $\beta(q)$, that takes into account the influence of polydispersity effects:

$$\tilde{S}(\bar{q}) - 1 = \beta(\bar{q})[S(\bar{q}) - 1] \tag{18}$$

The method of Kotlarchyk and Chen gives good results for relative narrow size distributions. Pedersen suggested a different approach [11], the 'local monodisperse approximation', in which it is assumed that the system can be divided up into subsystems of monodisperse ensembles. The total scattering function is then the simple sum over these systems weighted by a given size distribution function, $D(R)$:

$$\frac{d\sigma(\bar{q})}{d\Omega} = (\Delta\rho)^2 \int D(R) V^2(R) P(\bar{q}, R) S(\bar{q}, R) dR \tag{19}$$

4.3 Fit to Model Function

In the attempt to obtain real-space structural information from the measured scattering function, various approaches may be used. For a dilute collection of identical, randomly oriented aggregates, the scattering function equation (8) gives

$$\frac{d\sigma(q)}{d\Omega} = (\Delta\rho)^2 4\pi n_v \int r^2 \gamma(r) \cdot \frac{\sin(qr)}{qr} dr \tag{20}$$

where n_v is the number of particles per volume. At q-values small compared to the inverse of the characteristic length of the scattering object, the $\sin(qr)/(qr)$-function may be expanded into a series in qr, thereby giving the Guinier approximation

$$\frac{d\sigma(q)}{d\Omega} \propto \exp\left[-R_g^2 q^2/3\right] \tag{21}$$

where the radius of gyration R_g is defined as

$$R_g^2 = (1/2) \cdot \int \gamma(r) r^4 dr / \int \gamma(r) r^2 dr \tag{22}$$

A closely related approximation is the Zimm-approximation, which limits the expansion to second order in qr:

$$[\frac{d\sigma(q)}{d\Omega}]^{-1} = [\frac{d\sigma(0)}{d\Omega}]^{-1} + \ell^2 q^2. \tag{23}$$

The Zimm approximation is discussed in further details below in the parts describing scattering studies of polymer blends, section 7.

More generally, the measured scattering function might be related to a real-space model of which the structure factor can be described analytically: $I_{model}(q)$. The appropriate model function can then be obtained through a fitting routine that minimizes the least square residual χ^2 between the measured and model values:

$$\chi^2 = \sum_{i=1}^{N} (\frac{I_{exp}(\langle q_i \rangle) - I_{model}(\langle q_i \rangle)}{\sigma_i})^2, \tag{24}$$

where the index i refers to the number N of measured pixel values, and σ_i are experimental standard deviations. In the sections below, a number of relevant model functions will be presented in connection to specific polymer systems.

Instrumental smearing influences always experimental scattering data, and it may be necessary to include correction for this in the data analysis. Owing to the finite resolution of the instrument the scattering in a region around the nominal scattering vector $<q>$ is probed. For small-angle neutron scattering, the distribution of scattering vectors q can be described by a resolution function $R(\langle q \rangle, q)$ [12], and the smearing can hereby be taken into account in the model function, thus given as

$$\tilde{I}_{model}(q) = \int R(\langle q \rangle, q) I_{model}(q) dq \tag{25}$$

An example of such data analysis applied on block copolymers is given in Figure 29 in section 8.

4.4 Indirect Fourier Transformation

In the scattering function equation (20), valid for a dilute collection of identical, randomly oriented aggregates, the term $r^2\gamma(r)$ is the distance distribution function, $p(r)$, which in principle can be determined from a Fourier transformation of the measured cross-section. Since the experimental data, however, are measured in only a limited range of q and are affected by statistical noise, such Fourier transform is not practical applicable. Glatter proposed an alternative method to determine the pair distribution function, namely the so-called *Indirect Fourier Transform* [13], in which $p(r)$ is expressed as a linear combination of cubic b-spline functions $B_i(r)$:

$$\gamma(r) r^2 \equiv p(r) = \sum_{i=1}^{M} a_i B_i(r) \tag{26}$$

The expression equation (26) is inserted in equation (20), and the coefficients a_i are determined by least square methods. This indirect Fourier method uses only the measured data, and there is no need for extrapolation to low and high q-values. It is moreover easy to include instrumental smearing in the data analysis [14]. In practice, typically 50–80 spline functions are needed to give $P(q)$ with a reasonable resolution. This is, however, far beyond on number of independent parameters that are statistically allowed. In the attempt to limit the number of fit-parameters a_i, Glatter proposed to use a smoothness constraint in the χ^2-statistical method [13].

$$N_c = \sum_{i=1}^{M-1} [a_{i+1} - a_i]^2 \tag{27}$$

such that $\chi^2 - \lambda N_c$ is minimized rather than χ^2 itself. The weight of constraint is given by the parameter λ which can be determined objectively from the point-of-inflection method of the residual when given versus λ.

5 Polymer Conformation

The conformation of polymer chains in the melt, or in solution, have dramatic influence on mechanical and other properties of the materials. The classical question raised is whether the coil conformation in the melt is highly entangled, or not, as illustrated in Figure 8.

The conformation can in the melt be measured in a neutron scattering experiment by deuterium labeling some of the chains. Figure 2 shows schematically the essence of such labeling.

For small fraction ϕ of labeled polymers, the measured scattering is due to individual chains, thus giving the scattering function of the coil $P(q)$ according to the previous discussion related to equation (16). When ϕ is larger, however, one also find that the measured intensity directly probes the single chain conformation. The argument is that since the intensity involves only pair correlations, $I(q)$ must be a polynomial in ϕ of second order [15]:

$$I(q) \propto \phi P(q) + f^2 h(q), \tag{28}$$

where $h(q)$ is yet unknown. Here, however, we can impose the condition that for $\phi = 1$, as well as for $\phi = 0$, we will get no scattering. This means that $h(q) = -P(q)$ and thus

$$I(q) \propto \phi(1 - \phi) P(q). \tag{29}$$

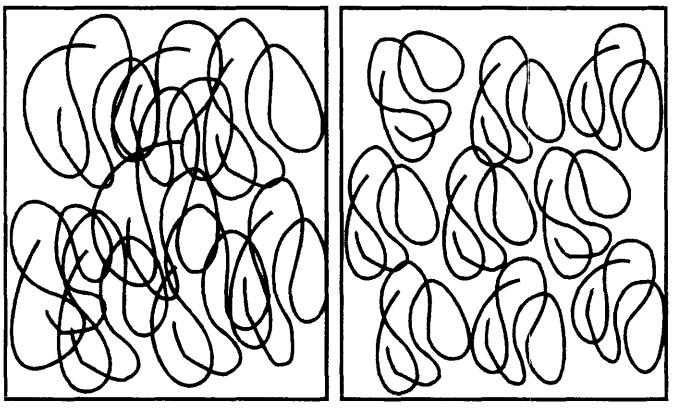

Figure 8 Schematic illustration of different possibly polymer chain conformation and degree of entanglement.

This argument assumes that the mutual interaction between any monomers, deuterated or not, is the same. For the measurement of polymer coil conformation in the melt, one might then argue that the optimal experimental conditions are that of about 50% deuterated molecules, giving the best signal to noise ratio.

In practice, however, even the minor difference between a polymer and its deuterium analogue might lead to phase separation, or significant composition fluctuations (see the section on polymer blends, 7) that will significantly limit the reliability in measuring polymer sizes. Furthermore, major amount of hydrogens in the sample will give substantial incoherent background. An optimal mixture to measure coil conformation in a polymer melt is therefore to use a blend of dominating deuterated material, and typically or the order of 2–5% non-deuterated polymers.

Neutron scattering experiments have proven that polymers approach the conformation of a random walk in the melt when the molar masses are sufficiently large. This conformation is often referred to as the *ideal* or the *Gaussian chain* conformation.

The mean polymer end-to-end distance, R_{ee}, is given relative to the persistence length, i.e., the step size in the random walk, a, and the number of steps N. For large N-values, the Gaussian statistics or the random walk gives the simple scaling relation between R_{ee} and N [15]:

$$R_{ee}^2 = Na^2, \tag{30}$$

The polymer radius of gyration, R_g, equation (22) which can be simple measured as the slope of ln $(I(q))$ plottet versus q^2 according to the Guinier approximation equation (21), takes correspondingly the form:

$$R_g^2 = \frac{1}{6}Na^2. \tag{31}$$

For the ideal chain, R_g scales accordingly with the square-root of the degree of polymerization N (see e.g., [15])

$$R_g \propto N^{\frac{1}{2}} \text{ or } R_g \propto M^{\frac{1}{2}}, \tag{32}$$

where M is the molar mass. Polymers show always a finite size distribution even though synthesis using ionic polymerization techniques today can provide polymers with rather well-defined molar masses. Different statistical average of the molar masses appear as the relevant depending on the physical phenomena. The most important are:

$$M_n = \sum n_i M_i / \sum n_i \tag{33}$$

$$M_w = \sum n_i M_i^2 / \sum n_i M_i \tag{34}$$

$$M_z = \sum n_i M_i^3 / \sum n_i M_i^2 \tag{35}$$

It appear from the definition of R_g, equation (22), that the radius of gyration of ideal polymer chains is related to the w-averaged mass, M_w: $R_g \sim M_w^{1/2}$.

Equation (32) is an example of fractal structure, *viz.* $M \propto R^{d_f}$, where the fractal dimension d_f in this random walk configuration is $d_f = 2$. In scattering experiments, fractal structures have a most simple form. The correlation function obey $\gamma \sim M/V \sim r^{d_f}/r^3$, which inserted into equation (8) simply reduces to

$$\frac{d\sigma(q)}{d\Omega} \propto q^{-d_f}, \tag{36}$$

Thus, the fractal dimension appears directly as the slope of the scattering function when represented in a double logarithmic plot.

To a first approximation the scattering function measured at a given q-value probes structural properties on the $1/q$-length scale. In the q-range between the reciprocal values of radius R_g and segment length a, the scattering functions thus reflects the local conformation inside the coil which is exactly given by the fractal statistics, i.e.,

$$I(q) \sim q^{-2} \text{ for } 1/R_g \ll q \ll a$$

for the random walk configuration.

The full form factor of ideal chains can be calculated analytically based directly on the definition of the form factor equations (15, 16)

$$P(\bar{q}) = \int_{\text{particle}} \gamma(\bar{r}) \exp(-i\bar{q} \cdot \bar{r}) dr \tag{37}$$

giving the Debye function $g_D(q)$:

$$P(\bar{q}) = P(q) = g_D(q) = \frac{2}{x^2}\left[x - 1 + \exp(-x)\right] \tag{38}$$

where

$$x = q^2 R_g^2.$$

Figure 9 shows an example of the scattering function of a polymer chain, including a fit the Debye function [16].

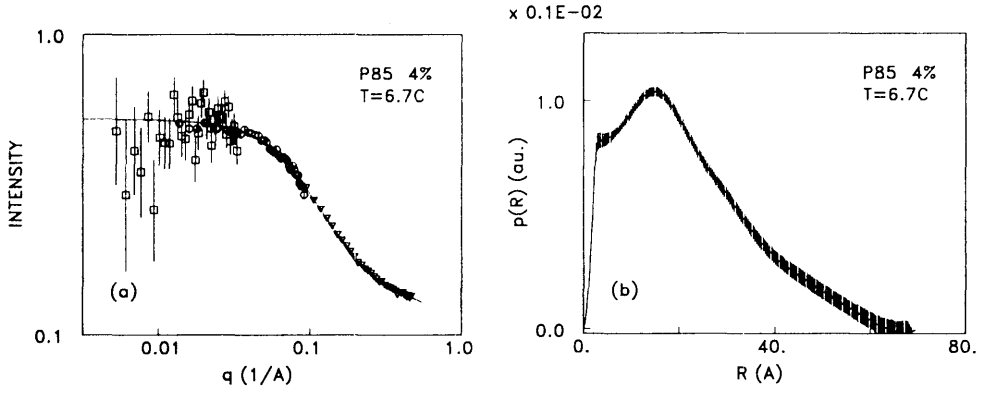

Figure 9 (a) Scattering function of polymer chains (PEO-PPO-PEO in water). The solid line represents fit to the Debye function. (b) The pair correlation function as obtained by indirect Fourier method from the experimental data. The $p(R)$-function shows correlations to relative large distances, characteristic for the open structure of the ideal chain. (reference Mortensen and Pedersen, *Macromolecules*, **1993**; 26: 805.

The figure also include the pair correlation function, as obtained using the fitting procedure of indirect Fourier transform, described in section 4.4.

In solutions, the polymer coil conformation depends on the solvent quality. For so-called θ-solvents, the difference in interaction between solvent molecules and polymers, and mutual polymer interaction vanishes, and the chain approach for large molar sizes the conformation of the random walk discussed above for melts.

In good solvents the polymer coil will swell and the structure approaches the conformation of a *self-avoiding random walk*, SAW, which can be shown to follow the scaling law (see e.g., [15]):

$$R_g \propto N^{\frac{3}{5}} \text{ or } R_g \propto M_w^{\frac{3}{5}}, \tag{39}$$

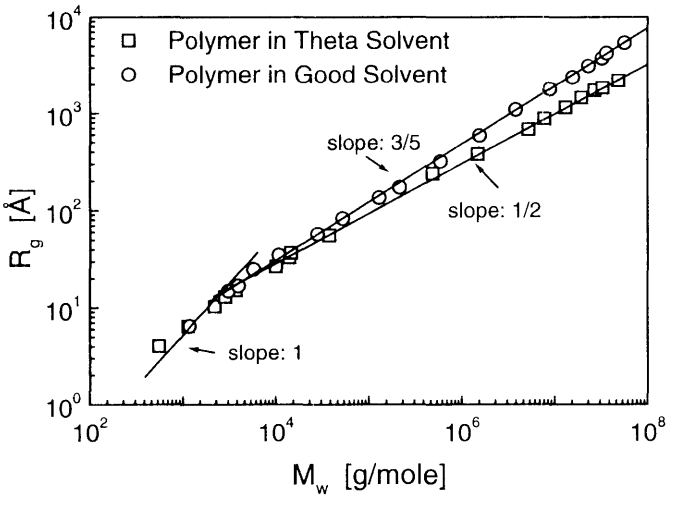

Figure 10 Polymer radius of gyration, R_g versus molar mass as measured in a θ solvent and in a good solvent (Data from Miyaki *et al.*, *Macromolecules*, **1978**; 11: 1180; Kiste *et al.*, *Die Macromol. Chem.*, **1969**; 121: 174; Huber *et al.*, *Macromolecules*, **1985**; 18: 1461; Ballard *et al.*, *Polymer*, **1976**; 17: 349).

i.e., the fractal dimension is $d_f = 5/3$. In dilute solutions the structure of polymer chains can be measured in a scattering experiment. Figure 10 shows results of a series of such experiments giving the polymer coil size R_g versus degree of polymerization [17–20]. The conformation approaches the two scaling laws: the random walk (ideal chain) obtained; θ-solvents, and the self-avoiding random walk in good solvents for polystyrene molar masses above approximately 10 kg/mole. For small molar masses the near linear relationship between R_g and M_w reflects a relative stiff, rod-like structure.

5.1 Semidilute Polymer Solutions

As the concentration of polymer chains in the solution grows, it passes through three characteristic concentration regimes: (i) the dilute solution (which is included in the discussion above), in which the individual coils do not overlap, (ii) the semi-dilute solution where coils are strongly overlapping but the volume fraction of polymers are still small, and iii) the concentrated solutions. The dilute and semidilute regimes are illustrated in Figure 11.

The crossover between dilute and semidilute is determined by the concentration c^*, which can be estimated by simple arguments: the crossover value must follows the relation

$$c^* \propto N/V_P, \tag{40}$$

where V_P is the swollen volume that the polymer chain expels, i.e., of the order of R_g^3. Using the relations between R_g and N, equations (32) and (39), equation (40) thereby gives the crossover concentrations

$$c^* \sim N^{-1/2} \text{ for ideal chains} \tag{41}$$

and

$$c^* \sim N^{-4/5} \text{ for chains where excluded volume} \tag{42}$$

effects are important.

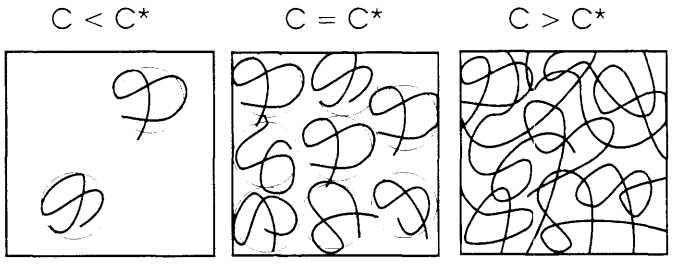

Figure 11 Illustration of the three concentration regimes of polymers in solutions: dilute: $c < c^*$, cross-over regime: $c \simeq c^*$, and semidilute: $c^* < c \ll 1$.

In the semi-dilute regime, $c^* < c \ll 1$, the structure is characterized by the length, ξ, of correlated concentration fluctuations. For distances less than this correlation length $r < \xi$ the mass distribution obeys the fractal scaling $M(r) \sim r^{d_f}$ with dimension d_f given by the *goodness* of the solvent (equations (32, 39)), and the scattering function is correspondingly given as $I(q) \sim q^{-d_f}$ for $q\xi > 1$ (see equation (36)). For distances $r > \xi$, the semidilute solutions look like a close-packed system of blobs with size ξ. In a simple picture this ξ can be viewed as the mesh-size of the temporary polymer network. The concentration fluctuations are correlated inside each blob, but uncorrelated with respect to any other blob [15]. The scattering function reflecting this regime, i.e., $q\xi < 1$ obeys Lorentzian profile [15]:

$$I(q) \simeq \frac{c^2\xi^3}{1 + q^2\xi^2}. \tag{43}$$

Falcao *et al.* found imperically that the function P_{blob} [21]

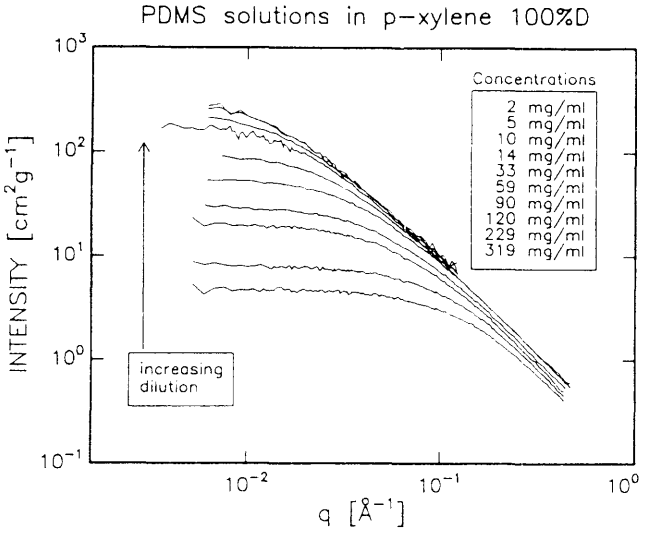

Figure 12 Experimental SANS scattering pattern of PDMS polymers in good solution (p-xylene), as obtained at different concentrations ranging from dilute into the semidilute regime (reproduced from Falcao *et al.*, *Macromolecules*, **1993**; 26: 5350).

$$P_{\text{blob}} \simeq \frac{(1 + q\xi)^{1/3}}{(1 + q^2\xi^2)} \tag{44}$$

describes the experimental scattering from semidilute polymer solutions very well over the entire measured q-range, including both inter-blob ($1/q > \xi$) and intra-blob correlations ($1/q < \xi$).

Figure 12 shows an example of a series of SANS data of polymers of poly(dimethylsiloxane), PDMS, in p-xylene solution, as obtained at concentrations ranging from dilute into the semidilute regime. The scattering functions are normalized relative to the polymer concentrations. The patterns at lowest concentration are in agreement with the Debye function and essentially concentration independent. The high-q scattering function approach the common function $I \sim q^{-d_f}$ reflecting the unperturbed local structure of the chains, the intra-blob correlations. The low-q part of the scattering function follows for concentrations above $c \sim c^*$ the Lorentz-function equation (43), thus giving the concentration dependence of the correlation length $\xi(c)$.

The average polymer concentration, valid for all scales greater than ξ, is

$$c \sim m(\xi)/\xi^3 \tag{45}$$

where $m(\xi)$ is the mass inside the blob, i.e., $m(\xi) \sim \xi^{d_f}$. For polymers in good solvents, $d_f = 5/3$, this gives $c \sim \xi^{5/3-3} = \xi^{-4/3}$, and thereby

$$\xi \sim c^{-3/4} \tag{45}$$

in very good agreement with experiments [22, 21]. Figure 13 shows the correlation lengths as obtained from the scattering functions given in Figure 12, showing the agreement with the simple scaling arguments for $c > c^*$, and ξ constant equal $R_g/\sqrt{3}$ for $c < c^*$.

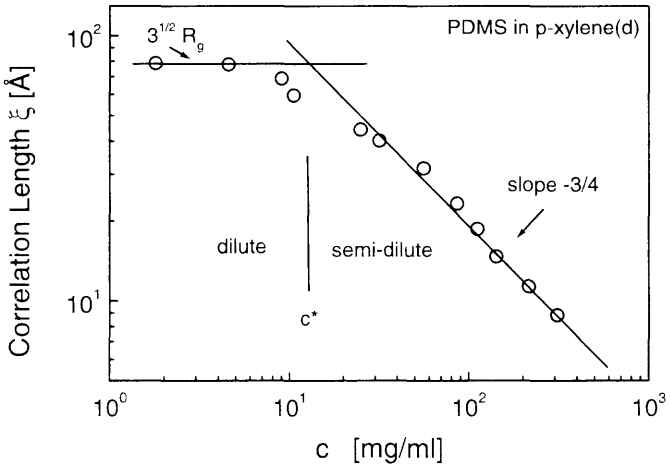

Figure 13 Correlation length ξ_s as a function of polymer concentration, showing the 3/4-scaling for $c > c^*$ and ξ_s constant (given by R_g) for $c \ll c^*$. The data are for PDMS in p-xylene (reproduced from Falcao *et al. Macromolecules*, **1993**; 26: 5350).

6 Polymer Networks

Cross-linking polymer chains creates, above a certain cross-link density, a macroscopic network of connected polymer strands. Upon cross-linking, the mechanical properties change from liquid like to solid-like behavior. The detailed macroscopic properties, like frequency dependence of the elastic and the loss modulii are to a large extent determined by the density and distribution of cross-links, and the related molar masses characterizing the polymer strands between neighboring cross-links. Small-angle scattering can be used to reveal such microscopic structural characteristics, and thereby provide the basis for detailed understanding between microstructure and final properties.

Classical network models are typically based on the assumption that the network strands in between cross-links conform according to Gaussian statistics (see section 5), and assume, for example, that a macroscopic deformation is accomplished by deformation of each polymer chain.

Swelling experiments have shown, however, that the local conformation of the individual strands is only slightly changed when the network is swollen to even large extent [23, 21]. The classical model also fails to explain several stretching experiments.

Typical scattering measurements on networks are those of polymer melts, where a few chains are labeled using the exchange of hydrogen with deuterium, as discussed above (see Figure 2). Such experiments have revealed the response of polymer chain conformation when stretched, and possibly relaxation after deformation.

The structure of networks swollen in a good solvent can be studied in analogy with studies on semidilute polymer solutions, as discussed above, section 5.1. It is advantageous formally to express the scattering function as the product of a form factor and a structure factor, according to the rule $I(q) \sim P(q)S(q)$, equation (16), discussed in section 2. The form factor is here associated with the blob structure of a semidilute polymer solution with characteristics similar to the swollen gel. The structure factor describes fluctuation in blob densities, and appear to be well describes as being fractal for length scales less than an upper characteristic value, ξ_l, and homogeneous when gauged with length scales $q^{-1} > \xi_l$. Texeira have shown that the scattering function of such fractal objects with an upper cut-off length ξ_l, can be given in the form [24].

$$S_{\text{fractal}}(q) = \tilde{1} + \frac{1}{(qr_o)^{d_l}} \frac{d_l \Gamma(d_l - 1)}{[1 + 1/(q\xi_l)^2]^{(d_l - 1)/2}} \qquad (46)$$

where $\Gamma(x)$ is the gamma function, and r_o is the gauge of the measurement which has the characteristic size of the scattering units. The first term ($\tilde{1}$) originates from the fact that at a certain q-value the interference between particles is not observed and the scattering is dominated by the pure particle scattering. In practice, a minor re-scaling of this value is necessary to fit to experimental data. Figure 14 shows an example of experimental scattering data obtained from both the cross-linked polymer network, and the corresponding semidilute polymer solution. The solid line in the figure represents a best fit to the product, $P_{\text{blob}} \cdot S_{\text{fractal}}$, of equations (44) and (46). The data at large-q basically overlap, while the low-q data proves additional fluctuations in the cross-linked gel, as well described by the model-function.

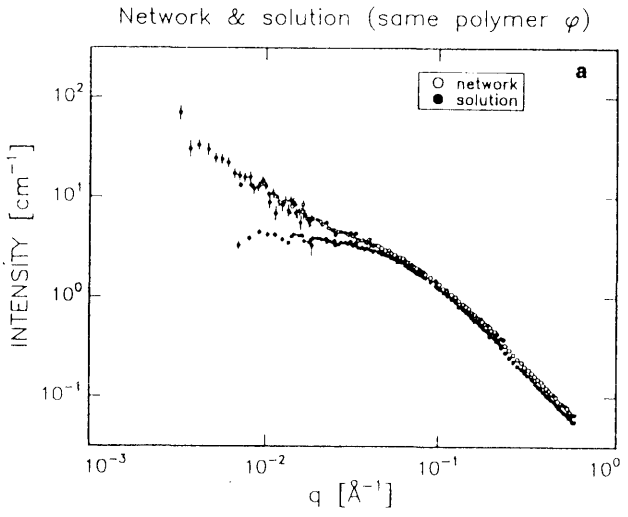

Figure 14 Experimental SANS scattering pattern of a semidilute polymer solution, and the corresponding cross-linked network. The solid line represent the best fit, as described in the text (reproduced from Falcao *et al.*, *Macromolecules*, **1993**; 26: 5350).

7 Polymer Blends

Generally, the thermodynamic properties of polymer blends are described within the Flory-Huggins model that is based on the assumption of negligible small thermal composition fluctuations according to the mean field approach. In reality it is, on the other hand, well approved that thermal composition fluctuations significantly renormalize the thermodynamics: the luctuations are small at temperatures far from the critical value but they become large near the region of the critical point, beyond which phase decomposition occurs. In this region, the Flory-Huggins meanfield model is not valid anymore and one needs thermodynamic models which self-consistently include the effect of thermal composition fluctuations. Furthermore, thermal fluctuations influence the process of phase decomposition as they smear out the spinodal line separating the metastable and the unstable regions.

In the present section we will review the basis for experimental studies of thermal composition fluctuations

in their equilibrium state, as measured using the small angle neutron scattering technique. We will in the presentation start to discuss how to extract information on the phase diagram and interaction parameter based on a meanfield random phase approximation the RPA-theory. Next we will discuss the possibility to use scattering technique to explore the renormalized thermodynamics near the critical point, where thermal composition fluctuations diverges.

The composition fluctuation of the polymer blend is characterized by a single length scale, the correlation length, ξ, which is closely related to the system susceptibility $S(0)$. The correlation length and $S(0)$ follow both scaling behavior with respect to the reduced temperature and with critical exponents that characterise the relevant universality class. The susceptibility and correlation length are described as

$$S(0) = C \cdot \tau^{-\gamma} \tag{47}$$

and

$$\xi = \xi_0 \cdot \tau^{\nu} \tag{48}$$

where $\tau = |T_c - T|/T$ is the reduce temperature, γ and ν the critical exponents characterizing the universality class, and C the critical amplitude. Far from the critical point thermal fluctuations are weak. In this range the fluctuations can be described within the Gaussian approximation and one obtains the mean field scaling laws for correlation length and susceptibility with the critical exponent, $\gamma = 1$ and $\nu = 1/2$. In the near vicinity of T_c, polymer blends belong to the 3d-Ising universality class, where γ is 1.24.

The thermodynamics of polymer blends are accordingly described in the asymptotic limits both near by and far from the critical point by simple scaling laws, but with different critical amplitudes and critical exponents. The cross-over between these two regimes is determined by the Ginzburg criterion [25, 26]. The crossover value is the so-called Ginzburg number, Gi.

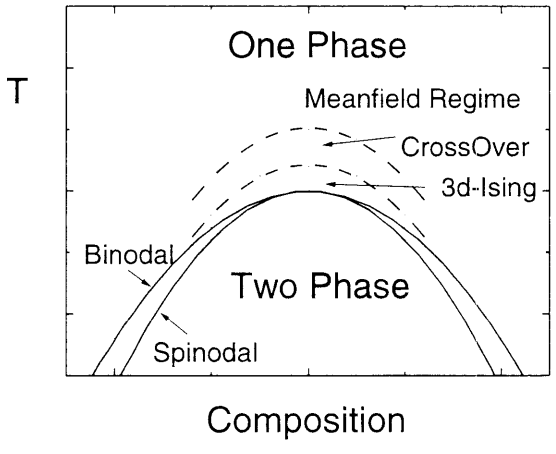

Figure 15 Schematic illustration of the phase behavior of binary polymer blend, showing the mean-field, the cross-over, and the 3D-Ising regimes of critical behavior, and binodal and spinodal phase boundaries.

For polymer blends it was argued that the Ginzburg number should be inversely proportional to the degree of polymerization, N. With the large N values characterizing polymers it was accordingly predicted that polymer blends in practice should show mean-field behavior effectively to the critical point [15]. Experimental scattering experiments have shown, however, unambiguously that the situation is more complex; polymer blends are characterized by Gi-values much larger than expected [27, 28].

7.1 Composition and Density Fluctuations

A binary polymer blend shows in general, in the mixed state, thermal composition fluctuations. These fluctuations can thermodynamically be described by the structure factor $S(q)$, and can accordingly be measured directly in an elastic scattering experiment.

A given polymer sample may, however, have different types of heterogeneities or fluctuations that all give rise to diffraction of the beam and contribute to the structure factor, but the various kinds of fluctuations have in general quite different contrast factors, and thus different amplitude of scattering (see equation (8)).

The fluctuations include beyond the chemical composition fluctuations, density fluctuations, which are independent of the composition fluctuations as discussed in [1]. The susceptibility of thermal density fluctuations is according to the fluctuation-dissipation theorem related to the compressibility $\beta = \partial \ln V/\partial P$, ($V$ being volume and P pressure) as [1]

$$S(0) = RT \cdot \beta \tag{49}$$

The contrast factor of density fluctuations is obtained from the average coherent scattering length density ρ^{-2} of the sample: $\bar{\rho} = \phi\rho_A + (1 - \phi)\rho_B$, ϕ being the volume fraction of the A-component.

The contribution to the measured $S(0)$ is in general negligible small in comparison with the contributions from composition fluctuations. As an example, we may refer to a polymer blend of deuterated polystyrene (d-PS) and poly (vinylmethylether) (PVME). The measured compressibility [29] of $\beta = 5 \cdot 10^{-10}/MPa$ gives an estimated contribution to the $S(0)$-susceptibility of approximately $1.5\,cm^3/mol$ from density fluctuations. In comparison the susceptibility of composition fluctuations, as discussed in further details below (see equation (58)), gives $S(0) = V/4$ near the compensation temperature T_{comp} of vanishing effective interaction parameter: $\chi = 0$. Even a polymer blend of relative small molar volume of for example $V = 2000\,cm^3/mol$, thus gives a contribution to $S(0)$ which is at least two orders of magnitude above the contribution from the density fluctuations to the total $S(0)$.

7.2 Flory-Huggins Theory

The structure factor, $S(q)$, describing the thermal composition fluctuations is measured directly by the neutron scattering function. The extrapolated value of $S(q)$ at the momentum transfer $q = 0$ determines the susceptibility, $S(0)$. The susceptibility, $S(0)$, is related to the second derivative of the Gibbs free energy of mixing, ΔG, with respect to the composition ϕ, by the fluctuation-dissipation theorem according to

$$S^{-1}(0) = \partial^2(\Delta G/RT)/\partial\phi^2 \tag{50}$$

where ΔG is a thermodynamic potential depending on temperature T, pressure P and composition ϕ. If $S(0)$ therefore is determined as a function of these parameters the system can in principle be fully characterized within the thermodynamic context.

Within the meanfield approximation the Gibbs free energy of mixing for binary polymer blends of polymer A and polymer B with composition $\phi_A = \phi$ and $\phi_B = 1 - \phi$ is given as

$$\Delta G/RT = \left[\frac{\phi \ln \phi}{N_A v_A} + \frac{(1-\phi)\ln(1-\phi)}{N_B v_B}\right] + \phi(1-\phi)\chi/T. \tag{51}$$

This equation represents the Flory-Huggins model for binary polymer blends. The model assumes incompressibility ($\phi_A + \phi_B = 1$). The first term describes the usual entropy of mixing, which is inversely proportional to the molar mass, and thus to the square of the polymer radius of gyration R_g (equation 31). The second term in equation (51) describes essential enthalpic contributions to ΔG, represented by the segmental Flory-Huggins interaction parameter, χ:

$$\chi = [\epsilon_{AB} - 1/2 \cdot (\epsilon_{AA} + \epsilon_{BB})] \tag{52}$$

where ϵ_{AB} represents interaction between dissimilar (A and B) segments and ϵ_{AA} and ϵ_{BB} represent interaction between similar segments of A and B type, respectively.

The χ-parameter reflects dipole-dipole interactions as well as other possibly effects, and may be rather complex in origin. According to the original Flory-lattice model, χ is expected to be independent of degree of polymerization, but in reality only high molar mass polymers have effectively a segmental χ-parameter where end-effects are negligible. χ is moreover assumed to be short ranged, given essential as a delta function around the monomer-monomer distance r_{mm}:

$$\chi(r) = \chi\delta(r_{mm}) \tag{53}$$

Experimentally it has been shown, however, that in some cases χ has a finite interaction range far beyond this r_{mm} distance [30].

Both the size and the sign of the Flory-Huggins segmental interaction are critical dependent on the minor differences between various effects, and both negative and positive variation with temperature can be observed. This leads to the respective upper critical (UCST) and lower critical solution temperature (LCST) of the phase diagram. Examples of these two kinds are shown in Figure 16 and Figure 17, giving data of deuterated polystyrene, dPS, mixed with respectively poly (methylstyrene), PMS, and poly(vinylmethylether), PVME.

Experimental use of the Flory-Huggins model, equation (51) shows moreover generally, that the term reflected by the χ-parameter is not purely of enthalic origin, but represents also some entropy. Formally, χ is therefore written as

$$\chi = \chi_h/T - \chi_\sigma \tag{54}$$

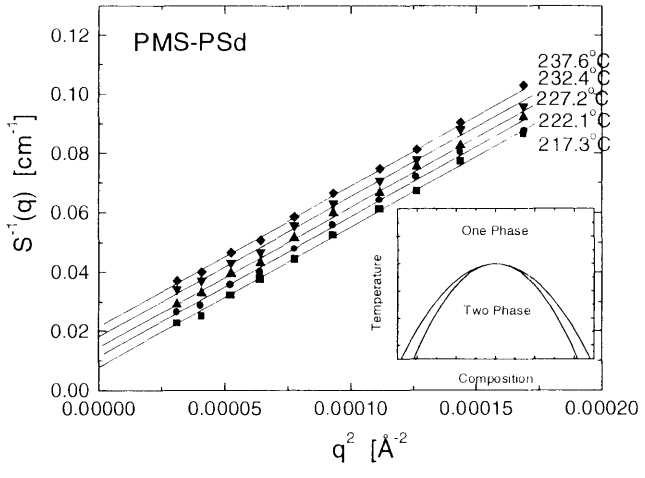

Figure 16 Structure factor of a binary polymer blend, PMS/PSd as obtained at different temperatures. The data are plotted in the Zimm representation: $S^{-1}(q)$ versus q^2. The PMS/PSd blend is an example of a UCST system. (Data originally published in Brerenton *et al., J. Chem. Phys.*, **1987**; 87: 6144).

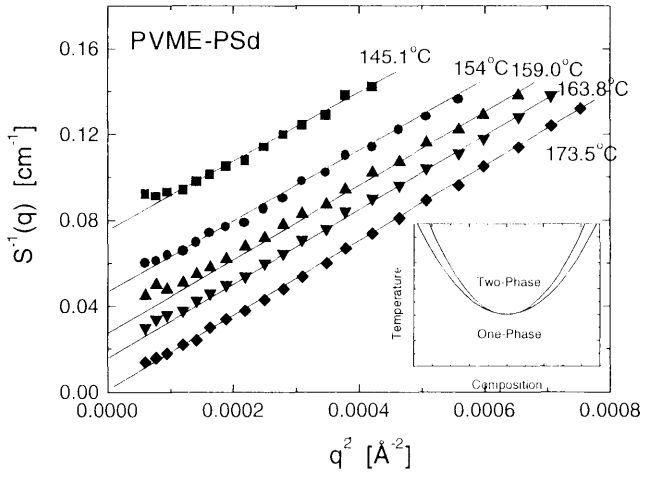

Figure 17 Structure factor of binary polymer blends as obtained at different temperatures. The data are plotted in the Zimm representation: $S^{-1}(q)$ versus q^2. The PVME/PSd blend is an example of a LCST system. (Data originally published in Brerenton *et al., J. Chem. Phys.*, **1987**; 87: 6144).

where the temperature independent values χ_h and χ_σ represents the pure entalpic and entropic parts of the interaction parameter, respectively. Using this form of χ, equation (51) may be rewritten into the form

$$\Delta G/RT = \left[\frac{\phi \ln \phi}{N_A} + \frac{(1-\phi)\ln(1-\phi)}{N_B} - \phi(1-\phi)\chi_\sigma\right] + \phi(1-\phi)\chi_h/T \quad (55)$$

where the first term is now pure entropic and the second is pure enthalpic.

From ΔG in Equation (51) and the fluctuation-dissipation theorem in Equation (50), the susceptibility $S(0)$ is derived as:

$$S(0) = \left[2(\chi_s^{scat} - \chi^{scat})\right]^{-1} \quad (56)$$

with the 'effective' Flory-Huggins parameter χ^{scat} given as [15, 1],

$$\chi^{scat} = -\frac{1}{2}\frac{\partial^2}{\partial\phi^2}\left[\phi(1-\phi)\chi\right]. \quad (57)$$

Formally χ^{scat} can be written as a sum of the entropic and the enthalpic parts: $\chi^{scat} = \chi_h^{scat}/T - \chi_\sigma^{scat}$ in analogy with the Flory-Huggins parameter, χ, itself (equation 54). In the scattering experiment the relevant parameter is accordingly χ^{scat} rather than χ, and one must therefore be careful when comparing the interaction values as obtained from scattering data with the parameter obtained from other techniques. Only if χ is independent of composition, $\chi(\phi) = \chi$, is $\chi^{scat} \equiv \chi$. This is, however, not generally the case. There may in particular be deviations near the limits $\phi \sim 0$ and $\phi \sim 1$, probably as a consequence of density fluctuations which might not be negligible in relation to composition fluctuations in these limits. Since the present discussion only concerns the Flory-Huggins parameters as related to the scattering experiment, however, there should be no doubt which parameter is discussed. We will in the following for simplicity therefore replace the symbol for the effective scattering parameter with the bare χ, giving equation (56) the form

$$S(0) = \left[2(\chi_s - \chi)\right]^{-1} \quad (58)$$

The value χ_s is the Flory-Huggins parameter at the spinodal, or for critical compositions, $\phi = \phi_c$: the critical point χ_c. It is derived from the entropy of mixing according to,

$$\chi_s = \frac{1}{2}\left(\frac{1}{\phi N_A} + \frac{1}{(1-\phi)N_B}\right) \quad (59)$$

For a symmetrical blend of A and B polymers with equal molar mass (and volume): $N = N_A = N_B$ the critical composition is $\phi_c = 0.5$ and the critical Flory-Huggins parameter becomes according to equation (59),

$$\chi_c = 2/N. \quad (60)$$

The meanfield critical amplitude, equation (47) is related to the Flory-Huggins parameters according to [33, 34]

$$C_{MF} = \frac{1}{2}|\chi_s - \chi_\sigma| = T_c^{MF}/2\chi_h \quad (61)$$

where the last equality relates to the 'meanfield' critical temperature T_c^{MF}.

7.3 Ornstein-Zernike Approximation of the Structure Factor, $S(q)$

The structure factor $S(q)$ for polymer blends is within the random phase approximation, RPA, given in terms of the form factors S_A and S_B of the single coils of components A and B, respectively, and the Flory-Huggins interaction parameter $\chi(q)$ according to

$$S^{-1}(q) = S_A^{-1}(q) + S_B^{-1}(q) - 2\chi(q) \quad (62)$$

where the single coil formfactor has the form

$$S_{A,B}(q) = \phi N_{A,B} \cdot g_D(R_{A,B}^2 q^2), \quad (63)$$

$g_D(x)$ representing the Debye function (see section 8.5). Insetting the expression of $g_D(x)$, equation (38), into equation (63) yields to second order in q:

$$S^{-1}(q) = \left[\frac{1}{\phi N_A} + \frac{1}{(1-\phi)N_B} - 2\chi\right] + \left[\frac{1}{3}R_A^2\frac{1}{\phi V_A} + \frac{1}{3}R_B^2\frac{1}{(1-\phi)V_B}\right]\cdot q^2 = S^{-1}(0) + \ell^2 q^2 \quad (64)$$

assuming a q-independent χ-factor. This is the Zimm-approximation.

Figure 16 and Figure 17 show examples of the structure factor given in Zimm-representation, S^{-1} versus q^2. The data represents measurements of blends of deuterated polystyrene, d-PS, mixed with respectively poly (methyl styrene), PMS, and poly(vinylmethylether), PVME, and measured for different temperatures approaching the spinodal T_s. The plots show linear behavior in agreement with the Zimm-approximation. It appear from the data that while the inverse susceptibility $S^{-1}(0)$ of the PSd/PMS polymer blend approach zero upon lowering the temperature, $S^{-1}(0)$ of the PSd/PVME blend approach zero for rising T, reflecting respectively the *LCST* and *UCST* behavior, as mentioned above.

The Zimm-representation of the scattering functions shown in Figure 16 and Figure 17 is characterized by regular parallel sets of data with same slope ℓ^2, as expected according to the Flory-Huggins lattice model.

The q-dependence of $S(q)$, the slope ℓ^2, is determined by local structures, i.e., the flexibility of the chain, and possibly the range of interaction. Insetting the expression

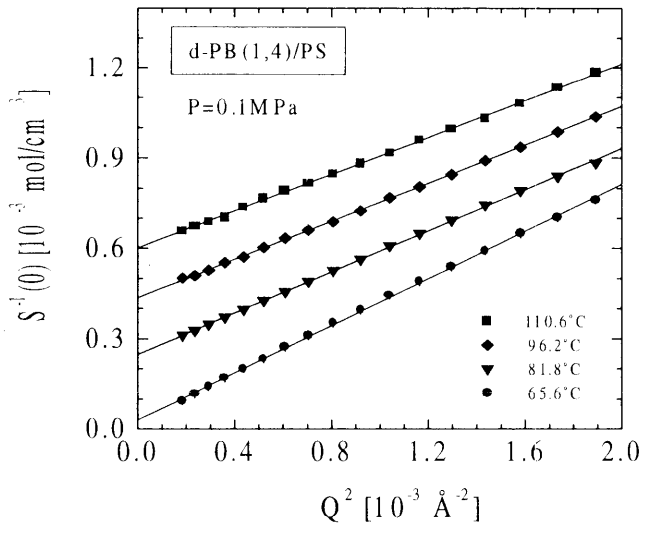

Figure 18 Structure factor of binary polymer blend if PS and dPB as obtained at different temperatures. The data are plotted in the Zimm representation: $S^{-1}(q)$ versus q^2, and represents an example of a system where the effective interaction $\chi(r)$ goes beyond the monomer-monomer distance (reproduced from Frielinghaus *et al., J. Appl. Cryst.*, **1997**; 30: 696; Schwahn and Mortensen, in *Scattering in Polymeric and Colloidal Systems* (2000).

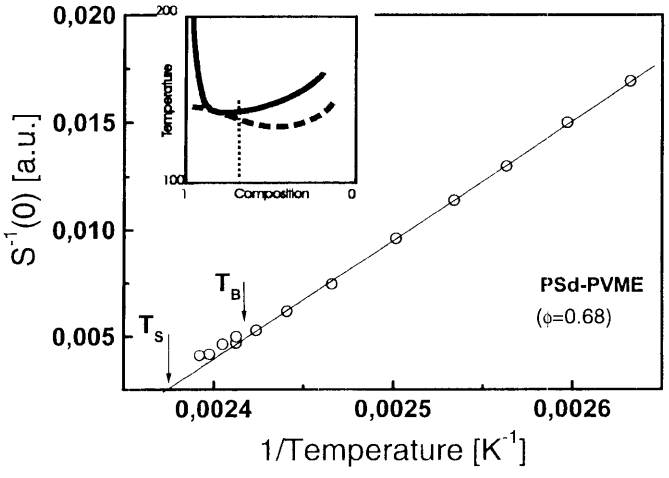

Figure 19 Susceptibility $S(0)$ plotted as a function of temperature, $S^{-1}(0)$ vs. T. The data are of a binary polymer blend of PSd and PVME. The data shows linear (meanfield) behavior over large ranges. The extrapolated $S^{-1}(0) = 0$ point reflects the spinodal, while the break in the curve reflects the binodal.

$R_g = Na^2/6$ for the radius of gyration (equation 31) into equation (64) shows that the value of ℓ is of the order of a third segment length of the polymer chain. The correlation length of the thermal composition fluctuation, ξ, is given as the square of the product of ℓ^2 and $S(q)$,

$$\xi = \ell \cdot \sqrt{S(0)}, \tag{65}$$

which with $S(0) \sim \tau^{-1}$ fulfills the meanfield scaling law, $\xi \propto \tau^{0.5}$.

Other polymer blends does not have the regular behavior expressed in Figures 16 and 17, but have a slope that is varying with temperature. Examples are polystyrene mixed with poly (tetramethyl-carbonate) PS/PTMC [30] and mixed with poly (butadiene) PS/PB [42, 31]. The latter example is reproduced in Figure 18.

Changes in the slope of S^{-1} versus q^2, and corresponding variation in pre-factor ℓ^2, are attributed to a final range of effective interaction rather than the δ-function equation (63) [30]. In the small q-limit, the Flory-Huggins parameter χ can then be approached

$$\chi(q) = \chi \exp(-r_0^2 q^2) \tag{66}$$

reflecting the range of interaction, r_0. In the Zimm-approximation, Equation (64), this leads, to first order in r_0, to the prefactor

$$\ell^2 = \frac{1}{3}\left(\frac{R_{g,A}^2}{\phi N_{A,w}} + \left(\frac{R_{g,B}^2}{(1-\phi)N_{B,w}} + r_0^2\chi\right)\right) \tag{67}$$

From scattering experiments it is accordingly possibly to measure the effective range of interaction in polymer blends.

7.4 Spinodal and Binodal Phase Boundaries Measured by SANS

In Figure 19 the inverse susceptibility of a dPS/PVME polymer blend has been plotted versus the inverse temperature. The composition is off critical, $\phi \neq \phi_c$. The data shows linear $S^{-1}(0)$ versus T relationship over large ranges, proving good agreement with mean field characteristics. The data are in this temperature range stable and reproducible, and extrapolating the data to $S^{-1}(0) = 0$ gives the (mean field) value of the spinodal: T_s (T_s^{MF}). At a given temperature, $T = T_B$, marked deviation appears signifying crossing the binodal (coexisting) curve of the phase diagram, as sketched in the insert of the figure. In the regime between T_B and T_s the obtained data will usually show fluctuations in time due to the macroscopic phase changes.

From data like those expressed in Figure 19 thermodynamic parameters can be extracted: namely the binodal and the spinodal phase boundaries, and the Flory-Huggins interaction parameter. The critical point (T_c, ϕ_c) is obtained from the sets of data where the temperature of the spinodal and the binodal merge.

Figure 20 shows the thermodynamic results from SANS experiments performed on an isotope mixture of polystyrene and deuterated polystyrene, PS/dPS, both polymers of very well defined molar masses. This gives a near ideal phase diagram characterized as a UCST system [32, 31]. The figure shows both the phase diagram and the Flory-Huggins parameter, χ as obtained

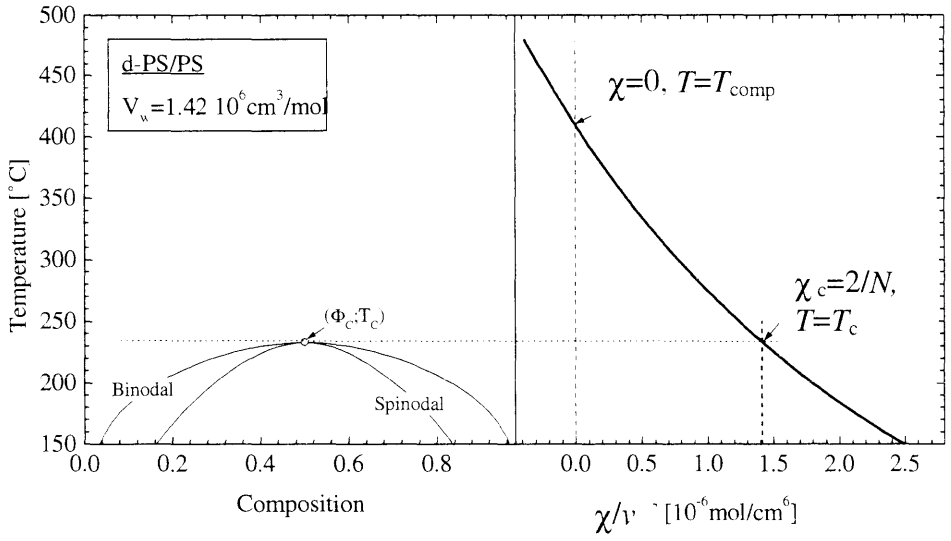

Figure 20 Phase diagram of the polymer only deviating with isotope change: dPS/PS. This system is a near ideal polymer blend with UCST. (reproduced from Müller *et al., J. Chem. Phys.*, **1996**; 104: 5326).

from the experimental scattering data. According to the Gibbs conditions of stability, equation (50), the inverse susceptibility $S^{-1}(0)$ is positive for a homogeneously mixed blend and becomes zero at the critical point. According to equation (58) this means that the χ-parameter in the homogeneous phase is smaller than χ_s at the spinodal, or smaller than χ_c at the critical temperature in the case of critical composition. A homogeneous blend with $\chi > \chi_s$ is in an unstable phase, and will spontaneously decomposes through spinodal decomposition. The binodal and the spinodal can be calculated from the Gibbs free energy equation (51) applying the tangent method using respectively the first derivative and the zero value of the second derivative of ΔG with respect to the composition ϕ.

7.4.1 Effect on Polydispersity in Phase Behavior

Figure 21 shows the phase diagram of a dPS/PVME-blend as obtained from scattering experiments [36]. The blend is characterized with relative monodisperse dPS ($M_w = 232$ kD, $M_w/M_n = 1.08$), but PVME component is markedly polydisperse ($M_w = 89$ kD, $M_w/M_n = 2.5$).

The experimental phase diagram deviates in a variety of manner from the more ideal phase behavior of PS/dPS, Figure 20 and the schematically figures given in Figure 15. One characteristic of the d-PS/PVME-diagram is that the critical point is not at symmetric composition. This signifies asymmetry between molecular parameters of dPS and PVME, which among others can be related to asymmetry between the specific molar volume of the two polymers.

Another characteristic appearance is that the critical temperature does not represent the lowest temperature of the binodal phase boundary. This is a result of major polydispersity of the PVME-polymer system. The spinodal phase boundary is related to the w-averaged mass, $M_w = \sum n_i M_i^2 / \sum n_i M_i$ as given in equation (34) in section 8.5. The situation for the binodal appear to have more complex origin, as obvious from the results given in Figure 21.

The phase diagram of a blend including a component of significant polydispersity, as that in the dPS/PVME system, should more correctly be represented in a multi-dimensional phase diagram, one axis for the mono-

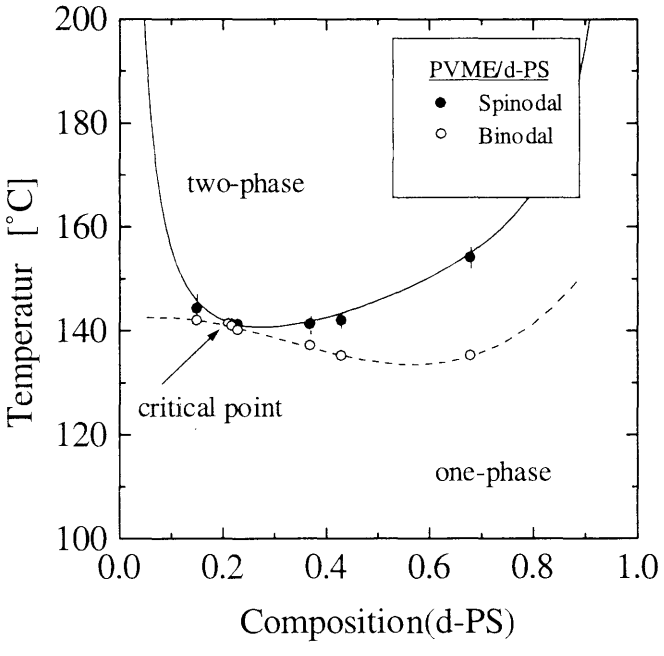

Figure 21 Phase diagram, including spinodal and binodal, of dPS-PVME as obtained from small-angle neutron scattering experiments (Schwahn *et al., J. Chem. Phys.*, **1987**; 87: 6078).

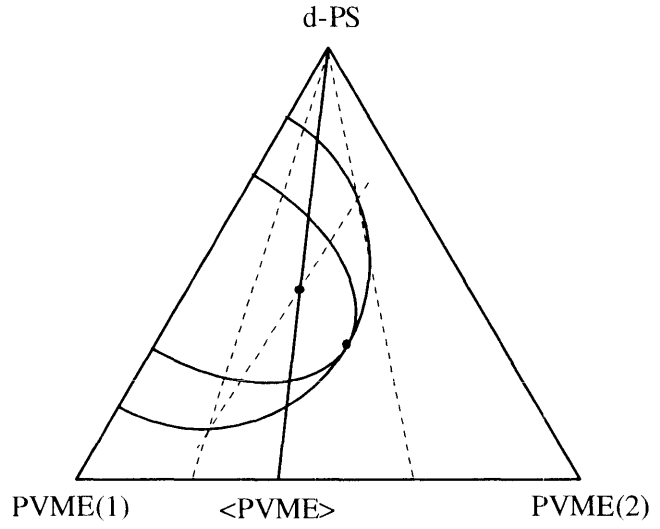

Figure 22 Schematic phase diagram of a three component system (od dPS, PVME (1) and PVME (2), where the two PVME systems differ in molar mass). The diagram represents a given temperature. The line d-PS-< PVME > represents the experimental composition axis of an 'experimental binary' blend as that shown in Figure 21 (Schwahn and Mortensen 2000).

disperse d-PS and depending on the size distribution a suitable multiply of axes for the PVME component. As an example a three component mixture has been plotted for a constant temperature; one dimension for the d-PS and the other two for two PVME components different in molecular volume. The line between the d-PS and the average < PVME > as depicted represents the composition axis in the quasi binary phase diagram as in Figure 15. While the PVME (1) component is only partially miscible with d-PS because of its larger molar mass the PVME (2) component is complete miscible at this temperature. So, the average < PVME > is only partial miscible as the 'composition' line passes the metastable two-phase region. If the composition of the sample is within the two-phase regime, the system decomposes into phases with PVME components of different average molecular weight. The observation, Figure 21, that the metastable phase region of the d-PS/PVME system is crossed at a lower temperature than the spinodal and the critical can be explained by the three-component phase diagram schetched in (Figure 22).

7.5 Critical Scattering in the Vicinity of T_c

In the near vicinity of the critical point T_c, mean field characteristics are no longer valid. The thermal composition fluctuations tend to stabilize the 'disordered' phase thus giving rise to a renormalized critical temperature. The relation between the mean-field value T_c^{MF} and the real T_c is expressed by the Ginzburg relation [26]:

$$T_c^{MF} = T_c/(1 - Gi), \tag{68}$$

where Gi is the Ginzburg number.

In a plot showing the susceptibility $S^{-1}(0)$ versus τ^{-1} for critical composition $\phi = \phi_c$, analogous to that of Figure 19, one then will find deviation from linear relationship. As an example shows Figure 23 such a behavior in the polymer blend of polystyrene and polybutadiene, dPB/PS [42, 31]. Polymer blends shows scaling laws in agreement with the 3d-Ising model as T approach T_c, [27, 28], i.e.,

$$S(0) = C_+ \tau^{-\gamma} \text{ with } \gamma = 1.24 \tag{69}$$

and

$$\xi = \xi_+ \tau^{-\nu} \text{ with } \nu = 0.63 \tag{70}$$

Generally, the experimentally determined susceptibility $S(0)$ can effectively be analyzed applying a function that describes $S(0)$ within the whole one-phase regime. Based on an ϵ-expansion model, Belyakov and Kiselev found such a function which practically have been proved to describe the experimental data very well [37, 38]. The crossover function has the form

$$\tilde{\tau} = \left(1 + 2.333\tilde{S}(0)^{\Delta/\gamma}\right)^{(\gamma-1)/\Delta} \times \left[\tilde{S}^{-1}(0) + \left(1 + 2.333\tilde{S}(0)^{-\Delta/\gamma}\right)^{-\gamma/\Delta}\right], \tag{71}$$

The exponents $\gamma \simeq 1.24$ and $\Delta = 0.5$ are the critical exponents of the 3d-Ising model. The rescaled reduced

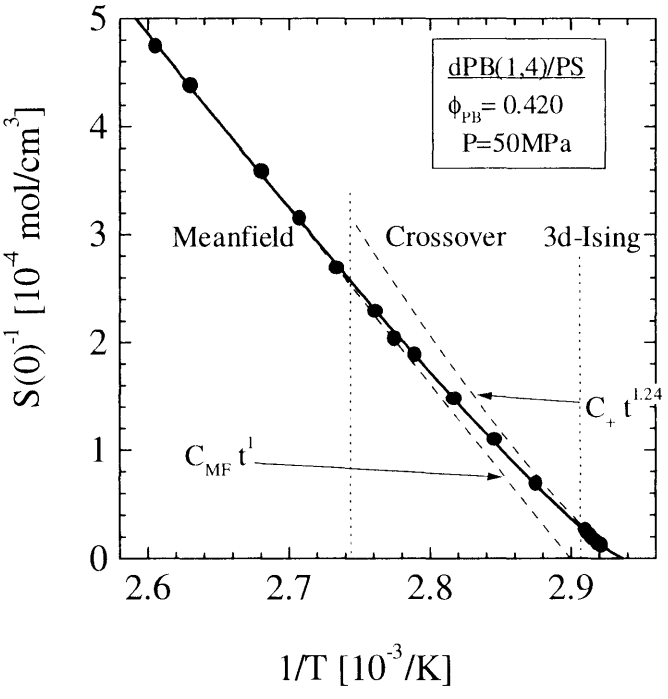

Figure 23 Inverse susceptibility $S^{-1}(0)$ versus inverse temperature for a mixture of dPB and PB of near critical composition. The solid line represents the best fit using the crossover function equation (71) while the dotted lines shows the asymptotic meanfield and 3d-Ising laws, respectively (Frielinghaus *et al.*, *J. Appl. Cryst.*, **1997**; 30: 696; Schwahn and Mortensen, 2000).

temperature $\tilde{\tau} = \tau/Gi$ is formulated as a function of the rescaled susceptibility $\tilde{S}(0) = S(0)/C_{MF}Gi$.

The parameters Gi, C_{MF}, and T_c deliver the thermodynamic information which can be obtained from a fit of the experimental $S(0)$ versus T using the crossover function given in equation (71). In the asymptotic limits of $\tau \gg 1$ and $\tau \ll 1$, respectively, the susceptibility in equation (71) follows the well-known scaling laws equation (47, 70) with amplitude C_{MF} and C_+ in respectively the meanfield and the 3d-Ising ranges [15, 26].

The Ginzburg parameter, Gi itself is related to the ratio of the critical amplitudes of the 3d-Ising and the meanfield case according to [37, 39]

$$Gi = 0.069 \cdot (C_+/C_{MF})^{1/(\gamma-1)} \tag{72}$$

As a result of the large exponent $(\gamma - 1)^{-1} = 4.17$, it appears that Gi is very sensitive to the critical amplitudes.

Figure 23 shows the inverse susceptibility $S^{-1}(0)$ versus inverse temperature for a mixture of dPB and PS of near critical composition [42, 31]. The solid line represents a fit of the crossover function given in equation (71); it describes the experimental data very well over the whole measured homogeneous phase including the two asymptotic regions, meanfield and 3d-Ising, where scaling relations of the susceptibility are valid. This experimental example indicates clearly that the validity of the meanfield Flory-Huggins model for binary polymer blends is somewhat limited. The relevant temperature regime of most miscible polymer blends are actually in the crossover range rather than in the meanfield, as originally anticipated.

The fit of the crossover function to the experimental data uniquely gives the Ginzburg number Gi and the critical amplitude of the meanfield approximation, C_{MF}.

7.6 Ginzburg Number

The critical amplitudes described in Equation (61) and by the scaling law $C_+ \propto N^{2-\gamma}$ leads, according to Binder to [34, 33]

$$Gi = \left[N^{2-\gamma}(2/N + \chi_\sigma)\right]^{1/(1-\gamma)} \tag{73}$$

In the limit of $\chi_\sigma = 0$, i.e., in the limit that the Flory-Huggins term is purely enthalpic, this relationship becomes identical to the scaling law $Gi \propto N^{-1}$ originally derived by deGennes [40] for incompressible systems. The degree of thermal fluctuations as expressed by the Ginzburg number Gi depends accordingly on the entropic term χ_σ of the χ-parameter, which could therefore significantly enhance Gi because of the large $(\gamma - 1)^{-1}$-exponent of equation (72) and equation (73).

In Figure 24 the Ginzburg number from several polymer blends has been plotted versus the mean degree of polymerisation in a double logarithmic scale. The straight line indicates an estimation of the proposed

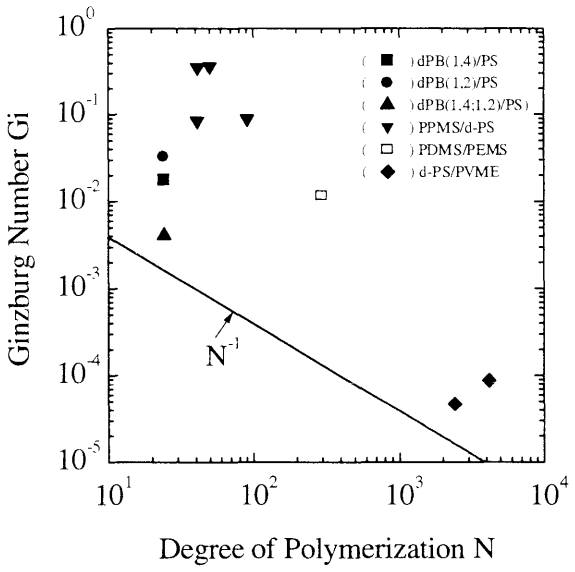

Figure 24 Ginzburg number Gi versus degree of polymerization N for different polymer blends (reference Schwahn *et al.*, *J. Phys. II*, **1994**; 4: 837 and Schwahn and Mortensen (2000)).

values according to a universal scaling behavior of $Gi \propto N^{-1}$, and approaching the known Gi-value of low molar mass liquids.

The experimental data show that the Ginzburg number in polymer blends is not simply N times smaller than the value in low molar mass liquids, whose Gi is of the order of $10^{-2} - 10^{-2}$. For polymer blends with N in the range up to 100, a Gi-value of the order of 10^{-1} is observed. This means that polymer blends may have a significantly larger critical range than small molar mass systems. The statement that polymer blends in principle are meanfield systems is therefore not correct.

The maximum values of Gi are found for polymers with N-values between 40 and 50. The exact value of these very large Gi-numbers might however be somewhat uncertain due to the limited T-range available. To get a reasonable significance of Gi the thermal fluctuations has to be measured in a temperature interval of more than $\Delta T \simeq Gi \cdot T_c$ above T_c in order to get a sufficiently large deviation from the pure 3d-Ising scaling behavior. The observed discrepancy between theoretical expectations and experiments can be explained by including the entropic term of the Flory-Huggins parameter, χ_σ, and the large exponent of 4.17 in equation (72) and equation (73). The large exponent makes Gi very sensitive to small changes of the critical amplitudes of the susceptibility, and therefore Gi is actually not a universal number whose value is solely determined by the degree of polymerization.

Only for polymer blends with N larger than approximately 1000 the Ginzburg number becomes efficient small, $Gi = 10^{-4}$, to give effectively meanfield character

even very close to the critical point. It should be mentioned, though, that miscible polymer blends of such large molecular weight exists only under special circumstances. Examples of such meanfield systems are polymers with extremely small Flory-Huggins interaction parameter. That can be realized in isotopic mixtures, as the blend of d-PS and PS shown above. Other examples are polymers that have a lower critical solution temperature, LCST, i.e., they are miscible at low temperatures and decompose at high temperatures. The blend d-PS/PVME shown in Figure 21 represents such an example, Under more realistic conditions polymer blends with a two-phase regime below 200 °C are found only for N of the order of 100. For such N-values the results given in Figure 24 clearly demonstrate that Gi is equal to, or even larger than that of low molar mass liquids.

7.7 The Correlation Length and Critical Exponents

In the asymptotic range of the 3d-Ising model a scaling relation between the slope ℓ^2 of the Zimm-expression equation (64), and the correlation length ξ exists. From simple calculations based on the 3d-Ising scaling laws, one find

$$\ell^2 = A_+ \xi^{\eta} \qquad (74)$$

where A_+ is an amplitude and η is the 'Fisher' critical exponent. η is related to the critical exponents γ and ν of respectively susceptibility and correlation length:

$$\eta = 2 - \gamma/\nu.$$

In Figure 25 the slope ℓ^2 has been plotted versus the correlation length in a double logarithmic scale for the dPB/PS blend [41, 42]. Above a correlation length of 100 Å the slope of 0.044 is within experimental accuracy in agreement with the theoretical value of $\eta = 0.038$.

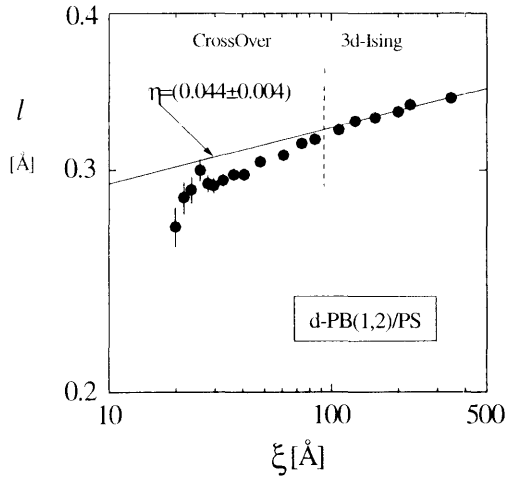

Figure 25 The slope ℓ^2 of the Zimm-approximation for $S(q)$ plotted versus the correlation length ξ in the crossover and 3d-Ising regime. The slope of the 3d-Ising regime provide the Fisher exponent η (Janssen *et al., Phys. Rev. Lett.*, **1992**; 68: 180).

7.8 Critical Fluctuations Studied in the Decomposed Sample

In the two-phase regime of polymer blends, it is also sometime possibly to measure critical fluctuations. This is for example the case in a blend of PPMS and d-PS, where the scattering from thermal fluctuations is well separated from that of the domain shape which occurs at q less than about 10^{-3} Å^{-1} because of their μm large sizes. Below T_c, $S(0)$ represents the thermal fluctuation modes within the precipitated domains.

Figure 26 shows the susceptibility $S(0)$ of the polymer blend d-PS/PPMS, as measured both above and below the critical temperature. Below T_c the susceptibility represents an average of susceptibilities in the two domains rich in respectively the one and the other polymer component. In both cases the susceptibility follows the scaling law of the 3d-Ising universality class. The ratio of the two critical amplitudes C_+ and C_- obtained respectively above and below T_c is slightly smaller than the number predicted from scaling theory [43].

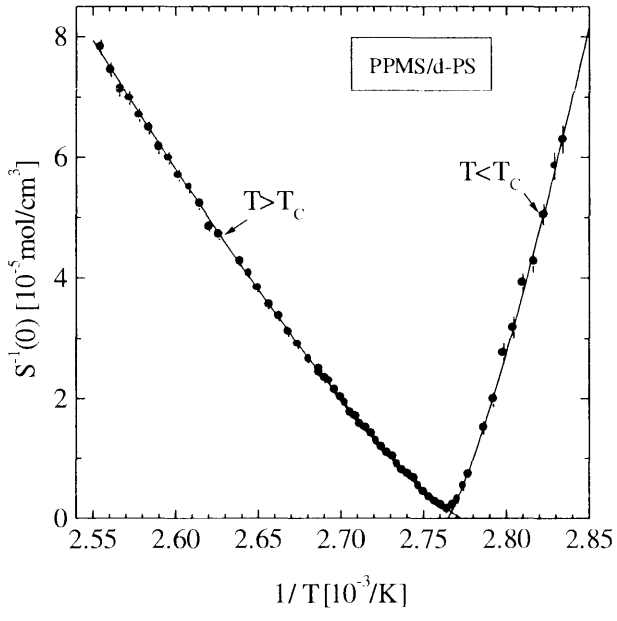

Figure 26 Inverse susceptibility above and below T_c which both follows the scaling behavior of the 3d-Ising model. The measured composition fluctuations below T_c are fluctuations within macroscopic segregated domains (reference Schwahn *et al., Phys. Rev. Lett.*, **1994**; 73: 1452).

7.9 External Fields

So far thermal fluctuations have been discussed in relation to temperature. Other thermodynamic/hydrodynamic parameters might be of interests both from fundamental and applied veiwpoints. Below, we will briefly discuss the behavior of thermal composition fluctuations when varying external fields like pressure and shear are applied.

7.9.1 Pressure

According to the equation of states theories the entropic term of the Flory-Huggins parameter χ_σ in equation (61) and equation (62) is related to the compressibility of free volume of the blend. Therefore the absolute value of χ_σ should decrease by applying pressure, and thereby a shift of the phase boundaries to higher temperatures should occur.

Figure 27 shows the inverse susceptibility plotted versus the inverse temperature for various pressures in the range 0.1 and 150 MP. The data are fitted using the cross-over function of equation (71) as shown by the solid lines. The spinodal and binodal temperatures obtained from $S(0)$ increases both with pressure as expected, and qualitatively consistent with the Clausius-Clapeyron equation.

$$\Delta T_B/\Delta P = \Delta V/\Delta S = \left[\partial\chi_h/\partial P - T_B\partial\chi_\sigma/\partial P\right]/(\chi_h/T_B) \tag{75}$$

which predicts a decrease of the sample volume and of the entropy $\Delta S < 0$ upon increasing pressure.

Fits to the experimental data of the d-PB/PS blends provides the Ginzburg number, which shows a decrease with pressure in agreement with theoretical predictions [33, 44, 45].

7.9.2 Shear

In the miscible phase of a high molar mass polymer blend, the application of shear leads to a distortion of the thermal composition fluctuations along the direction of flow, while those perpendicular to the flow remains having their thermodynamic equilibrium behavior [46]. This is consistent with mean-field behavior.

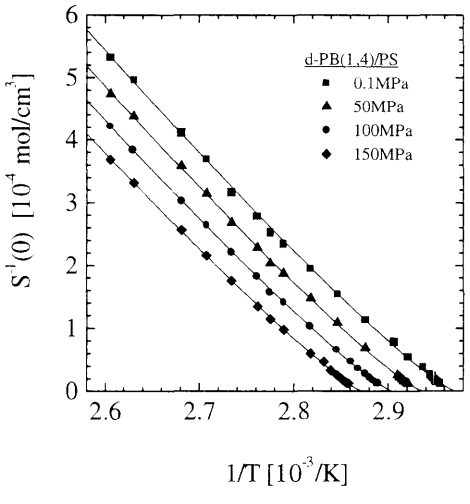

Figure 27 Inverse susceptibility versus inverse temperature of dPB/PS as measured for for different pressures in the range 0.1–150 Mpa. The solid lines are fits to the crossover function equation (71). It appear from the data that pressure increases the critical temperature (Frielinghaus *et al.*, *J.Appl.Cryst.*, **1997**; 30: 696).

The details on the anisotropic response suggest that hydrodynamics or mode-coupling effects are significant. The shear response to the critical temperature is by the mode-coupling renormalization group theory predicted to have the form [47, 48]

$$\Delta T_c(\dot\gamma)/\Delta Y_c(0) = \alpha\cdot(\dot\gamma)^{1/3\nu} \tag{76}$$

where $\dot\gamma = d\gamma/dt$ is the shear flow, γ being the shear amplitude, $\Delta T_c(\dot\gamma) = T_c(\dot\gamma) - T_c(0)$ is the change in critical temperature, and α is a pre-factor given by the spatial dimension and a time characteristic for the relaxation of concentration fluctuations, i.e., depending on the sample viscosity. The exponent ν is the Ising exponent of 0.63, giving a close to $\Delta T_c(\dot\gamma) \sim \dot\gamma^{0.5}$ relationship. Although the equation is derived in the strong shear limit, it reduces to the correct equilibrium for $\dot\gamma = 0$. Both simple liquids [49], and polymer blends [50] have shown very good agreement with this 0.5-power-law dependence of $\dot\gamma$. The prefactors of these diverse systems shows significant differences reflecting the different viscosities in low molar mass liquids and polymer materials.

Upon increasing shear flow, the immiscible sample will reach a critical shear value $\dot\gamma_c$ beyond which the sample is homogenized. According to mean-field theory, one has, including the $\dot\gamma$ dependencies of $S(0)$ and ξ

$$S(0,\dot\gamma)^{-1} \sim T - T_c(\dot\gamma) \tag{77}$$

and

$$\xi(\gamma)^{-2} = T - T_c(\dot\gamma) \tag{78}$$

With the $\Delta T_c(\dot\gamma) \sim \dot\gamma^{0.5}$-relation discussed above, one should therefore find that the correlation length scales with shear flow as

$$\xi(\dot\gamma) \sim \left[1 - T_c(\dot\gamma)/T\right]^{2\nu} = \left[1 + \alpha\cdot\dot\gamma^{1/3\nu}\right]^{-\nu} \tag{79}$$

and

$$S(0,\dot\gamma) \sim \left[1 - T_c(\dot\gamma)/T\right]^{2\nu} = \left[1 + \alpha\cdot\dot\gamma^{1/3\nu}\right]^{2\nu} \tag{80}$$

Experiments have shown very good agreement with these predictions, including both the high and low shear rate limits. In a high molar mass system of polystyrene (PS) polybutadiene (PB), Takebe *et al.* [50] found the high shear rate relations $\xi^{-2} \sim \dot\gamma$ and $S(0) \sim \dot\gamma$, whereas Hobbie *et al.* [51, 52] in a pseudo-binary PS/PB mixture, where the Ginzburg number has been effectively enhanced by the introduction of a low molar mass dioctyl phthalate (DOP), found very good agreement with the Onuki-Kawasaki theory also in the crossover regime between the low and the high shear rate limits. The data analysis by Hobbie *et al.* strongly indicates, that Fisher-renormalisation is relevant for such polymer blends [52].

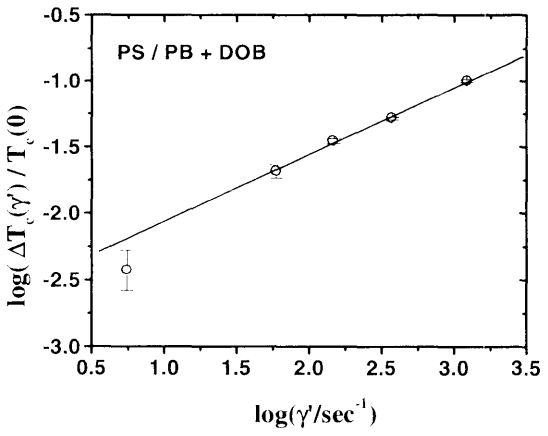

Figure 28 Shear experiment on polymer blend, showing the drop of critical temperature as a function of shear rate (reproduced from Takebe *et al.*, *J. Chem. Phys.*, **1989**; 91: 4369).

8 Block Copolymers

The most simple multi-component polymer system is the binary mixture of two linear polymer chains, A and B, discussed above. Diblock copolymers composed of two linear polymer blocks linked covalently together are closely related in the sense that they also are made up of two linear polymer blocks, but in opposition to blends, the bond between A and B prevents macroscopic phase separation. In Figure 1 are shown schematically such diblock copolymers.

The phenomenological theory of block copolymers is quite analogous to that of polymer blends, discussed in section 7. The thermodynamic properties are also here determined as an interplay between configurational entropy and enthalpic contributions according to the Flory-Huggins model of the Gibbs free energy, equation (71) (see e.g., de Gennes, [15]). For diblock copolymers this is usually written as:

$$\frac{\Delta G}{kT} = \frac{f_A}{N_A}\ln(f_A) + \frac{f_B}{N_B}\ln(f_B) + \chi f_A f_B \qquad (81)$$

where f_A and f_B represent the volume fraction of respective A-type and B-type of monomers. In the incompressible binary system $f_A + f_B = 1$. N_A and N_B are the corresponding degree of polymerization's. The enthalpic contribution is described through the segmental Flory-Huggins interaction parameter χ analogous to the blend system, equation (52) $\chi = [\epsilon_{AB} - 1/2 \cdot (\epsilon_{AA} + \epsilon_{BB})]$ with ϵ_{AA} and ϵ_{BB} representing the interaction energy between similar monomers and ϵ_{AB} is the interaction energy between the two different types of monomers.

As in polymer blends, the effective χ-parameter has also an entropic contribution, and is written in the form of equation (54): $\chi = \chi_h/T - \chi_\sigma$, where χ_σ determines the entropic and χ_h the enthalpic term. The origin of the entropic part is partly due to effects of the free volume, as discussed in connection to polymer blends.

In the presentation above on polymer blends, section 7, it was shown how scattering experiments can be used to measure the composition fluctuations in the homogeneous, miscible phase, and thereby reveal thermodynamic parameters like the binodal and spinodal phase boundaries, value of the interaction parameter χ and the scale of characteristic lengths of interactions.

Polymer blends will for a given positive χ value phase separate on the macroscopic length scale. In the $S(q)$ function this is reflected in the fact that the thermodynamics to a large extend is given by the structure factor measured at zero momentum transfer: $S(q = 0)$.

Block copolymers are composed of polymer blocks, which are linked together by covalent bonds. A block copolymer melt is therefore thermodynamically a singly phase system that cannot phase separate on the macroscopic level, inappropriate of the size of the Flory-Huggins interaction-parameter. On the mesoscopic length-scale determined by the molecular radius of gyration, however, phase separation can occur. For relative miscible blocks (small χ-values) the system will show composition fluctuations on the length scale of the polymer chain, whereas immiscible blocks assembly into a mesoscopically ordered structure. The transition from fully disordered melt to such locally unmixed state is therefore described by the two synonyms *'micro-phase separation transition'* (MST), and *'order-disorder transition'* (ODT) describing the same physical transition, but with emphasis of different physical properties. Depending on the relative volume fraction, f, of the one component and the overall polymer size, N, a variety of mesoscopically ordered structures may be formed. Recent reviews on the copolymer phase behavior includes papers by Bates, Fredrickson and coworkers and by Binder [53, 54, 33, 55].

In the discussion on block copolymers below, we will restrict the presentation to simple di-block architecture where blocks of

$$N_A = f_A \cdot N = f \cdot N$$

A-monomers are covalently bonded to blocks of

$$N_B = f_B \cdot N = (1 - f)N$$

B-monomers, N being the total degree of polymerisation and the composition, $f = f_A$ determining the volume fraction of A-units.

8.1 Disordered Block Copolymers Melts

There have been several theoretical works with the aim to provide the basic description of microphase separation in block copolymer melts. Meier *et al.* presented an early study based on diffusion equation, where entropic contribution from volume constrains, elasticity

differences, interface placement, and enthalpic contribution from heat of mixing were included [56, 57]. Helfand studied the problem of microphase separation in block copolymers with a statistical theory, in which the chain distribution function plays the central importance [58, 59]. In a mean field treatment based on a narrow interface approximation, this theory gives quite good agreement with experimental observations.

The more recent theoretical as well as experimental discussions of the block copolymer phase behavior are basically all based on the mean-field treatment of block copolymer melts presented by Leibler in 1980 [60]. These studies are based upon a single, standard Gaussian model where each molecule of the melt is composed of the N segments of which f is of type A, and the rest of type B. Each block represents a sufficient length of polymer such that they can be treated as Gaussian chains [60–62]. Leibler's theory is based on the random phase approximation, RPA, originally introduced into the polymer physics by deGennes [63]. More elaborated theories, including fluctuation renormalizations [61] and conformational asymmetry [55, 64] are based on this RPA theory. The basic point in these theories is the density-density correlation function

$$\hat{S}(\bar{r}-\bar{r}') \sim \langle \delta_A(\bar{r})\delta_A(\bar{r}')\rangle \tag{82}$$

of which the Fourier transform, $S(\bar{q})$, can be measured directly by elastic scattering experiments such as x-ray or neutrons. In the following, we will give some details on the RPA-theory of Leibler, since this provides the basis that is usually used for analyzing experimental scattering data through the structure factor calculation.

8.1.1 Concentration Fluctuations in the Mean-Field Approximation

In the RPA mean field model of an AB-diblock copolymer, as presented by Ludwig Leibler, it is assumed that both blocks have the same statistical segment length, a, and that the melt is incompressible. In the Flory-Huggins model of free energy, the enthalpic energy density can be written (see, e.g., [15])

$$u(\bar{r}) = kT \cdot \chi \cdot \delta_A(\bar{r})\delta_B(\bar{r}) \tag{83}$$

where $\delta_A(\bar{r})$ and $\delta_B(\bar{r})$ are the local, relative densities of respectively A and B monomers at position $\bar{r}$, i.e., $\delta_A(\bar{r}) + \delta_B(\bar{r}) = 1$.

For positive χ-values, the energy term in equation (83) favours an inhomogeneous phase with the A-ridge domains

$$\langle(\delta_A(\bar{r})\rangle > f \quad \text{and} \quad \langle(\delta_B(\bar{r})\rangle < 1-f$$

and B-ridge domains with

$$\langle\delta_A(\bar{r})\rangle < f \text{ and } \langle\delta_B(\bar{r})\rangle > 1-f$$

In all positions the product $\delta_A(\bar{r})\delta_B(\bar{r})$ is thereby smaller than the factor $f(1-f)$, applicable for random mixing. The energy term in equation (83) is accordingly reduced, but on the cost of configurational entropy of mixing.

In general, it is the product χN of the interaction parameter and the degree of polymerization, N, that governs the phase behavior, as in polymer blends. For $\chi N = 0$, or χN sufficiently small, the entropy is dominant and the system exhibits an isotropic phase with sequences A and B of the chains interpenetrating each other so that everywhere in the sample

$$\langle\delta_A(\bar{r})\rangle = f \text{ and } \langle\delta_B(\bar{r})\rangle = 1-f \tag{84}$$

where $\langle\,\rangle$ denotes the thermal average. This phase is the disordered phase. When χN becomes larger (as a result of increasing molar weight, or changing temperature) the local concentration will deviate from average. These fluctuations from mean local density determines the order parameter

$$\psi(\bar{r}) = \langle\Delta\delta_A(\bar{r})\rangle = \langle\delta_A(\bar{r}) - f\rangle. \tag{85}$$

The fluctuations may be described by the density-density correlation functions correlating compositions in a given distance $\bar{r} - \bar{r}'$,

$$\gamma_{AA}(\bar{r}-\bar{r}') = 1/(kT)\langle\Delta\delta_A(\bar{r})\Delta\delta_A(\bar{r}')\rangle \tag{86}$$

and

$$\gamma_{AB}(\bar{r}-\bar{r}') = 1/(kT)\langle\Delta\delta_A(\bar{r})\Delta\delta_B(\bar{r}')\rangle \tag{87}$$

The Fourier transform of these correlations

$$S_{AA}(q) = \int e^{-i\bar{q}\cdot\bar{r}}\gamma_{AA}(\bar{r}-\bar{r}')d\bar{r} \tag{88}$$

and equivalent terms for S_{BB} and S_{AB}, are the partial structure factors. Assuming that the system is incompressible, these partial structure factors are highly correlated. It is thereby possibly to describe both S_{BB} and S_{AB} in terms of the partial structure factor S_{AA}, which can be measured in an elastic scattering experiment. In the scattering experiment, the correlation function γ_{AA} is determined by the differences in *scattering lengths densities* rather than the polymer density itself, as discussed in section 2.2. In equations (86), (87) and (88), one should accordingly make the trivial substitution of $\Delta\delta$ with $\Delta\rho$ allowed according to the Babinet principle, i.e. $\langle\Delta\delta_A(\bar{r})\Delta\delta_A(\bar{r}')\rangle$-term should be replaced by the $\langle\Delta\rho_A(\bar{r})\Delta\rho_A(\bar{r}')\rangle$-correlation function, ρ_i being the scattering length density of component i, i being either A or B.

The free energy of the system may be expanded in terms of the orderparameter ψ:

$$F = F_0 + kT\sum_{n=2}^{\infty}\nu^{-n}\frac{1}{n!}\sum_{\bar{q}_1,\ldots,\bar{q}_k}\Gamma_n(\bar{q}_1,\ldots,\bar{q}_n)\cdot\psi(\bar{q}_1)\ldots\psi(\bar{q}_n) \tag{89}$$

where $\psi(\bar{q}_i)$ is the Fourier transform of $\psi(\bar{r}_i)$ and the coefficients Γ_n are simple functions of the correlation functions $\gamma^{(n)}$, $\gamma^{(n-1)}, \ldots, \gamma^{(2)}$. When one confines the attention to the temperature region near or above the transition, all terms containing powers of ψ higher than the forth may be dropped out. The relevant correlation functions are thus [60]

$$\begin{aligned}
\tilde{\gamma}^{(1)}(\bar{r}_1) &= \langle \Delta\rho_A(\bar{r}_1)\rangle \\
\tilde{\gamma}^{(2)}(\bar{r}_1,\bar{r}_2) &= \langle \Delta\rho_A(\bar{r}_1) d\rho_A(\bar{r}_2)\rangle \\
\tilde{\gamma}^{(3)}(\bar{r}_1,\bar{r}_2,\bar{r}_3) &= \langle \Delta\rho_A(\bar{r}_1) d\rho_A(\bar{r}_2)\Delta\rho_A(\bar{r}_3)\rangle \\
\tilde{\gamma}^{(4)}(\bar{r}_1,\bar{r}_2,\bar{r}_3,\bar{r}_4) &= \langle \Delta\rho_A(\bar{r}_1)\Delta\rho_A(\bar{r}_2)\Delta\rho_A(\bar{r}_3)\Delta\rho_A(\bar{r}_4)\rangle \\
&\quad - \tilde{\gamma}^{(2)}(\bar{r}_1,\bar{r}_2)\cdot\tilde{\gamma}^{(2)}(\bar{r}_3,\bar{r}_4) - \tilde{\gamma}^{(2)}(\bar{r}_1,\bar{r}_3) \\
&\quad \cdot \tilde{\gamma}^{(2)}(\bar{r}_2,\bar{r}_4)
\end{aligned} \tag{90}$$

These correlation functions are generally difficult to calculate, but within the RPA approximation, one can express $S(q)$, $\tilde{\gamma}^{(3)}$ and $\tilde{\gamma}^{(4)}$ in terms of the correlation functions of the unperturbed polymer chains, S_{ij}. The basic assumption in the RPA-method is that the chains on the scale of the coil are approached the ideal chain (see section 5). When the interaction between monomers are switched off, the monomer density correlation functions are correspondingly equal to those of the ideal Gaussian chains. In the RPA theory, one thereby calculate the response of the system to an external potentials U_i as if the response functions were those of the ideal chains, while the potentials acting on monomers U_i^{eff} are corrected to take into account monomer interactions. The solution is obtained by expanding the order parameter in powers of the external potential

$$\psi = \psi^{(1)} + \psi^{(2)} + \psi^{(3)} \tag{91}$$

where $\psi^{(1)}$ is linear in U_i,

$$\psi^{(1)}(\bar{q}) = -\beta S_{ij}(\bar{q}) U_i(\bar{q}) \tag{92}$$

β being a coupling parameter. Equivalent, $\psi^{(2)}$ is linear in U_iU_j and $\psi^{(3)}$ in $U_iU_jU_k$. This gives [60]

$$S(\bar{q}) = W(\bar{q})/\left[\hat{S}(\bar{q}) - 2\chi W(\bar{q})\right] \tag{93}$$

where

$$W(\bar{q}) = S_{11}(\bar{q})S_{22}(\bar{q}) - S_{12}^2(\bar{q}) \tag{94}$$

and

$$\hat{S}(\bar{q}) = S_{11}(\bar{q})S_{22}(\bar{q}) + 2S_{12}(\bar{q}) \tag{95}$$

$W(q)$ denotes the determinant of the matrix $\|S\|$ whose elements S_{ij} are the correlation functions of the ideal, non-interacting copolymer chains. The correlation function of the unperturbed chains can for large N-values be approached [60]

$$S_{11} = N\gamma_1(f,x) \tag{96}$$

$$S_{22} = N\gamma_1(1-f,x) \tag{97}$$

$$S_{12} = S_{21} = \frac{1}{2}N\left[g_1(1,x) - g_1(f,x) - g_1(1-f,x)\right] \tag{98}$$

where $\gamma_1(f,x)$ is a generalized Debye function, defined as

$$g_1(f,x) = \frac{2}{x^2}\left[fx + \exp(-fx) - 1\right] \tag{99}$$

with $x = q^2R_g^2 = q^2Na^2/6$, R_g being the radius of gyration of the ideal chain with N segments of length a (see equation 38). The final result of the structure factor becomes hereby the simple and important form

$$S(\bar{q}) = \frac{N}{F(x) - 2\chi N} \tag{100}$$

with

$$\begin{aligned}
F(x) =& g_1(1,x)/\left[g_1(f,x)g_1(1-f,x)\right. \\
&\left. - 0.25(g_1(1,x) - g_1(f,x) - g_1(1-f,x))^2\right]
\end{aligned} \tag{101}$$

The scattering function as formulated in this RPA approximation, equation (100), has been the basis for numerous analysis of experimental data on block copolymers in the disordered phase.

Figure 29 shows examples of experimental data and fits using the analytical Leibler function. The experimental data are indeed fitted nicely by the structure factor of the RPA theory. The solid curves shown in the figure represents best fits convoluted by the experimental resolution function. In the insert is shown the

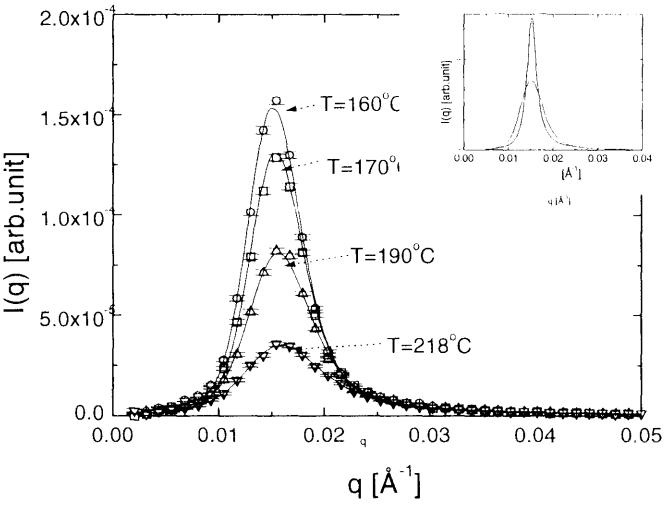

Figure 29 Example of experimental scattering function of a diblock copolymer, and fits using the meanfield RPA theory (solid line). The fits represent the model function including instrumental smearing. The effect of smearing is shown in the insert, giving the resulting Leibler function at 160 °C with and without smearing.

effect of instrumental smearing. In typical data analysis, however, both the polymer radius of gyration R_g and the Flory-Huggins interaction parameter χ are used as adjustable parameters. A nearly perfect fit is therefore possibly even though deviation from the mean-field predictions are evident, as for example variation in peak position q^* with temperature (beyond thermal expansion/contraction). Thus the agreement found in experiments cannot be taken as proof for the accuracy of the mean field RPA theory. Such a proof would require independent determination of R_g and χ. R_g can, in fact, be measured directly, as discussed below, using neutron scattering and specific labeling by exchange of hydrogen atoms with deuterium.

To find the order parameter one should look for the maximum of $S(q^*)$, i.e. the $q = q^*$ value where

$$dS(q)/dq = 0 \tag{102}$$

Using the equations above describing $S(q)$, it is implied that the solution of q^* does not depend implicit on χ. For symmetric block copolymers, $f = 0.5$, one finds

$$q^* R_g \simeq 1.945 \tag{103}$$

Plotting the inverse of this peak-value, $S^{-1}(q^*)$, as a function of reciprocal temperature, T^{-1} (or interaction parameter χ), one should according to the meanfield treatment get a straight line in analogy with the $S^{-1}(0)$-susceptibility of blends, equation (58), which as in usual second order phase transitions approach zero at the critical point, here the spinodal temperature. For symmetric block copolymers, $f = 0.5$, equation (100) and (101) leads to the critical value, $\chi_c N$:

$$\chi_c N = 10.495, \tag{104}$$

which should be compared with the corresponding critical value of binary blends, $\chi_c N = 2$, equation (60).

In real block copolymer systems the order parameter is significantly renormalized as the concentration fluctuations growth. This is discussed further below.

8.1.2 Effect of Polydispersity

Benoit and co-workers studied the influence of polydispersity on the scattering function [65]. They used the assumption that the interaction between two polymer molecules can be evaluated taking into account not only the direct contact, but also linear chains of contact. It was shown that a form equivalent to equation (100) is applicable, but with F, equation (101), replaced by

$$F(z,f) = \frac{z_1 + z_2 + 2z_{12}}{z_1 z_2 - z_1^2} \tag{105}$$

where it is assumed that the chains are Gaussian and that for each of the blocks, the normalized distribution of polymerizations are uncorrelated. Assuming the Zimm-Schultz distribution-function, z_1, z_2 and z_{12} have the form

$$z_i = 2f^2\left[\frac{1}{x_i} - \frac{1}{x_i^2} + \frac{1}{x_i^2}\left(\frac{1}{1+(x_i/(k_i-1))}\right)^{k_i-1}\right], \quad i = 1,2 \tag{106}$$

and

$$z_{12} = f(1-f)\frac{1}{x_1 x_2}\left[1 - \left(\frac{1}{1+(x_1/(k_1-1))}\right)^{k_1-1}\right] \times \left[1 - \left(\frac{1}{1+(x_2/(k_2-1))}\right)^{k_2-1}\right] \tag{107}$$

where

$$k_i = \left(1 - \frac{1}{M_w/M_n}\right)^{-1} \tag{108}$$

and $x_i = \frac{q^2 a_i^2 N_i}{6} = (qR_{g,i}^2$, in which a_i is the Gaussian coil statistical segment length as before.

In Figure 30 is shown the calculated structure factor in the case of no polydispersity, using Leibler's equation, and the structure factor of a diblock copolymer of similar size, but including polydispersity in each block of $M_w/M_n = 1.1$, following the theory of Benoit *et al.*, equation (105). A main difference between the two curves is the $S(q = 0)$ value, which in the polydisperse situation has a finite value. At high q-values, the polydispersity have no effect, as the $S(q)$ at these values probe local structures which are not influenced by dispersity. The peak-position q^* is lowered by 5–10%.

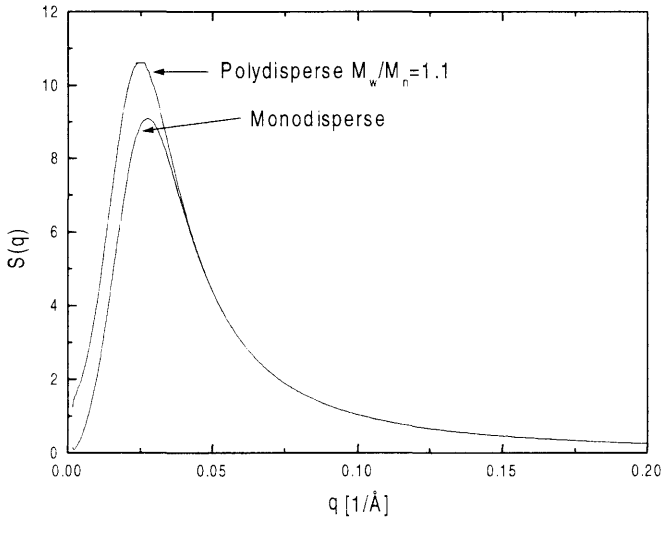

Figure 30 Calculation of the structure factor based on mean field RPA theory. The solid line represents the result of Leibler assuming no dispersity in polymer size. The broken curve represents the structure factor of a diblock copolymer of similar size, but including polydispersity in each block of $M_w/M_n = 1.1$, following the theory of Benoit *et al.*

8.1.3 Fluctuation Effects: Fredrickson Helfand Theory

The mean-field theory of Leibler agrees very well with experimental observations based on x-ray and neutron scattering when obtained relative far from the microphase separation temperature. In the vicinity of the MST, on the other hand, the mean field treatment is less accurate. Both Leibler and Fredrickson and Helfand noticed, that the effective Hamiltonian appropriate for diblock copolymers is in the same universality class as a model Hamiltonian considered by Brazovskii [60, 61, 66]. Based on the Hartree treatment used in the Brazovskii theory, Fredrickson and Helfand found that the structure factor can be written as the mean-field expression,

$$S(q) = \frac{N}{F(x) - 2\chi^{\text{ren}}N} \tag{109}$$

but with a renormalized Flory-Huggins parameter given by

$$\chi^{\text{ren}}N = \chi N - \tilde{c}\sqrt{S(q^*)N}, \tag{110}$$

where the factor $\tilde{c}\sqrt{S(q^*)}$ is composition dependent. For symmetric $f = 0.5$ diblock copolymers this yields a critical value of

$$\chi^{\text{ren}}N = 10.495 - 41.0(\bar{N})^{-1/3} \tag{111}$$

where $\bar{N}$ is the *generalized degree of polymerization*, characterizing the average number of chains in a volume R_0^3, where R_0 is the end-to-end statistical distance of the linear chain, $R_0^2 = 6R_g^3$

$$\bar{N} = R_0^3/V = N(a_{AB}^6)/v_0^2 \tag{112}$$

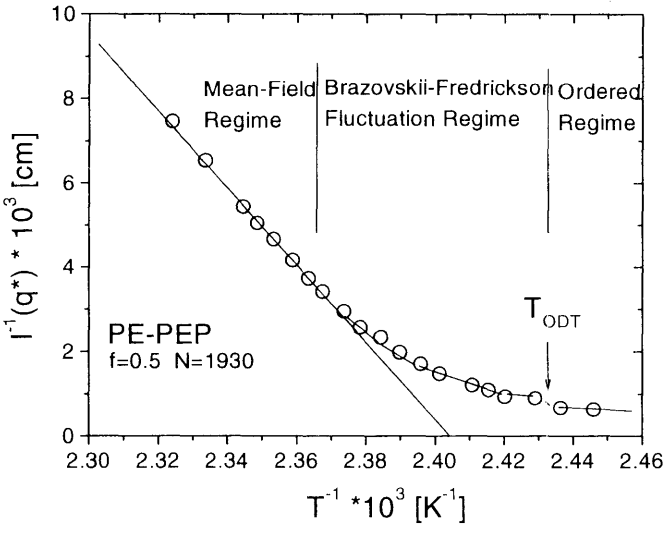

Figure 31 Illustration of the susceptibility $S^{-1}(q^*)$ versus temperature showing the fluctuation renormalisation near the T_{ODT}. The figure shows data of a symmetric PE-PEP diblock copolymer with $N = 1930$.

v_0 being the segment volume, and a_{AB} the averaged segment length

$$a_{AB}^2 = f_A a_A^2 + f_B a_B^2 \tag{113}$$

The fluctuation renormalisation thus makes the order parameter $S^{-1}(q^*)$ non-linear in χ, and thereby nonlinear in T^{-1}. This is shown in the experimental example given in Figure 31.

8.2 Gaussian, Weak and Strong Segregation Regimes

It appears from the discussion above on block copolymer melts, section 8.1, that it is the product χN that controls the degree of segregation between A and B blocks. Typically, the phase behavior with respect to segregation is categorized into three regimes, which we will denote: *Gaussian, weak* and *strong* segregation [67].

The Gaussian regime occurs when the chains are unperturbed and the concentration profile of fluctuations are sinusoidal, i.e., when the profile is well approximated by its first Fourier component. Matsen and Bates [68] discussed the three regimes based on the theoretical density profiles, but excluding fluctuation renormalisation. As a representative example, they discussed the symmetric $f = 0.5$ lamellar phase. Based on these calculations, the Gaussian-to-weak cross-over should occur at $\chi N \approx 12$, i.e., close to the mean-field critical point. Consequently, RPA is effectively only in the disordered regime. When fluctuations are taken into account, the Gaussian-to-weak segregation takes place in the disordered phase near $\chi N \approx 5$ [69–71].

The strong segregation regime appears when the middle of each domain becomes essentially pure one component and the interfaces narrow. From the calculated profiles [68], this means that the intermediate to strong segregation regime occurs between $\chi N \approx 25$ and 50, but the exact cross over value is rather arbitrary. N-values between 17 [72] and 95 [73] have been proposed for the cross-over between the weak and the strong segregation regimes.

In both the Leibler mean-field theory, and in the fluctuation-renormalized theories, it is assumed that the polymer coils obey Gaussian conformations. In reality, however, the polymer becomes still more stretched as the different blocks becomes more incompatible. The experimental determination of the various segregation regimes is often based on this stretching. In the Gaussian and in the strong segregation regimes, true scaling behavior is expected between polymer size and χN, but also the weak segregation regime can effectively be treated as obeying scaling behavior. Several recent theoretical mean-field approaches address such scaling behavior in the ordered state [68, 72, 74, 129, 76, 77, 73]. In these studies, the variation of the lamellar thickness with chain length is found to be stronger in the vicinity of the ODT than both in the Gaussian and in the strong segregation regime.

Experimentally, details of segregation profile in the ordered states can in principle be obtained from the relative intensities of the measured Bragg reflections. In practice, however, the number of Bragg peaks is often far too limited to give reliable details of the concentration profile.

The polymer stretching is rather determined based on the value of the correlation peak q^*. In the microphase separated state, this q^*-value gives the first order Bragg reflection, which for $f = 0.5$ is that of the lamellar structure.

Gaussian Regime

In the disordered phase without any significant segregation, the q^*-value is determined from polymer radius of gyration as

$$2\pi/q^* = \beta a N^{\alpha}, \qquad \alpha = 0.5 \tag{114}$$

giving the Gaussian regime. For the symmetric case, $f = 0.5$, the prefactor β is 1.318. Experimentally, the Gaussian $\alpha = 0.5$-scaling has been verified deep in the disordered phase for $\chi N < 5$ [69] as expected when fluctuations are taken into account [70, 71].

Weak Segregation

Self-consistent field theory (SCFT) [68] and calculations based on the random phase approximation (RPA) [78] show that the exponent α jumps to approximately 1.0 when weak segregation's are included. Experimentally, the weak segregation regime is characterized by an exponent of the order of 0.8–0.85 [69, 79, 80].

Strong Segregation

In the strong segregation limit, the lamellar periodicity, $d = 2\pi/q^*$, scale with an exponent of 2/3 consistent with both experiments [79–83] and theory [84–87]. The experiment by Hadziioannou and Skoulios [81] were made on symmetric, macroscopically oriented polystyrene-polyisoprene samples, while other data have been obtained on samples with isotropic texture. Helfand and Wasserman calculated the scaling relation based on a numerical, self-consistent field calculation, in which the free energy is determined by both enthalpic interactions at the interface and the entropy losses due to chain stretching and joint localization [84]. Semenov [85,86] and Ohta and Kawasaki [87] determined the scaling relation based on entropy loss due to chain stretching in a mean-field approach, using the random-phase approximation, giving the analytical expression

$$d = 2\left[(8\chi N)/(3\pi^4)\right]^{1/6} \cdot a\, N^{0.5} \tag{115}$$

The interfacial width strongly affects the structure factor, and should accordingly be incorporated in extended analysis of the Bragg reflections [86].

Experiments

Experimentally, the scaling relation for the three regimes can be measured through the location of q^*. In Figure 32 is shown the measured peak positions of two block copolymer systems, PS-PB and PEP-PEE, plotted versus chain length, N in a double logarithmic representation. The data which includes both results obtained using x-ray and neutron scattering, are given relative to the value of T_{ODT}.

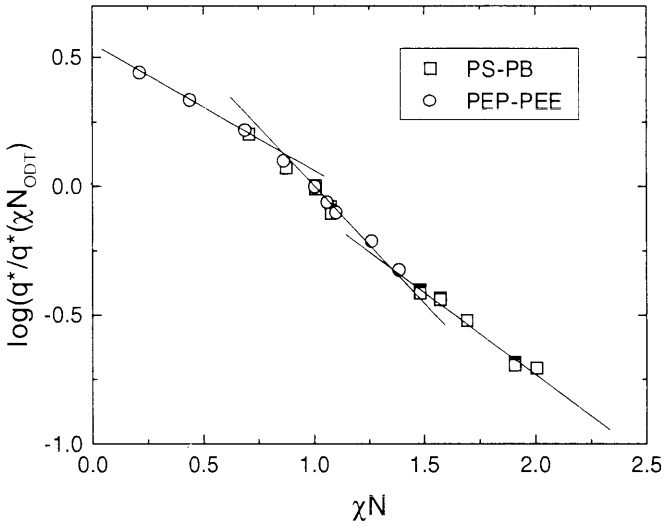

Figure 32 Peak positions, q^*, versus chain length, N multiplied by χ of PS-PB and PEP-PEE. The value of χ is based on the meanfield value at the order disorder transition. Full lines: weighted linear fits in appropriate χN-ranges. ODT is the order-disorder transition (reference Papadakis *et al. J. Phys.*, 7, 1829 (1997), and Almdal *et al., Phys. Rev. Lett.*, **1990**; 65: 1112).

8.2.1 Direct Measurement of Polymer Size

Experimentally, the polymer size can alternatively be measured in a scattering experiment by specific labeling of some coils [88, 89]. It should be noted, however, that the value measured by labeling and the value obtained from the q^*-position does not necessarily reflect the same physical size. Labeling experiments gives in the ordered phase when the sample texture is isotropic, a value averaged between the sizes parallel and perpendicular to the lamellae's. The peak-position q^* gives, on the opposite, specifically the perpendicular component.

Experimental measurements of the chain stretching as a function of incompatibility can, in principle be done either by changing the χ-value (by changing temperature) or by changing the molecular weight through synthesis of a homologous series of polymers. The former method provides in general only a relative small regime of χN, but very detailed measurements can be done near for example the order-disorder phase transition. Stamm and co-workers [89] measured the polymer size in both ways on a block copolymer system of polystyrene-polyparamethylstyrene (PS-PPMS), as shown in Figure 33.

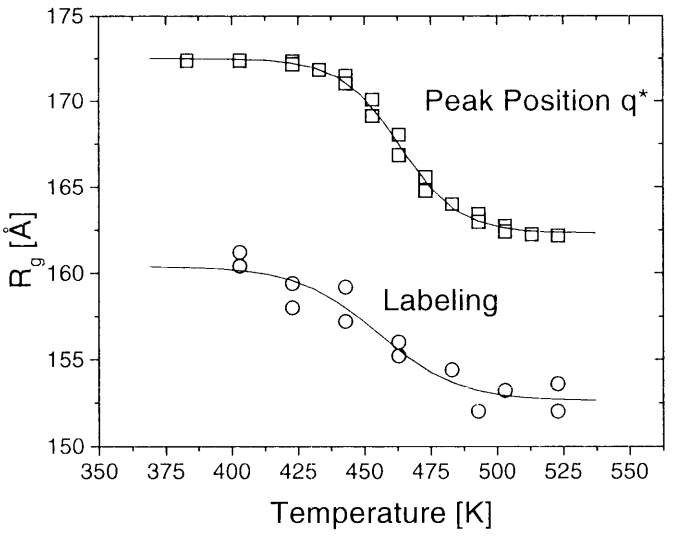

Figure 33 Polymer radius of gyration near the order-disorder transition temperature, as measured directly by specific deuterium labeling and from the peak-position q*. (reproduced from Bartels *et al., Eur. Phys. Lett.*, **1995**; 31: 81).

8.3 Order-Disorder Transition and Microphase Separation

8.3.1 Leibler RPA Theory

Within the meanfield RPA theory, one considers the polymer melt near its spinodal point, i.e., when χN is close to the critical value $\chi_s N$ for which $S(q^*)$ diverges, according to equation (100). Using a Landau type of analysis, the free energy is described in terms of the order parameter ψ. The quadratic term of the free energy expansion with respect to ψ:

$$F^{(2)} \sim \sum_{q} S^{-1}(\bar{q})\psi(q)\psi(-\bar{q}) \tag{116}$$

has a singularity near $|q| = q^*$. Since the contributions from higher order terms in ψ have no singularities, the important fluctuations must be those with wave vector $|\bar{q}| = q^*$, so that the order parameter $\psi(\bar{r})$ may be approximated by [60]:

$$\psi(\bar{r}) = S^{-1}(q^*) \sum_{q \in \{\pm Q_i\}} \psi(\bar{q}) \exp(i\bar{q}\bar{r}) \quad |\bar{Q}_i| = q^*, \quad i = 1, \ldots, n \tag{117}$$

giving

$$F^{(2)} = 2N(\chi_s - \chi) \sum_{q \in \{\pm Q_i\}} |\psi(\bar{q})|^2 \tag{118}$$

The coefficient of this term is independent of the specific sets $\{Q_i\}$. The third and forth order terms of the free energy with respect to ψ depends critically on the set $\{Q_i\}$, however. For this reason the prediction of the conditions for microphase separation requires detailed analysis of $F^{(3)}$ and $F^{(4)}$. For asymmetric diblock copolymers, $f \neq 0.5$, the third order term does not vanish at the spinodal, and the effective MST is in the mean field RPA a weak first order transition, with the asymptotic spinodal point positioned slightly inside the ordered phase. Only for $f = 0.5$ the mean-field RPA analysis predicts a second order critical point between the disorder and the lamellar structure. In all cases, the RPA theory predicts that the effective microphase separation temperature, $T_{MST}((\chi N)_{MST})$ and the ordering temperature $T_{ODT}((\chi N)_{ODT})$ is the same.

The mean field RPA theory shows to a large extend agreement with experimental results, both with respect to the structure of the disordered phase and the sequence of ordered structures. In practice, however, there is even for the $f = 0.5$ no second order critical point. On the contrary, lines of first order transitions between disordered and ordered structures are found. These observations can be explained including fluctuations, as discussed below. New experiments indicate in addition a decoupling of the ODT and the MST, at least for non-symmetric diblock copolymer systems.

8.3.2 Micellar Precursor

The Leibler function, equation (100) and (109) is, independent of whether fluctuation renormailzations are included or not, characterized by the pronounced correlation peak, and relative featureless behavior at higher q-values with no signature of secondary correlation peaks. This is a consequence of the fact that there in the fluctuating state are no interfaces, but a near sinusoidal density profile. Recent experiments have, however, shown clear indication of secondary peaks in the correlation function, signifying phase separation into micelles [90]. The scattering function of such micelles are discussed further in section 9 below.

Other signature of micellar precursors, i.e., separation between the micro-phase separation temperature and the order-disorder transition comes from dynamical studies showing different time constants for ordering and for phase separation [91]. The microphase separation temperature is equivalent to the critical micellar temperature (cmt) well known from both classical and block copolymer surfactants in selective solvents [92]. Thermodynamically, the micellar precursor in block copolymer melts can be understood as a consequence of polydispersity, resulting in an effective multicomponent system.

8.3.3 Fluctuation Effects on the Order-Disorder Transition

Fredrickson and Helfand applied, as already mentioned, a Hartree approach using the fact that the Hamiltonian describing block copolymers belong to the same

universality class as the model Hamiltonian considered by Brazovskii in 1975 [61, 66]. The Brazovskii-Hamiltonian is, among others, well known to account for the phase behavior of weakly anisotropic anti-ferromagnets, and liquid crystals near the nematic to smectic-C transition. Such systems are characterized by having large fluctuations not only near a single wave vector, but also in the vicinity of a shell of non-zero wave vectors. Brazovskii showed that this universality class exhibits a fluctuation induces first order phase transition in place of the continuous 2nd order transition predicted by Leibler's mean field theory. Diblock copolymers are accordingly not expected to show critical scaling in the very near vicinity of the transition temperature. This is in contrast to the homopolymer blends, discussed above.

An interesting feature of block copolymers that distinguishes them from typical systems in the Brazovskii universality class is that the fluctuation corrections to mean field theory can, in principle, be made arbitrarily small by increasing the molar mass of the chains. This is analogous to the situation for homopolymer blends, where non-classical corrections to mean field theory, given as the Ginzburg number, can vanish as the length of the chains approaches infinity.

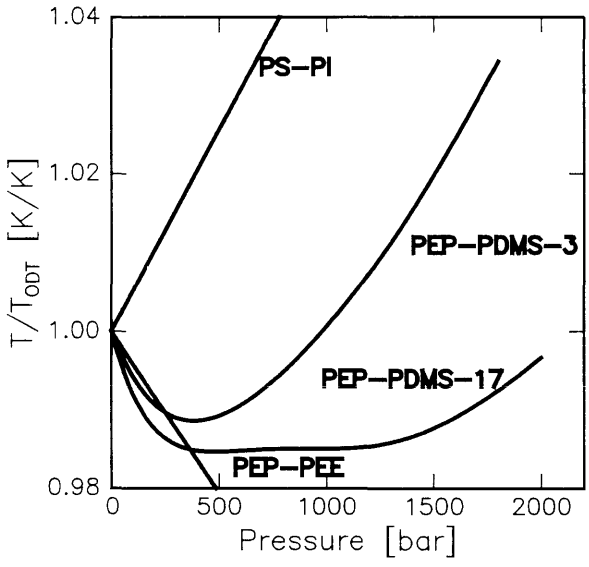

Figure 34 Pressure dependence of the order-disorder temperature for different diblock copolymers: PS-PI (Hasegawa *et al., J. Phys. Chem. Sol.*, **1999**; 60: 1307), PEP-PEE (Frielinghaus *et al., Macromolecules*, **1995**; 29: 3263), and two PEP-PDMS varying in molar mass (Schwahn *et al. Phys. Rev. Lett.*, **1997**; 77: 3152).

8.3.4 Order-Disorder Transition Dependence of Pressure

It has from both experiments and theory been argued that a main reason that fluctuations significantly renormalize the critical behavior in polymers is related to the free volume of polymer materials. Experimentally, this can be proven by application of hydrodynamic pressure as an additional thermodynamic parameter. The effect of pressure is primarily to reduce the free volume. In binary homopolymer blends, hydrodynamic pressure shifts accordingly the phase boundaries to higher temperatures, i.e., $\Delta T_c/\Delta P > 0$ and pressure lowers the Ginzburg number (see section 8). The change of phase-behavior were in section 8.1 analyzed in terms of pressure related changes in the enthalpic part of the free energy, i.e., in the Flory-Huggins interaction parameter, χ. The experimentally observed changes in phase behavior upon application of pressure were hereby concluded to be mainly related to a decrease of the entropic term, χ_σ of the Flory-Huggins parameter (see equation 54), i.e., $\Delta|\chi_\sigma|/\Delta P < 0$. This behavior is quite reasonable according to equation of state theories where the entropic term χ_σ is directly related to the compressibility and thereby the free volume of the sample [93].

In contrast to homopolymer blends, present published data on block-copolymer systems do not show any significant change in the Ginzburg number as a function of pressure [94]. The order-disorder transition temperature, T_{ODT}, however, has marked pressure dependence. In Figure 34 is shown the pressure dependence of various block copolymers [94–98]. It appears that the pressure dependence is rather diverging, with both positive and negative slopes of T_{ODT} versus P. The divergent behavior of T_{ODT} versus P reflects that the free energy of the system is determined by critical competition between entropic and enthalpic terms.

Small-angle scattering studies on a near symmetric diblock copolymer poly(styrene)-poly(isoprene), PS-PI, showed that the order-disorder phase boundary increases with pressure with a rate in the relative change in the microphase separation temperature T_{MST} of the order of $\Delta T_{MST}/\Delta P \sim 0.05 \cdot T_{MST}/\text{kbar}$ [96], while a block copolymer of poly(butadiene-1,4)-poly(isoprene), PB-PI, shows a significantly steeper pressure dependence, $\Delta T_{MST}/\Delta P \sim 0.65 \cdot T_{MST}/\text{kbar}$ [95]. Studies on poly(ethylenepropylene)-poly(ethylethylene), PEP-PEE gives a slope of reversed sign: $\Delta T_{MST}/\Delta P \sim -0.4 \cdot T_{MST}/\text{kbar}$ [97]. Most unusual is the phase behavior of the PDMS-systems, showing first a decreases in T_{ODT} and then an increase.

The pressure dependence of order-order transitions has only been measured in a single block copolymer, PEE-PEP, showing only minor, if any, influence [97].

A different type of pressure experiment was made on diblock copolymers of poly(styrene)-poly(paramethylstyrene), PS-PPMS, showing an apparent decrease in the T_{ODT} upon application of pressure [99]. The original experiments were made by application of pressure at high temperature, where processing is easy and then quenching the material for structural studies to be

performed at ambient temperature. Preliminary structural studies made under controlled hydrodynamic conditions showed, however, that the apparent change in order-disorder transition temperature upon quenching from a well-defined temperature with different applied pressures do not reflect thermodynamic equilibrium. The original scattering data rather reflect the pressure dependence of the glass-transition temperature, T_g, of poly(styrene). The studies under thermodynamic equilibrium showed on the contrary, that the order-disorder boundary in reality is increasing upon application of pressure.

The implication of non-zero compressibility of diblock copolymers has been taken into account in some theoretical studies. Freed, Dudowicz and coworkers applied a formalism based on a compressible random-phase approximation and lattice cluster theory [93, 100–103]. They presented scattering curves for disordered diblocks as a function of the free volume inversely related to the applied pressure. Their models suggested that the effect of pressure should be small far from the order-disorder transition, but might be substantially close to the T_{ODT}-transition. Bidkar and Sanchez applied a combined random phase and lattice fluid theory to calculate the influence of free volume, and thus dependence on pressure of the χ-parameter [104]. Bidkar and Sanchez conclude that the scattering experiments still may approach the correct thermodynamic $S(q)$-limit at $q = 0$, but free volume leads to an increase in the apparent molecular radius of gyration, R_g, obtained if calculated based on classical Ornstein-Zernike theory.

8.3.5 Order-Disorder Transition Dependence on Shear

Experimental studies applying shear on block copolymers has to the present mainly focused on the possibility to shear-align poly-crystalline mesophases into samples of well defined texture. Keller *et al.* and Hadziioannou *et al.* made already in the 70th the pioneering studies on commercial available polystyrene-polyisoprene-polystyrene (PS-PI-PS) showing the possibility to shear align the hexagonally packed cylinder phase [105, 106]. During the 90th a number of studies have been made on a variety of polymer systems, covering both the classical phases: micellar $Im\bar{3}m$ (*bcc*) [107], hexagonally ordered cylinders (*hex*) and lamellar (*lam*); the more recent discovered bicontinuous $Ia\bar{3}d$-cubic phase [108–110], and the thermodynamic metastable phase of perforated lamellar structure (*pl*) [111].

Renewed interests in the field of shear dependence began with the discovery of the possibility of detailed control of the lamellar orientations [112]. Using reciprocal steady-shear field on a PEP-PEE system, Koppi *et al.* observed that either the parallel or the perpendicular orientation could be achieved, depending on the temperature and rate of deformation. Later work has been done by Winey *et al.* [113], Patel *et al.* [114], Zhang *et al.* [115, 116], including rather detailed outline on the transformation between the various alignments. Hashimoto *et al.* revealed by application of x-ray synchrotron instrumentation large dynamic lattice transformations during the shear [117].

The understanding of block copolymers under shear is still relative limited. Cates and Millner [118] evaluated the effect of a steady shear flow on the disorder-to-lamellar transition in diblock copolymer melts and found that large strain shear suppresses concentration fluctuations, driving the sample into a more meanfield-like state. They predicted a quadratic increase in T_{ODT} with increasing shear rate, as well as a shear-rate dependent spinodal ordering temperature, T_s, that increases as $\dot{\gamma}^{1/3}$. Cates and Millner also predicted that fluctuations should be suppressed anisotropically, leading to a perpendicular orientation upon ordering, as discussed below. Subsequently, Marques and Cates [119], extended the Cates-Millner approach to include the hexagonal cylinder phase, and found correspondingly an increase in the disorder-to-hex transition temperature with increasing shear rate.

A modification of the Cates-Milner theory by Fredrickson [120] indroduced the concept of mechanical contrast, i.e., mismatch in mechanical response between blocks in a lamellar melt. In the low shear rate limit, $\dot{\gamma} \ll \dot{\gamma}^*$, where $\dot{\gamma}$ is the shear rate and $\dot{\gamma}^*$ is related to the inverse of the fluctuation life time, the Cates-Milner results of a quadratically increasing ordering temperature with $\dot{\gamma}$ is recovered. However, Fredrickson also finds that the parallel alignment is most stable just below T_{ODT} in this low shear rate limit. For $\dot{\gamma} \gg \dot{\gamma}^*$, perpendicular lamellae are most stable just below T_{ODT}, but further cooling yields a transition to the parallel orientation. The temperature, at which this perpendicular-to-parallel transition occurs, depend on the magnitude of the mechanical contrast in the melt, but is further predicted to be independent of shear rate. The latter point is in contradiction to most experimental observations.

The development of *in-situ* shearing devices have provided the means for testing the theoretical predictions. Both increase and decrease in ordering temperature has been observed experimentally. Koppi *et al.* [121] and Bates *et al.* [122, 107] examined the effect of a reciprocating steady shear on respectively lamellar and hexagonal forming PEP-PEE diblock copolymers, and found that T_{ODT} increases with shear rate in a manner consistent with the quadratic scaling. In Figure 35 is shown the shear rate dependent T_{ODT} of the disorder-to-hex transition, as well as two-dimensional contour plots of the two phases. Experimental data on triblock copolymers show more diverging facts. Nakatani *et al.* found an increasing T_{ODT} with shear in a hex-forming PS-PB-PS melt. Upon continued shear, however, the observed induced order apparently vanish after some

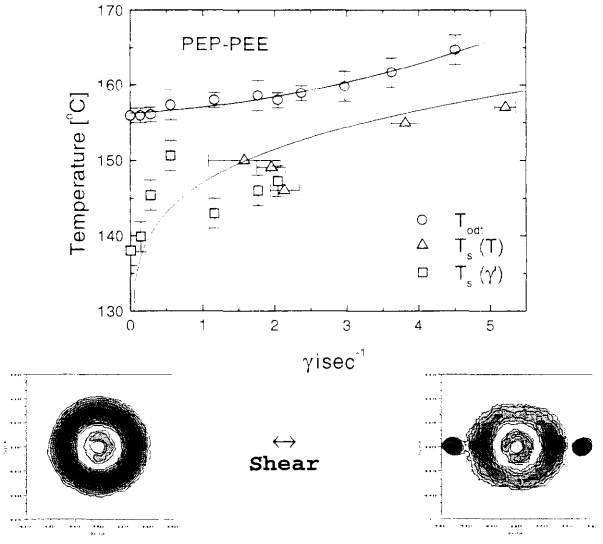

Figure 35 Shear rate dependence of the Order-to-Disorder transition in a PEP-PEE diblock copolymer. The contour plots clearly show the corresponding changes in scattering pattern upon application of shear: left, disordered at low shear rate, and right: ordered (hex) at high shear rate (reference Bates *et al.*, *Macromolecules*, **1994**; 27: 5934; Almdal *et al. J. Physique*, **1996**; 6: 617).

time [124]. Winter *et al.* [125] and Bates *et al.* [126,127] reported a suppression of T_{ODT} with increasing shear rate in respectively hex-forming PS-PI-PS and lamellar forming PEP-PEE-PEP.

8.4 Ordered Phases

Up to the present, we have discussed the disordered phase into some detail, but not gone much into a discussion on the phase behavior beyond the point where the order-parameter diverges. In this regime the microphase separation results in mesoscopic ordered structures. A significant amount of the attention that block copolymers in recent years have received concerns actually these self-assembled microstructures. Various geometry's occurs depending on the spontaneous curvature of the internal surface, which is produced by the differences in both volume fractions f, in mismatch in entropic stretching energy of the different blocks, and the degree of fluctuations as manifested through the degree of polymerization $\bar{N}$ [55]. A number of theoretical scenarios have been presented, however, the outcome seems to depend on subtleties in the calculations, in particular near the T_{ODT}. The predicted ordered phases differ therefore somewhat from each other.

Most models that have been proposed are based on effectively hard core interactions by implementing an incompressibility constraint where the average segment concentration is forced to be uniform. The remaining interactions are assumed to be local and are treated by an enthalpic term, like

$$FN/kT = \chi N \rho_0 \int \varphi_A(\bar{r})\varphi_B(\bar{r})d\bar{r} \qquad (119)$$

where $\varphi_A(\bar{r})$ and $\varphi_B(\bar{r})$ are the volume fraction of A and B segments, respectively. This simplified model for block copolymer melts retains the three most important ingredients: (i) entropic chain stretching, (ii) incompressibility, and (iii) immiscibility between unlike segments. The thermodynamics of even such simplified standard model cannot, however, be determined exactly [68].

Within the mean field RPA theory used by Leibler, only the coefficient of the second order term of the Landau expansion of the free energy is independent of the specific sets of wave-numbers $\{\bar{Q}_i\}$. The third and forth order terms, $F^{(3)}$ and $F^{(4)}$, depends critically on the set $\{\bar{Q}_i\}$ (see paragraph 8.3.1). For an ordered mesophase characterized by the set of vectors $\{\bar{Q}_i\}(i = 1,2, \ldots, n)$, its free energy density may be written in the form

$$FN/kT = 2(\chi_s - \chi)N\psi_n^2 - \alpha_n\psi_n^2 + \beta_n\psi_n^3 \qquad (120)$$

where the coefficients α_n and β_m are calculated based on the correlation functions of non-interacting Gaussian chains [60].

The equilibrium value of the amplitude ψ_n for an ordered phase is then to be determined by minimizing the free energy density with respect to ψ_n, i.e., for a given χN-value, the stable phase is that corresponding to the smallest free energy $F(\bar{\psi}_n)$. With this approach, Leibler determined the stability of the classical ordered structures and the condition for mesophase transitions. In the symmetric $f = 0.5$ case, the transition should be of second order, going from the disordered directly to the lamellar structure. For $f \neq 0.5$, the transition is weakly first order. In the very near vicinity of the disordered phase the minority component forms spherical micellar domains that are arranged on a bcc lattice with the matrix consisting of the majority component. Upon further decrease in T, (increase in χN) the mean field RPA predicts a first order transitions to the hexagonal ordered phase, where cylinders are formed by the minority component. Finally, after even further decrease in T, a first order transition to the lamellar structure is predicted.

8.4.1 Conformational Asymmetry

In the conformational symmetric case, where the A and the B statistical segment lengths are equal, the phase diagram will be symmetric with respect to A and B composition, i.e., around $f = 0.5$. Presence of segmental anisotropy, on the other hand, can account for asymmetry in the phase behavior, as observed in scattering experiments (see e.g., [55]) and accounted for theoretically [64]. Conformational asymmetry can be characterized by the parameter ϵ defined as

$$\epsilon = \beta_A^2/\beta_B^2 \quad (121)$$

where β gauges the space-filling characteristic

$$\beta^2 = R_g^2/V = a^2/6v \quad (122)$$

8.4.2 Thermodynamically Stable Phases

Leibler's work could, as discussed above, be mapped onto the Brazovskii Hamiltonian allowing calculations beyond mean field [61]. The effect of fluctuation renormalisation is not only to shift the phase boundaries to larger χN-values, it also changes the second order critical point to a line of first-order transition between the disordered and the lamellar phase. In addition, the fluctuation renormalisation causes a direct transition from the disordered phase to the hexagonal rod phase. The cubic *bcc* phase is quite substantially limited to highly asymmetric block copolymer architectures, though depending on the overall degree of polymerization.

Semenov addressed the structures of micellar block copolymer systems using mean-field theory and found the sequence of order: fcc → hex → bcc [128]. Vavasour's and Whitmore's mean-field approach [129] unified the predictions made by respectively Leibler [60] and Helfand and Wasserman [130] and found for asymmetric diblock copolymers qualitatively the same result as those obtained using the fluctuation theory [61]. Hamley and Bates [131] assessed the stability of various cubic phases other than the bcc phase near the T_{ODT} and found that, for all values of f, the fcc and the two-dimensional square structure (ml) are not stable. Marques and Cates showed that the simple cubic phase is also not stable [132]. Matsen and Bates used self-consistent field theory and predicted the sequence *dis* → *close-packed spheres* → *bcc* → *hex* with the close-packed sphere phase probably being hexagonally close-packed (hcp) near the ODT and *fcc* further away from the ODT [68] Matsen and Bates also showed the stability of the bicontinuous cubic structure Ia$\bar{3}$d, often named the gyroid structure according to theories on minimal surfaces calculations.

The experimental challenge related to the ordered block copolymer structures concerns both unique crystallographic identification of the phases, but also verification of the stability of the ordered microstructures. Since the characteristic dynamics of high molar mass polymer systems is often very slow, it is a real problem to conclude that an observed ordered phase is thermodynamically stable. Crystallographic description of the ordered structure has, in principle, to be solved like the investigation of any classic crystal, but the large length scale, and the amorphous building units give, of cause, a number of special features. A particular powerful method has been the application of combined x-ray scattering and transmission electron microscopy, TEM.

Small-angle x-ray scattering has been used for a number of the block copolymers to solve their ordered microstructures. By identifying the sequence of Bragg-reflections, the ordered structure can be identified according to standard crystallographic tables, as that given in Table 4. Assuming that the powder is ideal, i.e., without significant texture, the relative intensity of the different Bragg-peaks can further be used to obtain information beyond just the ordering symmetry. Not much has been done in that respect up to now, however, partly due to the still relative limit number of Bragg reflections that can be observed, and partly due to difficult background treatment in x-ray experiments.

Alternative to the powder technique, the ordered block copolymer can be made into a single crystal by application of appropriate fields. Shear fields are in particular good for such induced bulk orientation. The detailed structure have been identified for a number of diblock copolymers by making scattering experiments in the three principal directions of such shear aligned samples: beam parallel to shear gradient, beam parallel to shear-flow, and beam parallel to the neutral direction [133].

More recently, more detailed crystallographic studies have been made either having the shear-instrument in situ with the scattering facility, thus providing possibility for online alignment, or the shear aligned sample

Table 4 Crystallographic miller indices of common ordered block copolymer mesophases.

Simple cubic sc	*Body centred cubic Im$\bar{3}$m* bcc	*Face centred cubic* fcc	*Bicontinuous cubic* (G) Ia$\bar{3}$d	*Hexagolan Cylinder* hex	*Lamellar* lam
100	110	111	211	10	1
110	200	200	229	11	2
111	211	220	321	20	3
200	220	311	400	21	4
210	310	222	420	30	5
211	222	400	332	22	6
220	321	331	442	31	7
300	400	420	431	40	8
221	411	422	521	32	9
310	330	511	440	41	10

was transferred to a goniometer providing very detailed crystallographic investigation [110].

Still, many block copolymers might suffer from final identification of the mesoscopic order, simple due to lack of higher order reflections. Typical block copolymer samples show rather weak higher order reflections. This is both a result of relative low coherence of many ordered phases, *para*-crystallinity, and due to the form factor (see equation 8.16). The building blocks of the block copolymer have sizes comparable to the lattice distance, causing major reduction in intensity at high-order reflections. Moreover, the concentration profile, and thereby the profile of the scattering contrast, have near the order-disorder transition close to sinusoidal profile, giving only significant intensity in the first harmonics.

In Figure 37 is shown an example of a phase diagram, i.e., the diagram of the various ordered microstructure of block copolymers with varying volume fraction f and different molecular sizes [55, 134]. The diagram shows beyond the classical phases lamellar, hexagonal and bcc, also the bicontinuous Ia$\bar{3}$d, and modulated lamellar structures, *ml*. The *ml* structures have since these data were published been shown, both theoretically and experimentally, to be metastable governed by fluctuations.

8.4.3 Epitaxy

Transformations between ordered phases in block copolymer melts involve in general a large-scale reorganization of macromolecular aggregates comprised of the polymer chains. It has been shown that such transformations can occur epitaxially, i.e., the nucleation and growth of new structures upon passing an order-order transitions lead to preferred crystallographic orientations that are governed by symmetry and lattice spacing relationships between the original and the transformed state. Schultz *et al.* [108] and Hillmyer *et al.* [109] discovered the epitaxy between lamellar, hexagonal and the cubic bicontinuous Ia$\bar{3}$d structure. The {221} planes of Ia$\bar{3}$d were found to be epitaxially related to the {001} planes of the lamellar phase and the {10} planes of the hexagonal structure. Intermediate between the lamellar and the Ia$\bar{3}$d phase one usually find the non-equilibrium modulated lamellar phase (ml). The ml-phases are often very long lived, and experimentally difficult to distinguish from stable structures [111, 135]. Figure 36 shows an experimental study of PEP-PDMS diblock copolymer where the Ia$\bar{3}$d phase slowly grows out of the metastable ml-phase. The evolution in both structure and mechanical modulus are followed continuously [110].

9 Micelle

In the sections above on block copolymer melts it was discussed how incompatibility between different parts of the molecules can lead to various self-organized structures, the ordered mesophases. When block copolymers are mixed with a solvent selective for only one of the block types, the molecules tend also to self-assembly into well-organized structures to minimize direct contact between the immiscible units. This self-association gives rise to a wide range of phase behavior, including the formation of micelles of various form and sizes, complex structured microemulsions, and liquid crystalline phases on the mesoscopic length scale.

Scattering experiments is among the most important tools to provide information on size and form of the polymeric aggregates and on the thermodynamics characterizing the self-assembling, including the unimer-to-micelle transformation. Scattering data can

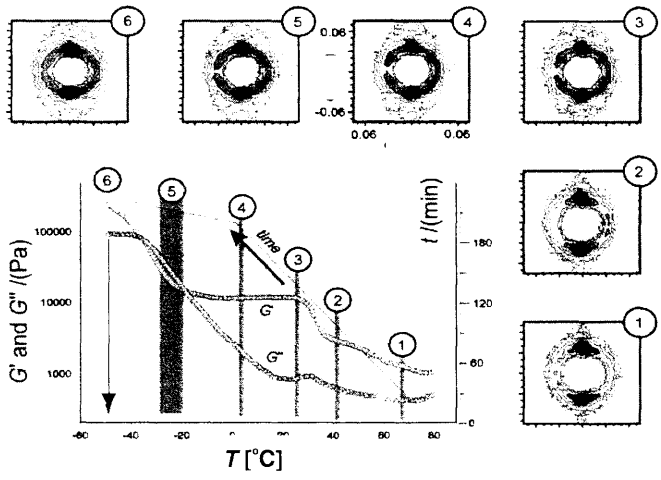

Figure 36 Simultaneous measurement of mechanical and structural properties using an instrumental setup with a rheometer online, as shown in section III (reference Vigild *et al.*, *Macromolecules*, **1998**; 31: 5702).

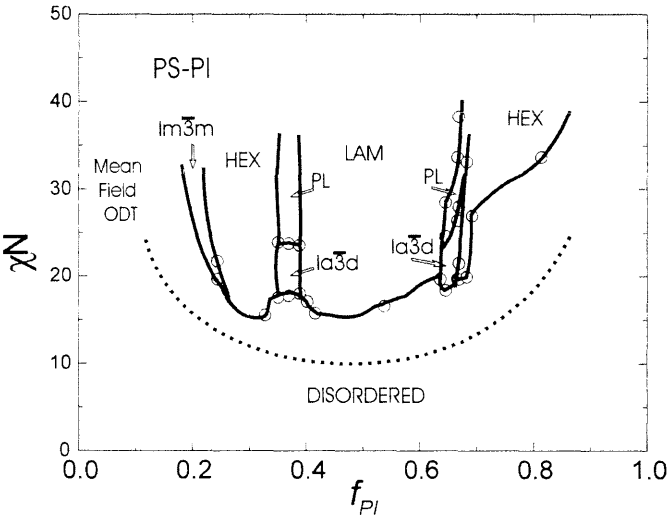

Figure 37 Experimental phase diagram of a diblock copolymer melt: polystyrene-polyisoprene, PS-PI (reference Khandpur *et al.*, *Macromolecules*, **1995**; 28: 8796).

potentially give both detailed information on structure of copolymer aggregates and information on the interactions between adjacent aggregates.

Block copolymers in selective solvents might form a variety of aggregates, depending on the detailed molecular architecture. Often, the polymers then self-associate into microscopic very well defined aggregates where the non-soluble parts form a core shielded from the solution by the soluble blocks. Such micellar aggregates may have the form of spherical objects, or they may be elongated stiff rods or flexible 'worms-like' structures, or have the form of flat discs. More complex structures can also be found, as for example networks of micelles or bi-continuous phases.

Below we will discuss both di- and tri-block copolymers which self-organize into micellar aggregates. We will discuss AB, ABA and BAB type of chemical architecture, where A represents the soluble block. The AB and ABA type of systems to be discussed organize typically in individual micellar aggregates, which interact through a near hard-sphere type of potential. Such micellar systems are sketched in Figure 38(a). BAB polymers may also form individual micelles, but this implies that all polymer chains start and end in the same micelle having the middle A-block dispersed into the liquid, the so-called flower-micelles. More likely, such micelles form interconnected networks, where cores are connected by the soluble A-polymer block, as shown schematically in Figure 38(b) and (c).

Scattering experiments give important insight into the assembling characteristics. The lower row of Figure 38 show the characteristic scattering pattern, $I(q)$ versus q, as expected from aggregates of respectively AB (or ABA) and BAB type of block copolymers. The broad peak at high q-values reflects the form factor of the micellar cores. The peak at low angles is indicative of interacting micelles. The peak position and width reflects the (local) micellar volume fraction and the interaction potential. The scattering function of the micellar cluster reflects this locally more dense system by having a more narrow peak positioned at a higher q-value. The additional scattering near $q = 0$ reflects the clustering of micelles.

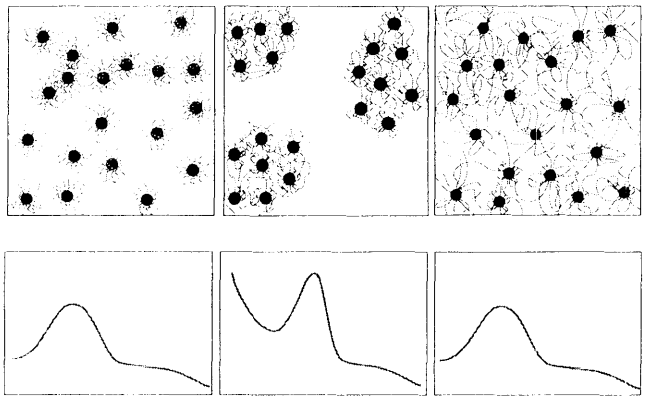

Figure 38 Schematic representation of spherical micelles of ABA (or AB) and BAB type of block copolymers in A-solvent, and their respective scattering functions. (a) ABA micelles resulting in independent hard-sphere interacting spherical aggregates. (b) BAB-micelles making up clusters of interconnected micelles. (c) BAB-micelles making up a near homogeneous micellar network structure.

In the text below is given a variety of examples of scattering data of aggregates like micelles and other microemulsions and the related data analysis. It is assumed that the polymer aggregates are monodisperse and randomly oriented, so equation (16) is valid. We will review some of the most important analytical expressions for the scattering function of typical block copolymer aggregates, including micelles with spherical, elliptical or rod-like shapes. Most of the expressions can be found in the book of Guinier and Fournet [6], or in the extended list of known scattering cross sections recently summarized by Pedersen [136].

9.1 Micellar Form Factor

9.1.1 Spherical Micelle

Micelles might in many cases be approached a simple, dense sphere. The form factor, P_{sp} of such homogeneous spherical particle with radius R_c has the analytical form [6]

$$P_{sp}(q) = [\Phi_{sp}(q)]^2 = \left[\frac{3}{(qR_c)^3}(\sin(qR_c) - qR_c\cos(qR_c))\right]^2 \tag{123}$$

which approach the $P_{sp}(q) \propto q^{-4}$ Porod law at large q-values.

The form factor equation (123) represents a good approximation to block copolymer micelles if they form a dense spherical aggregate with only small corona, or if the contrast of the micellar corona has been matched to the solvent (see Figure 3 in section 2). The 'D_2O-data' of block copolymer micelles shown in Figure 39 represents the latter situation of contrast matched corona [137, 138].

Typically, however, micelles formed from polymers are of the 'star-type' (Figure 38) with relative dense cores of the non-soluble blocks and with a corona of mixed polymer and solvent. To a first approximation, such micelles can be approached the core and shell model shown schematically in Figure 3.

The form factor of a single shell with inner and outer radius R_1 and R_2, respectively, is obtained from the form factor of dense sphere, $P = P_{sp}$ (equation 123) by subtracting the empty core with the proper volume weighting [6]:

$$P_{shell}(q) = \frac{V(R_1)P_{sphere}(q, R_1) - V(R_2)P_{sphere}(q, R_2)}{V(R_1) - V(R_2)} \tag{124}$$

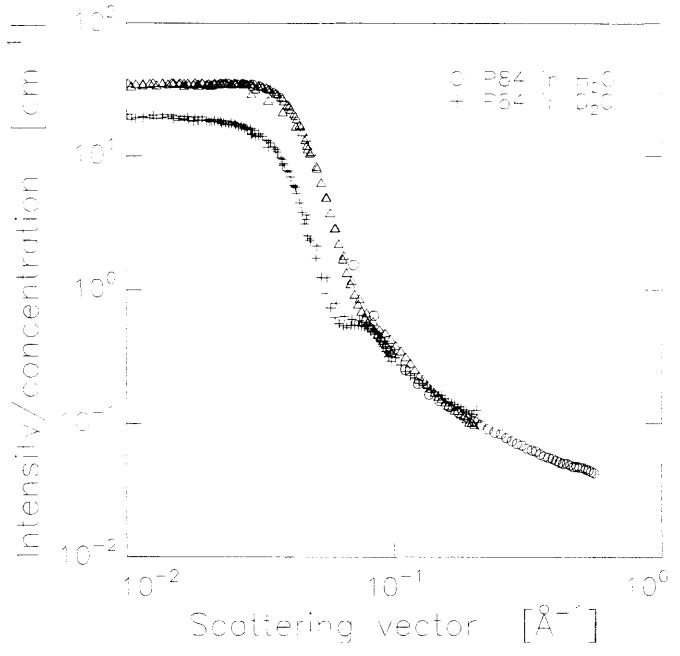

Figure 39 Experimental scattering data of PEO-PPO-PEO spherical micelles in mixture of water and oil. The data labeled H_2O corresponds to bulk contrast, while the data labeled D_2O have shell-contrast (see Figure 3). The solid lines are best fits to core and shell model.

This form factor can be generalized to the form factor of N concentric shells with radii R_i and ρ_i being their respective scattering length densities:

$$P(q) = \frac{\rho_1 V(R_1) P_{\text{sphere}}(q, R_1) + \sum(\rho_i - \rho_{i-1}) V(R_i) P_{\text{sphere}}(q, R_i)}{\rho_1 V(R_1) + \sum V(R_i)(\rho_i - \rho_{i-1})} \tag{125}$$

The solid lines in Figure 39 represents least square fits to this core and shell model.

The typical block copolymer micelles are characterized by not having dense shell structure, however. The polymers in the corona form rather a brush-like structure. The scattering function of such micelles does accordingly not show the high-q q^{-4}-law, since $I(q)$ in this range reflects local chain properties inside the corona. The form factor of such block copolymer micelles approach rather the q^{-2} behavior reflecting the polymer coil conformation (see equation 36).

A more realistic form factor of such spherical block-copolymer micelles should account for self-correlation of the spherical core, self-correlation of the chains in the corona, and cross term between the core and chains as well as between different chains. Pedersen and coworkers constructed an analytically scattering function that fulfils these criteria [139].

The self-correlation term of the sphere (P_{sp} and Φ_{sp}) and chains (P_{ch}) are given by the formula equation (123) and equation (38), respectively. The cross terms are calculated using the Debye equation, assuming infinitely thin shells and taken into account the correct weighting functions for, respectively, solid sphere and Gaussian chains. The interference term between core and chains thereby get the form:

$$S_{sc}(q) = \Phi_{sp}(q, R_c) x^{-1}(1 - e^{-x}) \sin(qR_c)/(qR_c) \tag{126}$$

and the term between chains attached to the surface:

$$S_{cc}(q) = x^{-2}(1 - e^{-x})^2 \left[\sin(qR_c)/(qR_c)\right]^2 \tag{127}$$

with $x = (R_g q)^2$, as before. The resulting form factor of a block-copolymer micelle with aggregation number N_{agg} can then be expressed as [139]

$$\begin{aligned} P_{mic}(q) =& N_{agg}^2 \rho_s^2 P_{sp}(q, R) + N_{agg} \rho_c^2 P_{ch}(q, L, b) \\ &+ N_{agg}(N_{agg} - 1) \rho_c^2 S_{cc}(q) \\ &+ 2 N_{agg} \rho_s \rho_c S_{sc}(q) \end{aligned} \tag{128}$$

where ρ_s and ρ_c are the excess scattering length densities of blocks in the core and in the chains of the corona, respectively.

Fits applying this micellar form factor gives very good agreement with experimental scattering data, as shown for PEO-PPO-PEO block copolymer micelles in Figure 40 [140]. The solid lines represents least square fits including instrumental smearing. The fit to the 1% polymer concentration represents effectively the bare form factor

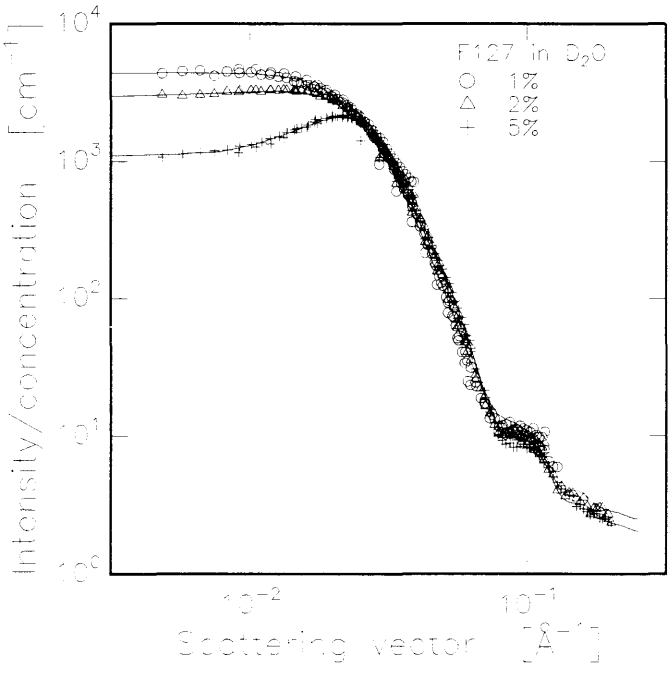

Figure 40 Experimental scattering data of spherical micelles of 1%, 2% and 5% aqueous (D_2O) solutions of $EO_{99}PO_{65}EO_{99}$-triblock copolymers. The solid lines are best fits to the micellar form factor equation (128), including hard-sphere interaction, equation (129), and instrumental resolution (from Mortensen and Talmon, *Macromolecules*, **1995**; 28: 8829).

equation (128), while the higher concentrations are affected by inter micellar correlations, as discussed further below. This inter micellar correlation mainly affects the low-q part of the spectra.

The position of the high-q side maximum (at $q \sim 10^{-1}$Å^{-1} in the system shown in Figure 40) gives directly the micellar size. It appears thus from the system shown, that the size and thereby the aggregation number does not change within the concentration range given in the figure.

9.2 Inter Micellar Correlations

The scattering function of micellar solutions becomes increasingly dominated by the structure factor, $S(q)$, as the micellar concentration is increased. In non-ionic suspensions of spherical, or near spherical micelles, the structure factor can successfully be determined using the Ornstein-Zernike approximation and applying the Percus-Yevick closure [141] with a hard-sphere interaction potential. $S(q)$ is in this hard-sphere Percus-Yevick approximation given by only two parameters, the micellar volume fraction ϕ and the hard-sphere interaction distance R_{hs} [142–144]:

$$S(q) = \frac{1}{1 + 24\phi G(qR_{hs}, \phi)/(2qR_{hs})} \tag{129}$$

where G is a trigonometric function of qR_{hs} and ϕ

$$\begin{aligned} G(qR_{hs}, \phi) = {} & \alpha(\phi)/4(qR_{hs})^2 \cdot [\sin(2qR_{hs}) - 2qR_{hs}\cos(2qR_{hs})] + \\ & \beta(\phi)/8(qR_{hs})^3 \cdot [4qR_{hs}\sin(2qR_{hs} + (2 - 4(qR_{hs})2) \\ & \cos(2qR_{hs} - 2] + \\ & \gamma(\phi)/32(qR_{hs})^5 \cdot [-16(qR_{hs})^4\cos(2qR_{hs}) + \\ & 4[(8(qR_{hs})^2 - 6)\cos(2qR_{hs}) + (8(qR_{hs})^3 - 12qR_{hs}) \\ & \sin(2qR_{hs}) + 6]] \end{aligned} \tag{130}$$

where α, β, and γ are given by the hard sphere volume fraction ϕ:

$$\alpha = (1 + 2\phi)^2/(1 - \phi)^4$$

$$\beta = -6\phi \cdot (1 + \phi/2)^2/(1 - \phi)^4$$

$$\gamma = \phi/2 \cdot (1 + 2\phi)^2/(1 - \phi)^4$$

The peak-position q_{max} of $I(q)$ of hard-sphere systems are frequently interpreted simple as given by the mean micellar distance: $2\pi/q_{max} = D = [4\pi/3R_{hs}^3/\phi]^{1/3}$, i.e., given by the micellar number density only. This is not true, the position of q_{max} is determined by a complex function of both R_{hs} and ϕ.

It is important to note, that in spite of the dispersed polymer corona a near-hard sphere interaction potential is expected as a result of entropic repulsion.

For suspensions of charged spherical micelles, the Ornstein-Zernike approximation has also been successfully applied, but with other closure relations than the hard sphere Percus-Yevick. Two closures are often used, the hypernetted chain approximation (HNCA) and the mean spherical approximation (MSA). The HNCA is known to be quite accurate for a charged hard-sphere system, however, it is a non-linear theory, which has to be solved by numerical methods. On the other hand, the MSA method is a linearized version of the HNCA. It is somewhat less accurate, but has the great advantage of having an analytical solution when the potential function is of the Yukawa form or screened Coulomb form [145]. Since the pioneering work of Hayter and Penfold [146] it has been customary in SANS data treatment to use the Derjaguin-Landau-Verwey-Overbeek (DLVO) double-layer repulsive potential as the interaction potential in the MSA.

With data obtained systematic as a function of polymer concentration, temperature and possibly pressure, is it possibly to give thermodynamic details on the aggregation behavior and inter micellar interactions. Fits to the experimental scattering data, as the examples presented in Figure 40, give essential four parameters: the micellar volume fraction, the micellar core and interaction radii and the aggregation number.

As a good model system, we will present some illustrative data of poly (ethylene oxide)-poly(propyleneoxide)-poly(ethyleneoxide), PEO-PPO-PEO, triblock copolymers in aqueous solution. The amphiphilic character of these copolymers changes dramatic with temperature, since the PPO block changes from being hydrophilic to hydrophobic upon raising temperature.

9.2.1 Critical Micellar Values and Micellar Volume Fraction

One of the important parameters obtained from fits to the experimental scattering function is the micellar volume fraction, ϕ.

Figure 41 shows in a contour diagram the micellar volume fraction ϕ of an aqueous suspension of EO_{25}-$PO_{40}EO_{25}$ triblock copolymers, given as a function of polymer concentration c and temperature T. The micelles are spherical in the given regime [92, 144].

At low temperatures and concentrations (regime I in the figure), all polymers are dissolved as *unimers*, i.e., as individual copolymer chains. Above a line of critical micellation temperatures (T_{cm1}) and concentrations (cmc_1), a relative broad regime (II) appear where unimers and spherical micelles coexist thermodynamically. The micellar volume fraction increases roughly linearly with temperature in this regime and reaches above a second characteristic temperature, T_{cm2}, a constant value, ϕ_0, corresponding to the situation that effectively all copolymers belong to a micellar aggregate. The boundaries separating phase I and II, and phase II and III are both well defined and reversible.

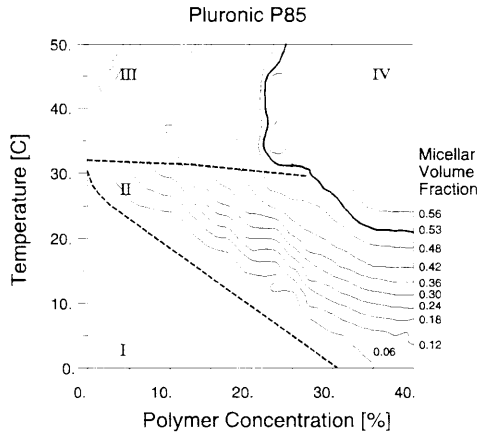

Figure 41 Contour plot of the micellar volume fraction of the $EO_{25}PO_{40}EO_{25}$ system as a function of polymer concentration and temperature. The broken lines separate pure unimer phase (I), pure spherical micellar phase (III) and coexisting micellar and unimer phase (II). The solid line represents $\phi = 0.53$ and separates liquid and *para*-crystalline phase (IV). (reproduced from Mortensen, *J. Physics Cond. Matter*, **1996**; 8: A103).

For polymer concentrations below approximately 20%, the limiting value of ϕ, that is approached in regime III, varies linearly with concentration [147] for $c \leq 0.2$. Above $c \approx 20\%$, on the other hand, the micellar volume fraction reaches a constant of the order of $\phi_c = 0.53$ (IV). In this regime there will therefore remain some unimers present. The $\phi_c = 0.53$ border is accompanied with a liquid-to-solid phase transition, reflecting that the suspension in regime IV forms a cubic ordered micellar crystal [147, 148], in agreement with the theoretical $\phi_c = 0.53$ value of hard-sphere crystallization [151].

In fitting the scattering function using equation (128), the aggregation number N and the volume fraction ϕ are two independent parameters. These are, however, coupled, *via* a third parameter R_{hs}. In the regime where ϕ increases linearly with temperature, the system is thermodynamic stable with both micelles and polymers present. The number of micelles per volume, ϕ/V_{hs}, ($V_{hs} = 4\pi/3R_{hs}^3$ being the hard-sphere micelle volume) and the number of free chains per volume, n_p, is related through

$$n_p + N_{agg} \cdot \phi/V_{hs} = c/V_p \qquad (131)$$

where c/V_p represents the total concentration of polymer chains, V_p being the dry volume of the polymer. Above T_{cm2} there are effectively no free polymer chains, i.e., $n_p = 0$, thus giving aggregation number:

$$N_{agg} = c/\phi_o \cdot 4\pi R_{hs}^3/3V_p. \qquad (132)$$

The dry polymer volume is given as the sum of the volume of monomers, $V_p = 2mV_{EO} + nV_{PO}$, where $V_i = M_i/(\rho_i N_A)$, i = *PO* or EO.

Application of pressure can, in analogy with the presentation on polymer blends section 7 and block copolymer melts, section 8, be used as an additional thermodynamic variable that leads to extended understanding. For the aqueous PEO-PPO-PEO systems, pressure has the effect of improving the solvent quality of water for PPO, i.e., the micelles tend to dissolve into unimers. The resulting effect on phase boundaries, critical micellation and micellar ordering temperature, is in agreement with the thermodynamic Clausius-Clapeyron equation (75) $\Delta T/\Delta P = \Delta V/\Delta S$ [149].

9.2.2 Micellar Sizes

In fitting the scattering function using equations (128) and (129), the micellar core size and interaction distance are among the resulting parameters.

Figure 42 shows such resulting core radii for PEO-PPO-PEO block copolymer micelles, given as a function of both temperature, concentration and molecular design [150]. The series of block copolymers shown in the figure have similar size PPO block: $EO_{25}PO_{40}EO_{25}$, $EO_{65}EO_{39}EO_{65}$ and $EO_{96}PO_{39}EO96$.

The micellar radius for different PEO/PPO architectures shows very similar characteristics. The scattering results show significant changes in core size with temperature, reflecting that the micelles are dynamic aggregates where the individual copolymer chains on short time scale jump from one micelle to another. It appears that when R_c is plotted against the reduced temperature $T - T_{cm1}$, the data follow a common master curve with the empirical scaling relation:

$$R_c \propto (T - T_{cm1})^{0.2} \qquad (133)$$

9.2.3 Ellipsoidal and Rod-like Micelle

There is no simple analytical form, which in analogy with equation (123) for spherical objects, can describe the

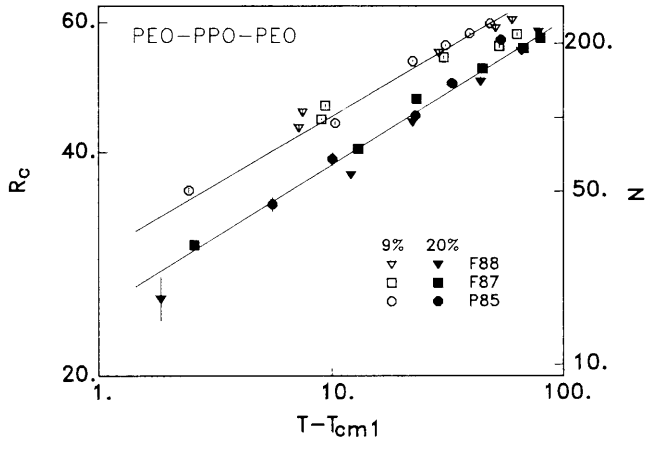

Figure 42 The micellar core radius of various PEO-PPO-PEO block copolymer micelles plotted versus the relative temperature, $T - T_{cm1}$, T_{cm1} being the critical micellation temperature. (reproduced from Mortensen and Brown, *Macromolecules*, **1993**; 26: 4128).

form factor of micelles with ellipsoidal or rod-like form. The form factor can in such cases be given in the form of numerical integrations.

For an ellipsoid with two of the axes equal R and the third axis equal ϵR, the form factor is given as [6]

$$P(q) = \int_0^{\pi/2} \left[\frac{3(\sin(q\tilde{R}) - q\tilde{R}\cos(q\tilde{R})}{(q\tilde{R})^3} \right] \sin\alpha \, d\alpha \qquad (134)$$

with $\tilde{R}(\alpha) = R(\cos^2\alpha + \varepsilon^2 \sin^2\alpha)^{1/2}$.

The form factor for concentric ellipsoidal shells can be calculated in analogy to that of concentric spheres, equation (125).

The form factor expression for rod-like micelles involves an integration over the first order Bessel function $B_1(x)$. For rods with radius R and length L has $P(q)$ the form [6]

$$P(q) = \int_0^{\pi/2} \left[\frac{2B_1(qR\sin(\alpha))}{qR\sin(\alpha)} \cdot \frac{\sin(\frac{1}{2}qL\cos(\alpha))}{\frac{1}{2}qL\cos(\alpha)} \right]^2 \cdot \sin(\alpha) d\alpha \qquad (135)$$

Equivalently, expressions has been developed for other relative simple geometries, as for example cylinder-shaped particles with elliptical cross section [152], and cylinders with spherical end-caps [153]. Extended flexible, polymer-like micelles have recently attracted lots of interests. The scattering function of such micelles has been studied both theoretically and experimentally (see e.g., [154]).

9.3 Nematic Phase

Rod-like and other extended micellar structures might show interesting response when exposed to shear.

Figure 43 shows the shear dependence of a 10% solution of $EO_{25}PO_{40}EO_{25}$ as obtained approximately in the middle of the rod-phase, $T = 76\,^{\circ}C$. It is clear that the micelles align in the shear field, forming a nematic phase.

The degree of alignment can be quantified by the nematic order parameter P_2:

$$P_2 = \frac{1}{2}\langle 3\cos(\phi) - 1 \rangle \qquad (136)$$

The order parameter corresponding to the two-dimensional data given in Figure 43 is given in Figure 44. The order parameter increases monotonically for shear fields up to about $\dot{\gamma} \simeq 1000\,s^{-1}$, beyond which value it stays constant.

The anisotropic scattering pattern of the sample displayed in the Figures 43 and 44, relaxes back to an azimuthally isotropic structure when the shear is stopped on a time scale that is far to quick too be studied by neutron scattering. In the neutron scattering experiment we observe isotropic scattering within the time resolution of a few seconds after the shear has been stopped.

9.4 Swollen Lamellar Phases

The block copolymer micellar systems form a variety on ordered mesophases in analogy with both the block copolymer melts discussed in section 8, and in ordinary surfactant systems. The scattering experiments of such micellar mesophases follow to a large extend the lines discussed above concerning ordered block copolymer melts. This also include shear alignment into mono-domain ordered crystals, etc. We will therefore not discuss the scattering technique on these phases further, but only rather briefly mention swollen phases, i.e., ordered phases where the solvent (or other homo-polymers) swell the ordered structure. We will in particular discuss the swollen lamellar phase.

Many block copolymers form lamellar mesophases when mixed with selective solvents. In aqueous PEO-PPO-PEO systems with low content of the hydrophobic block PEO, as the $EO_6PO_{36}EO_6$-copolymer, the lamellar phase is stable already at low (10% or less) polymer concentration [155]. The scattering function of such lamellar phases are usually dominated by a strong first order correlation peak, but only weak or no higher

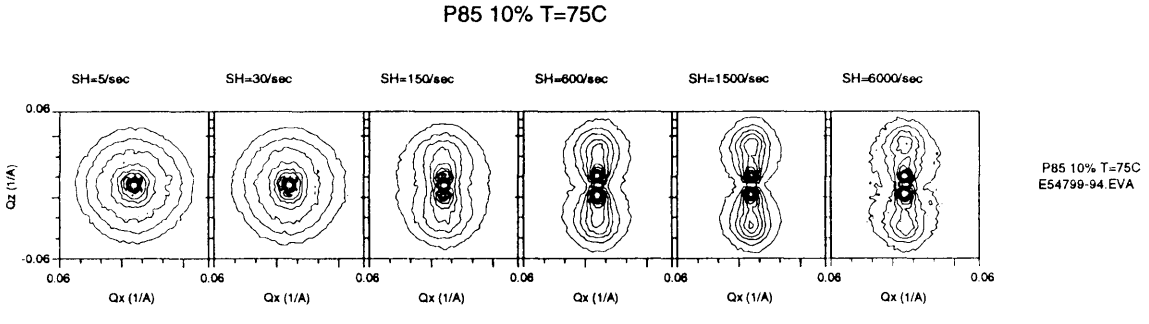

Figure 43 Two-dimensional scattering pattern of a 10% aqueous solutions of $EO_{25}PO_{40}EO_{25}$ in the rod-phase, as a function of external shear rate.

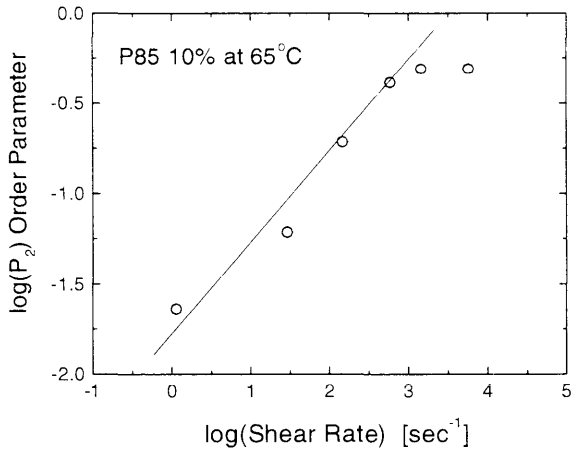

Figure 44 Nematic order parameter P_2 of a 10% aqueous solutions of $EO_{25}PO_{40}EO_{25}$ in the rod-phase, as a function of external shear rate. The order parameter is calculated based on the data shown in Figure 43.

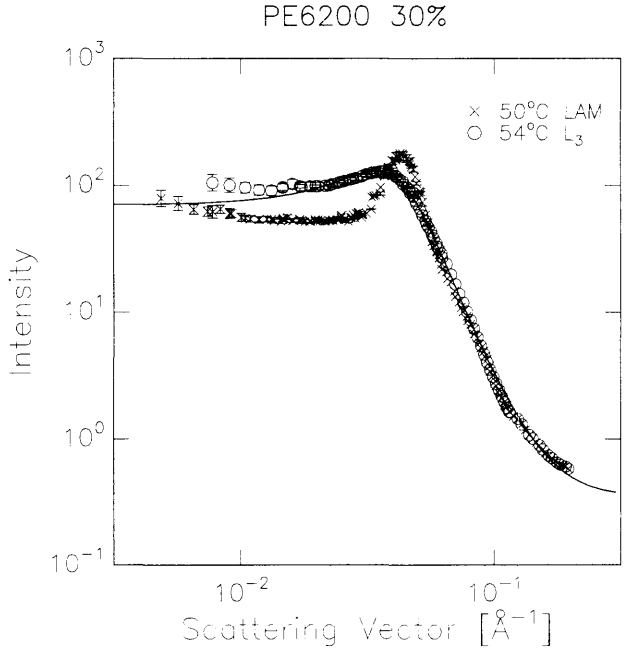

Figure 45 Scattering function of 30% $EO_6PO_{36}EO_6$ aqueous solution in the lamellar LAM-phase and in the bi-continuous L_3-phase. The solid line through the L_3-data points represents best fit to the Teubner-Strey model.

order reflections, as that shown in Figure 45, giving data of a 30% aqueous $EO_6PO_{36}EO_6$ solution.

The low-q scattering is typical for swollen lamellar phases with significant in-plane fluctuations. The lamellar periodicity, d, increases linearly with polymer concentration c:

$$d \propto \delta/c \tag{137}$$

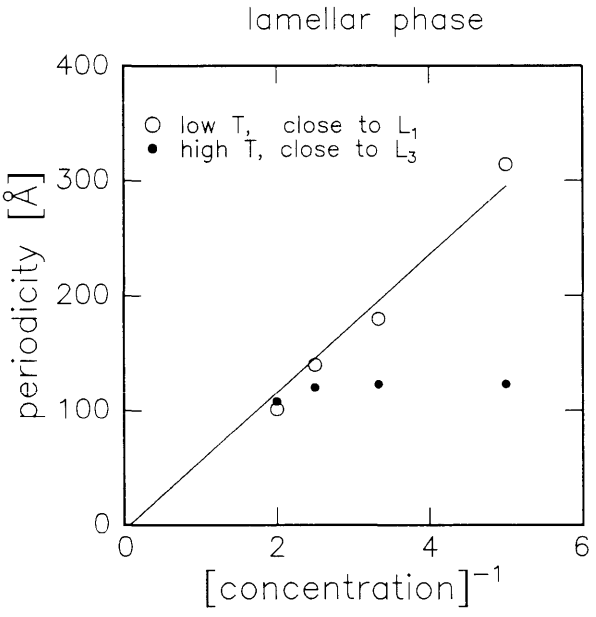

Figure 46 Periodicity of swollen lamellaes. Near the L_1-phase, the swelling follows simple geometric expectations (equation 137), while near the L_3-phase, fluctuations in the lamellaes stabilizes a periodicity roughly independent of c.

as expected for ideal one dimensional swelling. The prefactor δ gives the effective block copolymer thickness. An experimental example of this is given in Figure 46, showing the swelling of the lamellar phase both near the boundary to the micellar L_1-phase, and near the boundary to the bicontinuous L_3-phase. The simple geometric swelling-rule is perfectly fulfilled near the L_1-phase, whereas in-plane fluctuations near the L_3-phase stabilize a periodicity that is almost concentration independent.

The highly swollen lamellar systems is characterized by absence of really perfect, long-range order crystallinity. There exists different approached to describe such structure factors. In the classical work of Caillé, calculated for liquid crystalline smectic phases based on de Gennes harmonic description of the free energy given, the n'th order Bragg-reflection is given as [156]:

$$S(q_z)_n = \left[q_z - (2\pi n/d)\right]^{-2+\eta(n)} \tag{138}$$

with the characteristic power-law profile with exponent $\eta(n)$ given by the lamellae bending modulus K and bulk modulus B:

$$\eta(n) = \left[\pi/(2d^2)\right] \cdot \left[k_B T/\sqrt{KB}\right] n^2 \tag{139}$$

The power-law profile has been experimentally verified in smectic liquid crystalline materials.

Alternative approaches to describe the swollen lamellae phase is based on *para*-crystalline theory, where the scattering function must be calculated as a

convolution of the lamellar form factor and a one-dimensional lamellar structure factor $S_1(q)$ [157, 158]:

$$S(q_z) = < |f(q)|^2 S_1(q) > \quad (140)$$

9.5 Bicontinuous Microemulsions

While bicontinuous microemulsions frequently appear in ternary systems of oil, water and a low molar mass surfactant, this phase is still relative unexplored for polymeric systems. Polymeric bicontinuous microemulsions have only been seen in a low PEO-content aqueous system of PEO-PPO-PEO [155], and in mixtures of homo-polymers and block copolymers [160, 159]. In Figure 45 is shown the scattering function of the aqueous PEO-PPO-PEO system both in the lamellar phase ($T = 50\,^{\circ}C$) as discussed above, and when in the bicontinuous L_3-phase ($T = 54\,^{\circ}C$).

Based on three component oil/water/surfactant systems, Auvray and coworkers found empirically that the structure factor of the L_3 bi-continuous phase is characterized by a peak at the q-position [161]

$$q^* = \alpha \Delta^{-1} [\phi_s/(\phi_w \phi_o)] \quad (141)$$

with the prefactor α close to 0.5, and where ϕ_s, ϕ_w and ϕ_o are the volume fraction of respectively surfactants, water and oil, and $\Delta = \nu_s/a_H$ is the ratio between the steric volume of the surfactant molecule, ν_s, and the head-area, a_H.

Based on Debye's theory for a two-component material [162], different expressions have been developed which can be applied in either the bulk contrast case [163] or interface contrast [164, 165] (see Figure 4 in section 2). In the Teubner and Strey model the two phases are characterized by the volume fractions ϕ'_A and ϕ'_B modified from the original 'water' and 'oil' numbers by including the heads of the surfactant molecules in the water phase, and tails in the oil-phase. In the block-copolymer/polymer case this corresponds to respectively A-polymers and A-like solvent, and B-polymers and B-like solvent. The Teubner-Strey correlation function $\gamma(\mathbf{r})$ is given as

$$\gamma_{TS} = \exp(-r/\xi) \cdot j_o(q_o r) \quad (142)$$

where $q_o = 2\pi/d$, d being the average inter-domain distance between the two phases, and $\xi/d = q_o \xi/2\pi$ is a measure of polydispersity of the domain size. Inserting this γ_{TS}-correlation function into the expression for the scattering function gives

$$I(q) = 8\pi^2 \langle \eta \rangle / [\xi(q_a^2 - 2q_m^2 q^2 + q^4] \quad (143)$$

where $q_a^2 = q_o^2 + 1/\xi^2$ and $q_m^2 = q_o^2 - 1/\xi^2$. The scattering function $I(q)$ exhibits a peak at $q = q_m$ when $q_o > 1$, as shown in the example given in Figure 45. From the general property of the Debye function one obtain:

$$\gamma(r = 0) = -\xi^{-1} = -[1/(4\phi_{A'}\phi_{B'}] \cdot (S/V) \quad (144)$$

where S is the total internal interface and V the volume. Assuming that all surfactant molecules are on the oil-water interface, each subtending an area a_H, we have $S/V = \phi_s/\Delta$ and thus the relation between ξ and the system composition:

$$\xi = 4\Delta \cdot \phi_{A'} \cdot \phi_{B'}/\phi_{AB} \quad (145)$$

The solid line shown in Figure 45 represents best fit to the data in the L_3-phase, using the Teubner-Strey model.

Berk [164] and Chen *et al.* [165, 166] have applied the two-phase Debye correlation function in the case of interface contrast, where only the surfactant tails are visible. The main difference from the bulk contrast is the definition of the two phases, and their major difference in size: $\phi_1 = \phi_{w'+o}$ is the sum of the water-, the oil- and the surfactant head-group phases; and $\phi_2 = \phi_{s'}$ is the volume fraction of the tails. In the Berk-Chen model, the correlation function is given as [165].

$$\gamma_{BC} = 2/\pi \sin^{-1} [\tau(r, q_o)] + \sum C_n [\tau(r, q_o)]^n \quad (146)$$

where the coefficients C_n is given as Hermite-potentials. The Bessel function $j_o(r)$ in Berk's original model is smeared through a Schultz distribution f_Z of order Z in the attempt to approach experimental observations of relative broad peak in $I(q)$:

$$\begin{aligned} \tau(r, q) &= \int j_o(r) f_Z(q) dq \\ &= [(Z+1)/(qr)] \cos^Z(\phi) [\sin(Z\phi)/Z] \end{aligned} \quad (147)$$

with $\phi = \tan^{-1} [kr/(Z+1)]$. Substituting the above equation into the scattering function gives the scattering intensity.

9.6 Block Copolymer Micellar Networks

While the ABA-kind of block copolymers form individual micelles which interact through hard-sphere like repulsions, quite different behavior can be expected for BAB-kind of aggregates, as schematically illustrated in Figure 38.

The BAB-micellar systems have potentially interesting elastic properties as a result of the network structure. Very well defined networks can be designed with controllable sizes of both the rubber-like middle blocks and the knots formed by the micellar cores. One may even be able to control the position of the knots since these can be organized on a crystalline lattice [167].

In triblock copolymer systems of crystalline or glass forming polymers, permanent stable networks are

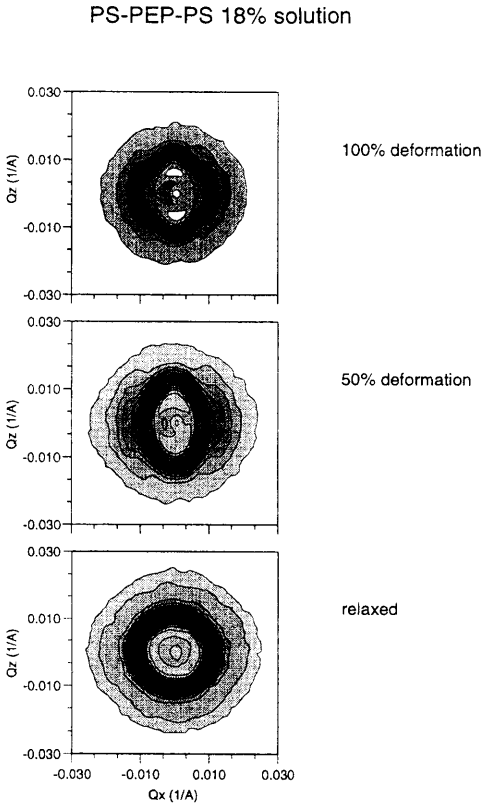

Figure 47 Two-dimensional scattering function of micellar network of PS-PEP-PS triblock copolymers in oil, as obtained when stretched to various degree (reference Mortensen, *Current Opinion Coll. Int. Sci.*, **1998**; 3: 12).

possibly. Tri-block copolymers of polystyrene, PS, and rubber like materials like poly(ethylene propylene), PEP, form such stable networks when dissolved in oil. Already with a few percent of such polymers in the oil, a permanent network of interconnected glassy PS spheres is formed throughout the sample, resulting in rubber-like elastic material. In some parts of the phase diagram, these materials form solid like ordered structures in analogy with the independent bulk copolymers and AB (A)-micelles.

Stretching these materials gives rise to interesting structures, as shown in the contour plot of Figure 47 [168, 169]. The scattering pattern of samples stretched up to roughly 100% shows markedly enhanced scattering intensity in specific positions: *pseudo Bragg reflections* revealing stretching induced positional order of the PS-cores. At higher stretching ratios butterfly shaped patterns appear reflecting major inhomogeneity in the distribution of micellar links.

10 Concluding Remarks

In the present review we have described the use of small-angle neutron scattering to study a variety of polymer systems, including polymer chain conformation, phase behavior of polymer blends and block copolymers, micellar phases, and critical scattering near phase transitions.

It has been shown that the small-angle scattering technique can provide detailed experimental values of size and form of polymers chains as well as their aggregates, and the technique gives detailed knowledge to the thermodynamics.

Still, a large number of features, which are also studied by neutron scattering techniques, have not been included. This concerns for example studies on stretched networks to elucidate properties related to the so-called tube of the polymer dynamics, and it concern more complex structures, like star-polymers, dendrimers and multi-branched chain structures. Crystalline and semi-crystalline polymer systems, as often studied by combined small-angle and wide angle scattering have also, due to limitations, been excluded in the review, as well as topics related to near-surface structures, as studied by neutron and x-ray reflectivity.

It appear from the text, that the information obtained from scattering experiments can be used directly in the design and optimization of new polymeric materials. But experimental scattering studies of complex polymer systems provides also a big challenge for exploring new physical phenomena.

Acknowledgments

The present review on scattering methods in polymer physics is based on long standing collaboration with a number of colleagues and students, of whom I in particular would like to acknowledge Schwahn, D., Bates, F.S., Stamm, M., Almdal, K., Pedersen, J.S., Vigild, M. and Papadakis, C.

References

1. Higgins, J.S. and Benoît, H. *Polymers and Neutron Scattering*, Clarendon Press, Oxford, **1994**.
2. Strobl. G. *The Physics of Polymers*, Springer, Berlin, **1996**.
3. Chen, S.-H. and Kotlarchyk, M. *Interaction of Photons and Neutrons with Matter*, World Scientific Pub. Co., Singapore, **1997**.
4. Lindner, P. and Temb. T. *Neutron, x-ray and light scattering*, North Holland, Amsterdam, **1991**.
5. Brown, W. and Mortensen K. (Ed.) *Scattering in Polymeric and Colloidal Systems*, Gordon and Breach Sci. Publ., **2000**.
6. Guinier, A. and Fournet. G. *Small-angle scattering of x-rays*, J. Willey and Sons, New York, **1955**.
7. Glatter, O. and Kratky, O. (Ed.) *Small-angle x-rays scattering*, Academic Press, New York, **1982**.
8. Wignal, G. and Bates, F.S. *J. Appl. Cryst.*, **1987**; 20: 28.
9. Jacrot, B. and Zaccai. G. *Biopolymers*, **1981**; 20: 2413.
10. Kotlarchyk, M. and Chen. S.-H., *J. Chem. Phys.*, **1983**; 79: 2461.
11. Pedersen, J.S. *J. Appl. Cryst.*, **1994**; 27: 595.
12. Pedersen, J.S., Posselt, D. and Mortensen. K. *J. Appl. Cryst.*, **1990**; 23: 321.

13. Glatter, O. *J. Appl. Cryst.*, **1997**; 10: 415.
14. Hansen, S. and Pedersen. J.S. *J. Appl. Cryst.*, **1991**; 24: 541.
15. deGennes. P.G. *Scaling Concepts in Polymer Physics.* Cornell Univ. Press, Ithaca, **1979**.
16. Mortensen, K. and Pedersen. J.S. *Macromolecules*, **1993**; 26: 805.
17. Kiste, R.G. *et al., Die Macromol. Chemie*, **1969**; 121: 174.
18. Ballard, D.G.H. *et al., Polymer*, **1976**; 17: 349.
19. Miyaki, Y. *et al., Macromolecules*, **1987**; 11: 1180.
20. Huber, K. *et al., Macromolecules*, **1985**; 18: 1461.
21. Falcao, A., Pedersen, J.S. and Mortensen, K.B. *Macromolecules*, **1993**; 26: 5350.
22. Brown, W. and Mortensen, K. *Macromolecules*, **1988**; 21: 420.
23. Bastides, J., Picot, C. and Candau, S.J. *J. Macromol. Sci.*, **1981**; B19: 13.
24. Texeira, J. *J. Appl. Cyst.*, **1988**; 21: 781.
25. Ginzburg, V.L. *Sov. Phys., Sol. State*, **1960**; 2: 1824.
26. Goldenfeld, N. Lectures on Phase Transitions and the Renormalization Group. In *Frontiers in Physics 85*, Addison-Wesley, New York, **1992**.
27. Schwahn, D., Mortensen, K. and Yee-Madeira, H. *Phys. Rev. Lett.*, **1987**; 26: 1544.
28. Bates, F.S., Rosedale, J., Stepanek, P., Lodge, T.P., Wiltzius, P., Fredrickson, G.H. and Hjelm. R.P. *Phys. Rev. Lett.*, **1990**; 65: 1893.
29. Janssen, S., Schwahn, D., Mortensen, K. and Springer, T. *Macromolecules*, **1993**; 26: 5587.
30. Brereton, M.B., Fischer, E.W., Herkt-Maetzky, C. and Mortensen. K. *J. Chem. Phys.*, **1987**; 58: 6144.
31. Schwahn, D. and Mortensen, K. Polymer blends. In *Scattering in Polymeric and Colloidal Systems*, Brown W. and Mortensen K. (Ed.) Gordon and Breach Sci. Publ., **2000**.
32. Müller, G., Schwahn, D., Eckerlebe, H., Rieger, J. and Springer. T. *J. Chem. Phys.*, **1996**; 104: 5326.
33. Binder, K. Phase Transitions in Polymer Blends and Block Copolymer Melts: Some Recent Developments. In *Advances in Polymer Science*, Springer-Verlag, Berlin, **1994**; 112: 181.
34. Binder, K. *Phys. Rev.*, **1984**; A29: 341.
35. Müller, G., Schwahn, D., Eckerlebe, H., Rieger, J. and Springer, T. *J. Chem. Phys.*, **1996**; 104: 5326.
36. Schwahn, C., Mortensen, K., Springer, T., Yee-Madeira, H. and Thomas, R. *J. Chem. Phys.*, **1987**; 87: 6078.
37. Belyakov, M.Y. and Kiselev, S.B. *Physica A*, **1992**; 190: 75.
38. Anisimov, M.A., Kiselev, S.B., Sengers, J.V. and Tang, S. *Physica*, **1992**; 88: A1, 487.
39. Schwahn, D., Meier, G., Mortensen, K. and Janssen, S. *J. Phys. II (France)*, **1994**; 4: 837.
40. de Gennes, P.G. *J. Physique Lett.*, **1977**; 38: 441.
41. Janssen, S., Schwahn. D. and Springer. T. *Phys. Rev. Lett.*, **1992**; 68: 3180.
42. Frielinghaus, H., Schwahn, D., Mortensen, K., Willner, L. and Almdal, K. *J. Appl. Cryst.*, **1997**; 30: 696.
43. Schwahn, D., Mortensen, K. and Janssen, S. *Phys. Rev. Lett.*, **1994**; 73: 1452.
44. Binder, K. *J. Chem. Phys.*, **1983**; 72: 4756.
45. Schwahn, D., Schmackers, T. and Mortensen, K. *Phys. Rev.*, **1994**; E52: 1452.
46. Hobbie, E.K., Nakatani, A.I. and Han, C.C. *Mod. Phys. Lett.*, **1994**; B8: 1143.
47. Onuki, A. and Kawasaki, K. *Ann. Phys.*, **1979**; 121: 456.
48. Onuki, A. and Kawasaki, K. *Ann. Phys. Suppl.*, **1981**; 131: 271.
49. Beysend, D., Gbadamassi, M. and Boyer, L. *Phys. Rev. Lett.*, **1979**; 43: 1253.
50. Takebe, T., Sawaoka, R. and Hashimoto, T, *J. Chem. Phys.*, **1989**; 91: 4369.
51. Hobbie, E.K., Hair, D.W., Nakatani, A.I. and Han, C.C. *Phys. Rev. Lett.*, **1992**; 69: 1951.
52. Hobbie, E.K., Nakatani, A.I., Yajima, H., Douglas, J.F. and Han, C.C. *Physical Review E*, **1996**; 53: R4322.
53. Bates, F.S. and Fredrickson, G.H. *Annu. Rev. Phys. Chem.*, **1990**; 41: 525.
54. Bates, F.S. and Fredrickson, G.H. *Annu. Rev. Mater. Sci.*, **1996**; 26: 501.
55. Bates, F.S., Schulz, M.F., Khandpur, A.K., Förster, S., Rosedale, J.H., Almdal, K. and Mortensen, K. *Faraday Discuss*, **1994**; 98: 7.
56. Meier, D. *J. Polym. Science*, **1968**; C26: 81.
57. Hashimoto, T., Shibayama, M., Kawai, H. and Meier, D. *Macromolecules*, **1985**; 18: 1844.
58. Helfand, E. *J. Chem. Phys.*, **1975**; 62: 999.
59. Helfand, E. *Macromolecules*, **1975**; 8: 552.
60. Leibler, L. *Macromolecules*, **1980**; 13: 1602.
61. Fredrickson, G.H. and Helfand, E. *J. Chem. Phys.*, **1987**; 87: 697.
62. Matsen, M.W. and Schick, M. *Macromolecules*, **1994**; 27: 4014.
63. deGennes, P.G., *J. Physique (France)*, **1970**; 31: 235.
64. Vavasour, J.D. and Whitemore, M.D. *Macromolecules*, **1993**; 26: 7070.
65. Benoit, H., Wu, W., Benmouna, M., Mozer, B., Bauer, B. and Lapp, A. *Macromolecules*, **1985**; 18: 986.
66. Brazovskii, S.A. *Sov. Phys. JETP*, **1975**; 41: 85.
67. Various alternative names are used for the three regimes of segregation, e.g. *weak, intermediate* and *strong*.
68. Matsen, M.W. and Bates, F.S., *Macromolecules*, **1996**; 29: 1091.
69. Almdal, K., Rosedal, J.H., Bates, F.S., Wignall, G.D. and Fredrickson, G.H. *Phys. Rev. Lett.*, **1990**; 65: 1112.
70. Fried, H. and Binder, K. *Europhys. Lett.*, **1991**; 16: 237.
71. Barrat, J.L. and Fredrickson, G.H. *J. Chem. Phys.*, **1991**; 95: 1281.
72. Sones, R.A., Terentjev, E.M. and Petschek, R.G. *Macromolecules*, **1993**; 26: 3344.
73. Melenkevitz, J. and Muthukumar, M. *Macromolecules*, **1991**; 24: 4199.
74. Shull, K.R. *Macromolecules*, **1992**; 25: 2122.
75. Vavasour, J.D. and Whitmore, M.D. *Macromolecules*, **1992**; 25: 5477.
76. Tang, H. and Freed, K.F. *J. Chem. Phys.*, **1992**; 96: 621.
77. McMullen, W.E. *Macromolecules*, **1993**; 26: 1027.
78. Mayes, A.M. and de la Cruz, M.O. *J. Chem. Phys.*, **1991**; 95: 4670.
79. Papadakis, C.M., Almdal, K., Mortensen, K. and Posselt, D. *Europhys. Lett.*, **1996**; 36: 289.
80. Papadakis, C.M., Almdal, K., Mortensen, K. and Posselt, D. *J. Phys. II France*, **1997**; 7: 1829.
81. Hadziioannou, G. and Skoulios, A. *Macromolecules*, **1982**; 15: 258.
82. Hasegawa, H., Hashimoto, T., Kawai, H., Lodge, T.P., Amis, E., Glinka, C. and Han, C.C. *Macromolecules*, **1985**; 18: 67.
83. Hashimoto, T., Shibayama, M. and Kawai, H. *Macromolecules*, **1980**; 13: 1237.
84. Helfand, E. and Wasserman, Z.R. *Macromolecules*, **1976**; 9: 879.
85. Semenov, A.N. *Sov. Phys. JETP*, **1985**; 61: 733.
86. Semenov, A.N. *Macromolecules*, **1993**.
87. Ohta, T. and Kawasaki, K. *Macromolecules*, **1986**; 19: 2621.
88. Hasegawa, H., Tanaka, H., Hashimoto, T. and Han, C.C. *Macromolecules*, **1987**; 20: 2120.
89. Bartels, V.T., Stamm, M., Abetz, V. and Mortensen, K. *Europhys. Letters*, **1995**; 31: 81.

90. Sakamoto, N., Hashimoto, T., Han, C.D., Kim, D. and Vaidya, N.Y. *Macromolecules*, **1997**; 30: 5832.
91. Swab, M. and Stöhn, B. *Colloid Polym. Sci.*, **1997**; 275: 341.
92. Mortensen, K. *J. Phys. Cond. Matter.*, **1996**; 8: A103.
93. Dudowicz, J. and Freed, K. *Macromolecules*, **1995**; 28: 6625.
94. Schwahn, D., Frielinghaus, H., Mortensen, K. and Almdal, K. *Phys. Rev. Lett.*, **1996**; 77: 3153.
95. Hasegawa, H., Sakamoto, N., Takeno, H., Jinnai, H., Hashimoto, T., Schwahn, D., Frielinghaus, H., Janssen, S., Imai, M. and Mortensen, K. *J. Phys. Chem. Sol.*, **1999**: 60; 1307.
96. Hajduk, D.A., Urayama, P., Gruner, S.M. and Erramilli, S. *Macromolecules*, **1995**; 28: 7148.
97. Frielinghaus, H., Schwahn, D., Mortensen, K., Almdal, K. and Springer, T. *Macromolecules*, **1996**; 29: 3263.
98. Mortensen, K., Almdal, K., Schwahn, D. and Frielinghaus, H. *Macromol. Symp.*, **1997**; 121: 245.
99. Bartels, V.T., Stamm, M. and Mortensen, K. *Polymer Bulletin*, **1996**; 36: 103.
100. Tang, H. and Freed, K.F. *Macromolecules*, **1991**; 24: 958.
101. Freed, K.F. and Dudowicz, J. *J. Chem. Phys.*, **1992**; 97: 2105.
102. Dudowicz, J. and Freed, K.F. *Macromolecules*, **1993**; 26: 213.
103. Dudowicz, J. and Freed, K.F. *J. Chem. Phys.*, **1994**; 100: 4653.
104. Bidkar, U.R. and Sanchez, I.C. *Macromolecules*, **1995**; 28: 3963.
105. Keller, A., Pedemente, E. and Willmouth, E. *Nature*, **1970**; 225: 538.
106. Hadziiannou, G., Mathis, A. and Scoulios, A. *Colloid Polym. Sci.*, **1979**; 2570: 136.
107. Almdal, K., Mortensen, K., Ryan, A.J. and Bates, F.S. *Macromolecules*, **1996**; 29: 5940.
108. Schultz, M.F., Bates, F.S., Almdal, K. and Mortensen, K. *Phys. Rev. Lett.*, **1994**; 73: 86.
109. Hillmyer, M., Bates, F.S., Almdal, K. and Mortensen, K. *Science*, **1996**; 271: 976.
110. Vigild, M.E., Almdal, K. and Mortensen, K. *Macromolecules*, **1998**; 31: 5702.
111. Hamley, I., Koppi, K.A., Rosedale, J., Bates, F.S., Almdal, K. and Mortensen, K. *Macromolecules*, **1993**; 26: 5959.
112. Koppi, K.A., Tirrell, M., Bates, F.S., Almdal, K. and Colby, R.H. *J. Phys. II (France)*, **1992**; 2: 1941.
113. Winey, K.I., Patel, S.S., Larson, R.G. and Watanabe, H. *Macromolecules*, **1993**; 26: 4373.
114. Patel, S.S., Larson, R.G., Winey, K.I. and Watanabe, H. *Macromolecules*, **1995**; 28: 4313.
115. Zhang, Y.U., Wiesner, U. and Spiess. *Macromolecules*, **1995**; 28: 778.
116. Zhang, Y.U., Wiesner, U., Yang, Y., Pakula, T. and Spiess. *Macromolecules*, **1996**; 29: 5427.
117. Suehiro, S., Saijo, K., Seto, T., Sakamoto, N., Hashimoto, T., Ito, K. and Amemiya, Y. *J. Synch. Radiation*, **1996**; 3: 225.
118. Cates, M.E. and Milner, S.T. *Phys. Rev. Lett.*, **1989**; 62: 1856.
119. Marques, C.M. and Cates, M.E. *J. Phys. (France)*, **1990**; 51: 1733.
120. Fredrickson, G.H. *J. Rheology*, **1994**; 38: 1045.
121. Koppi, K.A., Tirrell, M. and Bates, F.S. *Phys. Rev. Lett.*, **1993**; 70: 1449.
122. Bates, F.S., Koppi, K.A., Tirrell, M., Almdal, K. and Mortensen, K. *Macromolecules*, **1994**; 27: 5934.
123. Almdal, K., Mortensen, K., Koppi, K.A., Tirrell, M. and Bates, F.S. *J. Phys. II (France)*, **1996**; 6: 617.
124. Nakatani, A.I., Morrison, F.A., Douglas, J.F., Mays, J.W., Jackson, C.L., Muthukumar, M. and Han, C.C. *J. Chem. Phys.*, **1996**; 104: 1589.
125. Winter, H.H., Scott, D.B., Gronski, W., Okamoto, S. and Hashimoto, T. *Macromolecules*, **1993**; 26: 7236.
126. Tepe, T., Hajduk, D.A., Hillmyer, M.A., Weimann, P.A., Tirrell, M., Bates, F.S., Almdal, K. and Mortensen, K. *J. Rheology*, **1997**; 41: 1147.
127. Hajduk, D.A., Tepe, T., Takenouchi, H., Tirell, M., Bates, F.S., Almdal, K. and Mortensen, K. *J. Chem. Phys.*, **1998**; 108: 326.
128. Semenov, A.N. *Macromolecules*, **1989**; 22: 2849.
129. Vavasour, J.D. and Whitmore, M.D. *Macromolecules*, **1992**; 25: 5477.
130. Helfand, E. and Wasserman, Z.R. In Goodman, I. (Ed.): *Developments in Block Copolymers-1*, Applied Science Publishers, **1982**.
131. Hamley, I.W. and Bates, F.S. *J. Chem. Phys.*, **1992**; 100: 6813.
132. Marques, C.M. and Cates, M.E. *Europhys. Lett.*, **1990**; 13: 267.
133. Almdal, K., Koppi, K.A., Bates, F.S. and Mortensen, K. *Macromolecules*, **1992**; 25: 1743.
134. Khandpur, A.K., Förster, S., Bates, F.S., Hamley, I.W., Ryan, A.J., Bras, W., Almdal, K. and Mortensen, K. *Macromolecules*, **1995**; 28: 8796.
135. Hajduk, D.A., Takenouchi, H., Hillmyer, M.A., Bates, F.S., Vigild, M.E. and Almdal, K. *Macromolecules*, **1997**; 30: 3788.
136. Pedersen, J.S. *Adv. Colloid Interface Science*, **1994**; 70: 171.
137. Mortensen, K. Small-Angle scattering studies of block copolymer micelles, micellar mesophases and networks in *Amphiphilic Block copolymers: Self assembly and applications*, (Ed.) Alexandridis and Lindman) Elsevier Science, New York and London, **2000**.
138. Svensson, B., Alexandridis, P., Olsson, U. and Mortensen, K. *submitted*, **1999**.
139. Pedersen, J.S. and Gerstenberg, M. *Macromolecules*, **1996**; 29: 1363.
140. Mortensen. K. and Talmon, Y. *Macromolecules*, **1995**; 28: 8829.
141. Percus, J.K. and Yevick, G.J. *Phys. Rev.*, **1958**; 110: 1.
142. Ashcroft, N.W. and Lekner, J. *Phys. Rev.*, **1966**; 145: 83.
143. Kinning, D.J. and Thomas, E.L. *Macromolecules*, **1984**; 17: 1712.
144. Mortensen, K. and Pedersen, J.S. *Macromolecules*, **1993**; 26: 805.
145. Hansen, J.P. and McDonald. *Theory of simple liquids*, Academic Press, New York, **1987**.
146. Hayter, J.P., Penfold, J. *Mol. Phys.*, **1981**; 42: 109; and *J. Chem. Soc. Faraday. Trans.*, **1081**; 46: 651.
147. Mortensen, K. *Europhys. Lett.*, **1992**; 19: 599.
148. Mortensen, K., Brown, W. and Nordén, B. *Phys. Rev. Lett.*, **1992**; 68: 2340.
149. Mortensen, K., Schwahn, D., Janssen, S. *Phys. Rev. Lett.*, **1993**; 71: 1728.
150. Mortensen, K. and Brown, W. *Macromolecules*, **1993**; 26: 4128.
151. Robbins, M.O., Kremer, K. and Grest, G.S. *J. Chem. Phys.*, **1988**; 88: 3286.
152. Mittelbach, P. and Porod, G. *Acta Physica Austr.*, **1961**; 14: 405.
153. Cusack, S. *J. Mol. Biol.*, **1981**; 145: 541.
154. Pedersen, J.S. and Schurtenberger, P. *J. Appl. Cryst.*, **1996**; 29: 646.

155. Hecht, E., Mortensen, K. and Hoffmann, H. *Macromolecules*, **1995**; 28: 5465.
156. Caillé, C. *R. Acad. Sci. Ser. B*, **1972**; 274: 891.
157. Hoseman, R. and Bagchi, S.N. *Direct analysis of difraction by matter*, North-Holland Publ., Amsterdam, **1962**.
158. Lemmich, J., Mortensen, K., Ipsen, J.H., Hønger, T., Bauer, R. and Mouritsen, O.G. *Phys. Rev. B*, **1996**; 53: 5169.
159. Laurser, J.H., Func, J.C., Sedat, J.W., Agard, D.A., Smith, S.D., Samseth, J., Mortensen, K. and Spontak, R. *Langmuir*, **1997**; 13: 2177.
160. Bates, F.S., Maurer, W.W., Lipic, P.M., Hillmyer, M.A., Almdal, K., Mortensen, K., Fredrickson, G.H. and Lodge, T.P. *Phys. Rev. Lett.*, **1997**; 79: 849.
161. Auvray, L., Cotton, J.P., Ober, R. and Taupin, C. *J. Phys. Chem.*, **1984**; 88: 4586.
162. Debye, P. and Bueche, A.M.J. *Appl. Phys.*, **1949**; 20: 518.
163. Teubner, M. and Strey, R. *J. Chem. Phys.*, **1987**; 87: 3195.
164. Berk, N.F. *Phys. Rev. Lett.*, **1987**; 58: 2718.
165. Chen, S.-H., Chang, S.L. and Strey, R. *Prog. Colloid Polym. Sci.*, **1990**; 81: 30.
166. Chen, S.-H., Chang, S.L., Strey, R., Samseth, J. and Mortensen, K. *J. Phys. Chem.*, **1991**; 95: 7427.
167. Mortensen, K., Almdal, K., Kleppinger, R., Mischenko, N. and Reynaers, H. *Physica B — Condensed Matter*, **1998**; 241: 1025.
168. Reynders, K., Mischenko, N., Mortensen, K., Overbergh, N. and Reynaers, H. *Macromolecules*, **1995**; 28: 8699.
169. Mortensen, K. *Current Opinion Coll. Interface Sci.*, **1998**; 3: 12.